TECHNISCHE UNIVERSITÄT DRESDEN

Fakultät Forst-, Geo- und Hydrowissenschaften

On the reconstruction of three-dimensional cloud fields by synergistic use of different remote sensing data

Dissertation zur Erlangung des akademischen Grades
Doctor rerum naturalium (Dr. rer. nat.)

vorgelegt von
Dipl.-Geogr. Klemens Barfus

Gutachter:

Herr Prof. Dr. Christian Bernhofer
TU Dresden / Institut für Hydrologie und Meteorologie

Herr Prof. Dr. Andreas Macke
Universität Leipzig / Institut für Meteorologie

Dresden, 01.06.2010

Erklärung des Promovenden

Die Übereinstimmung dieses Exemplars mit dem Original der Dissertation zum Thema

„On the reconstruction of three-dimensional cloud fields by synergistic use of different remote sensing data“

wird hiermit bestätigt.

.....
Ort, Datum

.....
Unterschrift

Abstract

The objective of this study was to assess if new cloud datasets, namely horizontal fields of integrated cloud parameters and transects of cloud profiles becoming available from current and future satellites like MODIS and CloudSAT as well as EarthCARE will allow for the reconstruction of three-dimensional cloud fields.

Because three-dimensional measured cloud fields do not exist, surrogate cloud fields were used to develop and test reconstruction techniques. In order to answer the question if surrogate cloud fields may represent real cloud fields and to evaluate potential constraints for cloud field reconstruction, statistics of surrogate cloud fields have been compared to statistics of various remote sensing retrievals. It has turned out that except for cloud droplet effective radius, which is too low, other cloud parameters are in line with parameters derived from measurements.

The reconstruction approach is divided into two parts. The first one deals with the reconstruction of the cloud fields. Three techniques with varying complexity are presented constraining the reconstruction by measurements to various degrees. Whereas the first one applies only information of a satellite radiometer, the other two constrain the retrieval also by profile information measured within the domain. Comparing the reconstruction quality of the approaches, there is no superior algorithm performing better for all cloud fields. This might be ascribed to liquid water content profiles of the surrogate cloud fields close to their adiabatic reference. Consequently, the assumption of adiabatic liquid water content profiles of the first scheme yields adequate estimates and additional information from profiles does not improve the reconstruction.

The second part of the reconstruction approach addresses the reconstruction quality by comparing parameters of radiative transfer describing photon path statistics as well as radiances. Therefore, three-dimensional radiative transfer simulations with a Monte Carlo code were carried out for the surrogate cloud fields as well as for the reconstructed cloud fields. It was assumed that deviations of the parameter simulated for the reconstructed cloud and the surrogate cloud field are smaller when reconstruction is more accurate. For parameter describing photon pathes it has been found that only deviations of geometrical pathlength statistics reflect the reconstruction quality to a certain degree. Deviations of other parameters like photon penetration depth do not allow for either assessing local differences in reconstruction quality by an individual reconstruction scheme or to infer the most appropriate reconstruction scheme.

The differences in reflectances do also not enable to evaluate reconstruction quality. They prevent from gaining insight in local accuracy of reconstruction due to effects like horizontal photon transport weakening the relations between microphysical as well as optical properties and radiances. In order to address these effects, grids of various complexity, derived by applying photon path properties, were used to weight deviations of cloud properties when analyzing the relationships. Unfortunately, there is no increase of explained variance due to the application of the weighting grids.

Additionally, the sensitivity of the results to the model set-up, namely the spatial resolution of the cloud fields as well as the simplification and neglection of ancillary parameters, were analyzed. Though one would assume a strengthening of relationships between deviations of cloud parameters and deviations of radiances due to more reliable sampling and reduced inter-column transport of photons when column size increases, there is no indication for resolutions where an assessment of the reconstruction quality by means of reflectance deviations becomes feasible. It also has been shown that inappropriate treatment of aerosols in the radiative transfer simulation impose an error comparable in magnitude to differences in reflectances due to inaccurate cloud field reconstruction. This is especially the case when clouds are located in the boundary layer of the aerosol model.

Consequently, appropriate aerosol models should be applied in the analysis. May be due to the low surface reflection and the high cloud optical depths, the representation of the surface reflection function seems to be of minor importance.

Summarizing the results, differences in radiative transfer do not allow for the assessment of cloud field reconstruction quality. In order to accomplish the task of cloud field reconstruction, the reconstruction part could be constrained employing information from additional measurements. Observational geometries enabling to use tomographic methods and the application of additional wavelengths for validation might help, too.

Zusammenfassung

Ziel der Arbeit war die Evaluierung inwieweit Datensätze von Wolkenparametern, horizontale Felder integraler Wolkenparameter und Schnitte vertikal aufgelöster Parameter, zur Rekonstruktion dreidimensionaler Wolkenfelder genutzt werden können. Entsprechende Datensätze sind durch MODIS und CloudSAT erstmals vorhanden und werden zusätzlich mit dem Start von EarthCARE zur Verfügung stehen.

Da dreidimensionale Wolkenfelder aus Messungen nicht existieren, wurden zur Entwicklung der Rekonstruktionsmethoden surrogate Wolkenfelder genutzt. Um die Qualität der surrogaten Wolkenfelder abzuschätzen und um mögliche Randbedingungen zur Rekonstruktion aufzuzeigen, wurden Statistiken der surrogaten Wolkenfelder mit denen unterschiedlicher Fernerkundungsprodukte verglichen. Dabei zeigte sich, dass, abgesehen von den gegenüber Messungen zu geringen Effektivradien der Wolkentropfen in den surrogaten Wolkenfeldern, die übrigen Wolkenparameter gut übereinstimmen.

Der Rekonstruktionsansatz gliedert sich in zwei Teile. Der erste Teil beinhaltet die Rekonstruktion der Wolkenfelder. Dazu werden drei Techniken unterschiedlicher Komplexität genutzt, wobei die Komplexität durch den Grad der eingebundenen Messungen bestimmt wird. Während die einfachste Technik lediglich Informationen, wie sie aus Messungen mit einem Satellitenradiometer gewonnen werden können, nutzt, binden die anderen Techniken zusätzlich Profilinformationen aus dem beobachteten Gebiet ein. Analysen zeigten, dass keine der Methoden für alle untersuchten Wolkenfelder den anderen Methoden überlegen ist. Dies mag daran liegen, dass die Flüssigwasserprofile der surrogaten Wolkenfelder nur geringfügig von den in der ersten Rekonstruktionsmethode angenommenen adiabatischen Flüssigwasserprofilen abweichen, so dass die Nutzung der Profile kaum zusätzliche Information für die Rekonstruktion liefert.

Im zweiten Teil des Rekonstruktionsansatzes wird die Qualität der rekonstruierten Wolkenfelder durch den Vergleich von Parametern des Strahlungstransfers, wie Photonenpfad-Statistiken und Strahlungsgrößen, evaluiert. Dazu wurden sowohl für die surrogaten Wolkenfelder als auch für die rekonstruierten Wolkenfelder dreidimensionale Strahlungstransfersimulationen mit einem Monte-Carlo-Modell durchgeführt. Angenommen wurde hierbei, dass eine bessere Rekonstruktionsqualität durch geringere Abweichungen der betrachteten Strahlungsparameter aus Simulationen mit rekonstruierten und surrogaten Wolkenfeldern gekennzeichnet ist. Bei den Parametern, die die Photonenwege beschreiben, unterstützen lediglich die Abweichungen der geometrischen Photonenweglängen diese These. Weder erlauben die Abweichungen der übrigen Parameter, zum Beispiel der Eindringtiefen, Rückschlüsse auf die lokale Rekonstruktionsqualität der einzelnen Methoden zu ziehen, noch ermöglichen sie die beste Rekonstruktionsmethode zu identifizieren.

Auch die Unterschiede der simulierten Reflektanzen können nicht zur Bestimmung der Rekonstruktionsqualität herangezogen werden. Durch Effekte wie horizontale Photonentransporte werden die Zusammenhänge zwischen mikrophysikalischen und optischen Eigenschaften und Reflektanzen der jeweiligen Gittersäule aufgeweicht, und folglich sind keine Rückschlüsse auf die lokale Rekonstruktionsqualität möglich. Um auf entsprechende Effekte einzugehen, wurden für die Analyse Wichtungsfelder unterschiedlicher Komplexität aus Photonenwegeigenschaften generiert, um diese zur Wichtung der Abweichungen der Wolkeneigenschaften zu nutzen. Der Anteil der erklärten Varianz konnte jedoch durch die Nutzung der entsprechenden Wichtungsfelder nicht erhöht werden.

Zusätzlich wurden Sensitivitätsstudien hinsichtlich einzelner Vorgaben der Untersuchung durchgeführt. Dazu wurden sowohl der Einfluss der räumlichen Auflösung der Wolkenfelder als auch die Vereinfachung oder Nichtbetrachtung einzelner Modellparameter analysiert. Eine Reduzierung der Auflösung einhergehend mit einem zuverlässigeren Sampling und reduzierten Photonentransport

zwischen den Gittersäulen führte zu keinem direkteren Zusammenhang zwischen den Abweichungen der Reflektanzen und den Abweichungen der mikrophysikalischen Eigenschaften. Folglich existiert keine Auflösung, die die Anwendung des Verfahrens ermöglichen würde. Ebenso wurde gezeigt, dass die unzureichende Einbeziehung von Aerosolen bei den Strahlungstransfersimulationen einen Fehler verursachen kann, der in der Größe dem Unterschied der Reflektanzen unzureichender Wolkenfeldrekonstruktionen gleichkommt. Dies ist insbesondere der Fall, wenn die Wolken sich innerhalb der Grenzschicht des Aerosolmodells befinden. Entspechend sollte in solchen Situationen dem verwendeten Aerosolmodell besondere Beachtung geschenkt werden. Hingegen ist der Einfluss des Ansatzes, wie die Bodenreflektion beschrieben wird, eher gering. Dies mag an dem verwendeten Modell mit einer geringen Albedo in Kombination mit optisch dicken Wolken liegen.

Zusammenfassend kann festgestellt werden, dass die Unterschiede im Strahlungstransfer nicht zur Abschätzung der Rekonstruktionsqualität der Wolkenfelder herangezogen werden können. Um dem Ziel einer dreidimensionalen Wolkenfeldrekonstruktion näher zu kommen, könnten beim Rekonstruktionsteil Informationen aus zusätzlichen Messungen als Vorgaben genutzt werden. Ebenso könnten Beobachtungsgeometrien, welche die Anwendung tomographischer Methoden erlauben, sowie zusätzliche Wellenlängen zur Validierung der Rekonstruktionsergebnisse verwendet werden.

Contents

1 Introduction **1**

2 Theory **8**
2.1 Liquid water clouds . . . 8
2.2 Macrophysical parameters . . . 9
2.2.1 Cloud fraction . . . 9
2.2.2 Cloud-base and Cloud-top . . . 10
2.3 Microphysical parameter . . . 11
2.3.1 Liquid water content . . . 11
2.3.2 Drop size distributions and effective radius . . . 14
2.4 Radiative properties and radiative transfer . . . 18
2.4.1 Radiative properties of clouds . . . 18
2.4.2 Radiative characteristics of cloud droplet ensembles . . . 18
2.4.3 Aerosol particles and their radiative properties . . . 20
2.4.4 Rayleigh optical properties . . . 22
2.4.5 Surface reflection . . . 23
2.4.6 Solar radiation . . . 23
2.4.7 Radiative transfer modeling . . . 25
2.4.8 Modifications of the Monte Carlo model . . . 27

3 Data **29**
3.1 4D Clouds and the BBC-campaign . . . 29
3.2 Simulated cloud fields . . . 29
3.3 Description of surrogate cloud fields . . . 32

4 Reconstruction of cloud fields **45**
4.1 Introduction . . . 45
4.2 Reconstruction without information of profiling instruments . . . 45
4.3 Reconstruction with information of the mean profile . . . 46
4.4 Reconstruction with profile information of the complete transect . . . 51
4.5 Quality of the reconstructed cloud fields . . . 51

5 Differences between the radiative transfer in original and reconstructed cloud fields **56**
5.1 Differences in photon statistics of the reconstructed cloud fields . . . 57
5.2 Differences between radiation results of original and reconstructed cloud fields . . . 66

6 Influence of ancillary parameters **80**

6.1 Influence of horizontal resolution 80
6.2 Influence of aerosol profile assumptions 83
6.3 Lower boundary conditions 87

7 Conclusions and perspective **91**

... Mir scheint, gerade das macht die Wolken schön und bedeutsam, daß sie sich bewegen, und daß sie im Himmel, der für unsere Augen toter Raum ist, Entfernungen, Maße und Zwischenräume schaffen. Daß diese Entfernungen und Maße unerhört täuschen, ist ganz belanglos ...

Wie die Wolken uns den Luftraum sichtbarer machen, so machen sie uns die Bewegungen der Luft wahrnehmbarer. Und die Bewegungen der Luft sind zwar nicht unserem Denken, wohl aber unseren Sinnen stets rätselhaft und darum fesselnd. Wenn hundert Meter oder tausend Meter über meinem Kopf die Luft bewegt ist, Strömungen gehen, sich treffen, kreuzen, teilen, bekämpfen, so habe ich nichts davon. Sehe ich aber eine Wolke oder eine Wolkenschar wandern, rascher und langsamer reisen, innehalten, sich teilen, ballen, umformen, schmelzen, bäumen, zerreißen, so ist das ein Schauspiel und nimmt Interesse und Teilnahme in Anspruch.

So ist es auch mit dem Licht, daß wir im scheinbar leeren, blauen Raum nicht wahrnehmen. Schwimmt aber eine Wolke darin, wird sie grau, hellgrau, weiß, golden, rosig, so ist all das Licht in der Höhe mir nicht mehr verloren; ich sehe, beobachte, genieße es. Wer hat nicht schon am Abend, wenn die Sonne längst versunken und die Erde erloschen war, hoch oben noch Wolken brennen und im Lichte schwimmen sehen ...

from Hermann Hesse, Wolken (1907)

Chapter 1

Introduction

Clouds play the key role in human perception of the current atmospheric state. Besides the assessment for the chance of precipitation by the brightness of the clouds, the observer can also recognize the high variability of clouds on very small temporal and spatial scales as a result of cloud micro- and macrophysics representing turbulence on a wide range of scales in the atmosphere. Especially the spatial variability of cloud properties is the reason, why clouds are responsible for uncertainties in climate modeling. The recent report of the International Panel on Climate Change (IPCC) emphasizes the progress in cloud treatment in climate models but also indicates cloud feedbacks as responsible for the largest uncertainties in climate sensitivity estimates (Solomon et al., 2007). For example some modeling studies found an increase of boundary layer cloud cover with increasing surface temperature whereas observations reported decreasing cloud optical depth with rising temperature leading to the opposite effect of cloud radiative forcing (Randall et al., 2007).

Current global climate models like ECHAM 5 are operated with resolutions of up to 0.75° x 0.75° (Roeckner et al., 2004) and therefore are not able to resolve individual clouds or even variability within these clouds. These variabilities are also not resolved by regional climate models like REMO (Regional Model) with resolutions of up to 0.1° or numerical weather prediction models like the LM (Lokalmodell) of the German Weather Service with an operational resolution of 7 km. However, these variabilities have been identified as important for the radiative transfer within the grid cell.

Various investigations have been done to quantify the effects of subgrid cloud variabilities like liquid water path (Cahalan et al., 1994b), cloud-top height (Loeb et al., 1998; Richter et al., 2007) or the organization of boundary layer clouds (Li et al., 1994) on gridscale radiative transfer. Several effects have been detected which arise when subgrid variability is neglected or treated in a simplified way. Cahalan et al. (1994a) found the "plan parallel bias", which arises when the albedo is calculated for the mean properties of the gridcell instead of calculating it for every subgrid column and then averaging the individual albedos, to be about 15 %. This decrease of albedo for calculation of the so called independent pixel approximation (IPA) originates from the nonlinear relationship between optical depth and albedo but still neglects modifications of the radiation field by horizontal transport of photons between columns. This effect called "IPA albedo bias" is rather small with about 1 % in overcast cloud scenes (Cahalan et al., 1994b) but increases up to 15 % for broken cloud scenes (Di Guiseppe and Tompkins, 2003).

In addition to the radiative effects cloud heterogeneity in the subgrid scale is relevant for precipitation in atmospheric models due to auto-conversion. This process, where larger cloud droplets collect smaller ones and form rain droplets, starts when drop size exceeds a certain threshold. The

drop sizes are a function of liquid water path. Accordingly, there are situations where no precipitation will form when the drop size is derived from gridscale liquid water path, but when subgrid variability of liquid water path and drop size is taken into account there might be some areas with precipitation (Pincus and Klein, 2000).

There are different ways to handle the representation of clouds in atmospheric models. They can be distinguished in attempts to describe subgrid cloud features in a more statistic way (Tompkins, 2002) by determining probability distribution functions (PDF) of subgrid properties from gridscale variables and attempts to model clouds in 'realtime' within climate simulations. One of these attempts is the so called 'Superparametrization' stated by Randall et al. (2003), where Cloud Resolving Models (CRM) are embedded in climate models, which is so far limited by the current computer power. Though in this attempt clouds are simulated by the model-generated thermodynamics of the atmosphere, like in the statistical attempts, observed cloud data are needed for comparison and validation.

Because there is no method to measure three-dimensional cloud fields (Evans and Wiscombe, 2004) they have to be simulated depending more or less on the range of input data. The adequate strategy depends on the application of these cloud fields and can loosely be divided in stochastic models, dynamic models, and reconstruction schemes.

Stochastic models are widely used for radiative transfer studies to account for the influence of subgrid cloud variabilities and the consequences for remote sensing algorithms. These models range from bounding cascade models (Cahalan et al., 1994b) to reproduce a predefined power spectrum for the description of spatial variability, over Fourier methods (Barker and Davies, 1992) to more advanced methods like surrogate clouds (Venema et al., 2005) and similar methods (Evans and Wiscombe, 2004) incorporating multiple input data. All these models have in common that they simulate cloud fields with statistical properties like the Fourier spectrum or the probability distribution function predefined by the input data. Their spatial resolution is just limited by the scales where the measured statistical properties like the slope of the Fourier spectrum become invalid. However, none of these models is able to reproduce horizontal anisotropy of the original cloud field so far. Dynamic models like Cloud Resolving Models (CRM) or Large-Eddy Simulations (LES) simulate cloud fields for predefined conditions like soil moisture, atmospheric stability and moisture distribution. The generated cloud fields are used for studies of geometrical (Neggers et al., 2003) and microphysical properties (Hinkelman et al., 2005) as well as for radiation aspects (Coley and Jonas, 1997). The last category, denoted as reconstruction schemes, combines several retrievals of remote sensing instruments not only to simulate cloud fields with predefined statistics but moreover to reconstruct the observed cloud fields. In the geostatistical sense reconstruction methods are more exact than stochastic models because of preserving the values at the sampling points.

A simple approach merely using data of a spaceborne plattform is described in Hutchison (2002). Based on MODIS data geometrical cloud thickness is estimated from the optical thickness assuming a vertical homogeneous effective radius deduced from MODIS data, too, and a height independent liquid water content depending on cloud type adopted from data out of literature (Liou, 1992). Because of these limitations Hutchison restrains the algorithm to stratiform clouds though these clouds also show stratifications in microphysical properties (Nicholls and Leighton, 1986). Due to the cloud-base algorithm using data of a microwave radiometer (Wilheit and Hutchison, 2000), this approach is limited to single-layer clouds and the application over oceans.

The aim of the present study is to evaluate the possibilities to reconstruct three-dimensional cloud fields by merging data from miscellaneous instruments as they will become available from

satellite missions with onboard active sounding instruments (Stephens et al., 2002). Investigations are limited to water clouds. The datasets and their geometry are illustrated in Fig. 1.1. They consist of two-dimensional fields of cloud optical depth, effective radius near cloud-top and cloud-top height. Within the volume defined by the horizontal fields, a slice with observed profiles of liquid water content and effective radius is available. For these profiles also cloud-base height is known. As mentioned before current systems are not capable to observe three-dimensional cloud fields. Accordingly simulated cloud fields are employed instead of real cloud fields and datasets as they will become available from satellite are extracted. Radiative transfer is simulated for the reference fields as well as for fields reconstructed by methods developed in the present study. The main idea is that measured radiances from satellite or in this case simulated for the reference field will coincide with simulated radiances for the reconstructed cloud field, in areas where cloud field reconstruction succeeds.

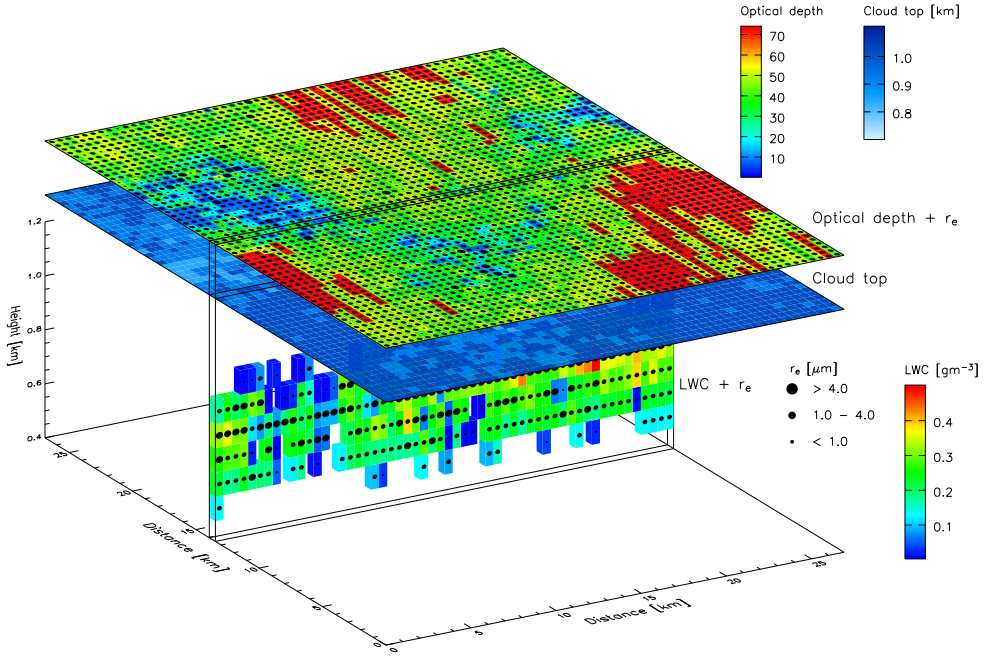

Figure 1.1: Data pool for the cloud field reconstruction consisting of 2D radiometer retrievals namely optical depth, effective radius and cloud-top height as well as profiler retrievals like liquid water content, effective radius and cloud-base height

There are two approaches presented in literature dealing with quite similar problems of merging data from multiple sources in order to reconstruct cloud fields as the present study and therefore are described here in more detail. The first one (Liou et al., 2002) is dedicated to cirrus clouds and the second one (Marchand and Ackerman, 2004) aims to reconstruct stratiform water clouds.

The approach of Liou et al. (2002) uses input data characterized by the same geometry as data in Fig. 1.1. As in this study, Liou et al. (2002) merge horizontal fields of vertical integrated cloud data from NOAA AVHRR and MODIS like optical depth and mean effective ice crystal size with profile data recorded within the satellite-observed volume. The profiles consist of ice water content and ice crystal size parameters measured by a 35 GHz Doppler radar. Time series of profiles are transferred into space domain by assuming cloud fields advected due to local wind speed and direction. This approach is feasible as long as the frozen turbulence assumption (Barker et al.,

2004) is valid, which states that within the time needed to advect the cloud field over the observed domain no evolutionary changes in cloud structure take place. In this analysis the mean wind speed in the cloud layer is employed to the overall profile avoiding complicated situations where speed and direction of advection differ between cloud levels. The result of the time-space conversion is a slice of profiles within the satellite observed domain. Because investigations have shown that cloud-base variations for cirrus clouds are higher in along-wind direction than in crosswise direction, the respective cloudbase of the slice is assigned to the pixel crosswise from the slice, too. When in a first guess ice crystal size is assumed to be homogeneous in the cloud column, optical depth, cloud geometrical thickness, and ice crystal size can be used for the determination of the ice water path and the average ice water content following a parametrization of light scattering by ice crystals (Liou, 1992). Vertical distribution of the ice water path and ice crystal size is done by height dependent scaling coefficients that have been calculated for the columns of the slice describing the ratio of profile values of ice water content/ice crystal size and the average values of ice water content/ice crystal size. The coefficients are used to scale the ice water content and the ice crystal size in the columns crosswise from the profile. Due to the pixel size of MODIS and NOAA AVHRR the horizontal resolution of the reconstructed cloud fields is about 1 km, whereas the properties of the radar profile result in a vertical resolution of about 90 m

Several assumptions are made in the study described above confining the applicability to water clouds. One of these assumptions is the higher variability of cirrus clouds in the along-wind direction. This feature becomes most evident for cirrus clouds induced by gravity waves. Hinkelman et al. (2005) investigated the influence of wind and windshear on the anisotropy of cumulus clouds in Large-Eddy simulations but did not find the maximum anisotropy neither in along-wind nor in cross-wind direction. So there is no evidence for the validity of this assumption for convective or stratiform water clouds particularly if they are not wave induced.

There is also a parametrization for water clouds where the optical depth can be calculated from geometrical thickness, liquid water content and droplet size effective radius (Nevzorov and Shugaev, 1972), but when values in the liquid water profile or the profile of the effective radius are altered due to height dependent scaling coefficients, the overall optical depth of the column will change according to the nonlinear nature of the relation between microphysical and optical properties.

Marchand and Ackerman (2004) used AirMISR, an aircraft mounted version of the Multiangle Imaging Spectroradiometer (MISR), profiles of cloud droplet size and ground based lidar data to reconstruct three-dimensional cloud fields. Cloud-top height is retrieved by matching of two images applying stereographic methods. Cloud-base is derived from lidar data and assigned to the entire cloud field, so that cloud-base is homogeneous. The profile of particle sizes collected by transects in different altitudes in the clouds was also assigned to the overall cloud field. Liquid water path was retrieved by 1D radiative transfer applying nadir data of a visible channel. This first-guess cloud field was used to perform complete 3D radiative transfer simulations. When measured and simulated radiation differed, LWP was adjusted by an iterative procedure, which was stopped when differences fall below a predefined threshold. This approach is appealing because of its efforts to include 3D effects in the LWP retrieval. Due to the horizontal resolution of the cloud field of 27.5 m horizontal photon transport should play a considerable role and consequently radiation is not only determined by the microphysical and optical properties of the column itself, but also by the properties of adjacent columns. Marchand and Ackerman (2004) unfortunately provide no information how they tackle this problem when adjusting the LWP in the iterative procedure.

As mentioned before the objective of this work is to evaluate the feasibility to reconstruct three-dimensional cloud fields by merging remotely sensed cloud data from various instruments. All data are or will become available from instruments mounted on spaceborne platforms (Stephens et al., 2002) so that a more global coverage of cloud observations will be obtained. Following from the more or less turbulent environment of cloud formation, cloud properties vary over a wide range of scales which are to some extent below the resolution of the sensors. These subgrid properties induce lots of degrees of freedom which might be reduced if more knowledge of cloud dynamics and the resulting statistic and cloud structure will become available from models and observations (Iwabuchi and Hayasaka, 2002). So far the degrees of freedom for this study have to be reduced by several assumptions.

The first restriction is that this study deals with non-precipitating water clouds, so there is no need to deal with optical properties of ice and mixed phase clouds. Furthermore, clouds in this study have in common that they are single-layer clouds though there are some methods to identify multilayered clouds from airborne active (Platt et al., 1994) and passive instruments (Baum et al., 1995), too. Chambers et al. (1997) used a histogram technique where unimodal histograms of two Landsat channels indicate single-layer clouds. Chang and Li (2005) analyzed global MODIS data of four months for the occurrence of low level single-layer clouds. Their low level clouds have cloud-top pressure values above 600 hPa and are not analyzed for multilayered clouds. Clouds of this category amount to 44.4 % of all clouds over the ocean and 35.6 % over land.

The cloud features of this study like cloud fraction and variability of microphysical properties are completely described by the resolution of the grid. As mentioned before there are many measurement campaigns dealing with variabilities of cloud features in the subgrid scale of atmospheric models quantifying their influence especially on gridscale radiative transfer. From this point of view the neglect of subgrid scale variability when using cloud fields with a horizontal resolution of about 400 m might be a crude approximation but is a consequence of the resolution of the cloud fields available for this study. In this context it also has to be noted that retrieval algorithms for cloud properties from satellite data assume plane-parallel clouds within the gridcell and consequently use one-dimensional radiative transfer models. Hence effects due to the influence of adjacent cells and the subgrid variability are neglected. The influences of adjacent cells have been investigated by various studies (e.g. Várnai, 2000), and some methods for bias corrections have been proposed. Chambers et al. (1997), for example, calculated gridscale effects for a large number of cloud situations and suggested a correction of these effects depending on several geometrical properties of the cloud field. In their study cloud fields exhibited cloud-base variability but cloud-top was held constant. Várnai and Davies (1999) found opposite effects of cloud-top variability and horizontal inhomogeneity of optical properties for distinct constellations. It has to be noted that Chambers et al. (1997) like many other authors used fixed values for the effective radius in their study, whereas Marshak et al. (2006) demonstrated the influence of effective radius variability on 3D radiative transfer and cloud property retrievals. Iwabuchi and Hayasaka (2002) identified mean values, variability, and its spatial organization of cloud geometrical and optical properties as input parameters for a bias correction. Also solar zenith angle, observation angle, and spatial resolution should be implemented in the correction method. Iwabuchi and Hayasaka (2002) recommend to observe small-scale geometrical and optical cloud properties and tried to find connections among them to use these relations for the description of subgrid properties in the correction method. From the aspects mentioned above it becomes clear, that there will be a discrepancy when cloud properties obtained by one-dimensional algorithms are employed to simulate the three-dimensional radiation field. This problem also underlies the study of Chambers et al. (1997). In the present study all

radiative transfer simulations are performed by three-dimensional methods. If methods developed here with the aid of simulated data would be applied to remotely sensed data, this problem would arise, too.

Another simplification is the coincidence of cloud properties deduced from different instruments. Different measurement principles and geometries of the instruments as well as varying retrieval methods will provide variable estimates of the observed quantity. In continuative studies there might be a chance to benefit from these differences when trying to gain more information from the data, but so far this problem is masked out.

Conditioned by the stochastic algorithm generating the three-dimensional cloud fields serving as input data cloud field statistics are isotropic. As mentioned above Hinkelman et al. (2005) found significant anisotropies in wind sheared cumulus cloud fields for wind speeds higher than 10 ms^{-1} but also noticed that the detection of the three-dimensional features responsible for the anisotropy might be difficult from two-dimensional data sets of vertically integrated cloud properties.

Most investigators apply one analytical form of the drop size distribution to the entire domain. This might be a simplification, too, especially for areas diluted by entrainment of clear air but reduces the degree of freedom for the present study.

An additional deviation from real-world conditions mentioned here is the assumption of homogeneous lower boundary conditions in radiative transfer simulations meaning that there is no spatially varying surface reflection function.

The integration of the cloud field reconstruction in the overall framework of this study is presented in Fig. 1.2 also providing an overview of the individual issues of this study. The starting point is the original three-dimensional cloud field. From this cloud field the satellite derived data set shown in Fig. 1.1 is compiled. Several schemes are applied to reconstruct three-dimensional cloud fields. For the original and the reconstructed cloud fields radiative transfer simulations with several simplifications compared to the real-world situations are carried out. The analyses of differences in microphysical and optical properties as well as differences in radiation will shed light on the question if differences in radiation reproduce differences in microphysics caused by inaccurate reconstruction and consequently the reconstruction quality can be assessed.

The outline of this study is as follows: In chapter 2 some macro- and microphysical properties of liquid water clouds are described, and the underlying processes are broadly sketched. This chapter also provides some references on measurements and remote sensing of these quantities and their limitations. The theory for the radiative properties of liquid water clouds, aerosols, and Rayleigh scatterers is described and the Monte Carlo radiative transfer model applied in this study and its modifications are delineated. Chapter 3 deals with the cloud fields used as the test cases for this study. There is a brief description of the simulation method to generate these fields. The subset of cloud fields selected for this study is characterized by several statistical parameters. Additionally the cloud fields are compared with cloud fields from literature to get an idea of the simulation quality. The following chapter presents three approaches to reconstruct three-dimensional cloud fields from the predefined data base. It includes the analysis and comparison of the reconstruction quality for the individual approaches. Chapter 5 describes the differences between results of radiative transfer simulations performed for the original and the reconstructed cloud fields. In the first part some geometrical aspects like photon-pathlength statistics and penetration depth of the photons into the cloud are explored, whereas the second part tries to link the deviations of the simulated radiation to differences in microphysical and optical properties of the cloud fields. The impact of some simplifications within the radiative transfer simulations like neglecting aerosol profiles and more complex surface reflection and the influence of the horizontal resolution of the

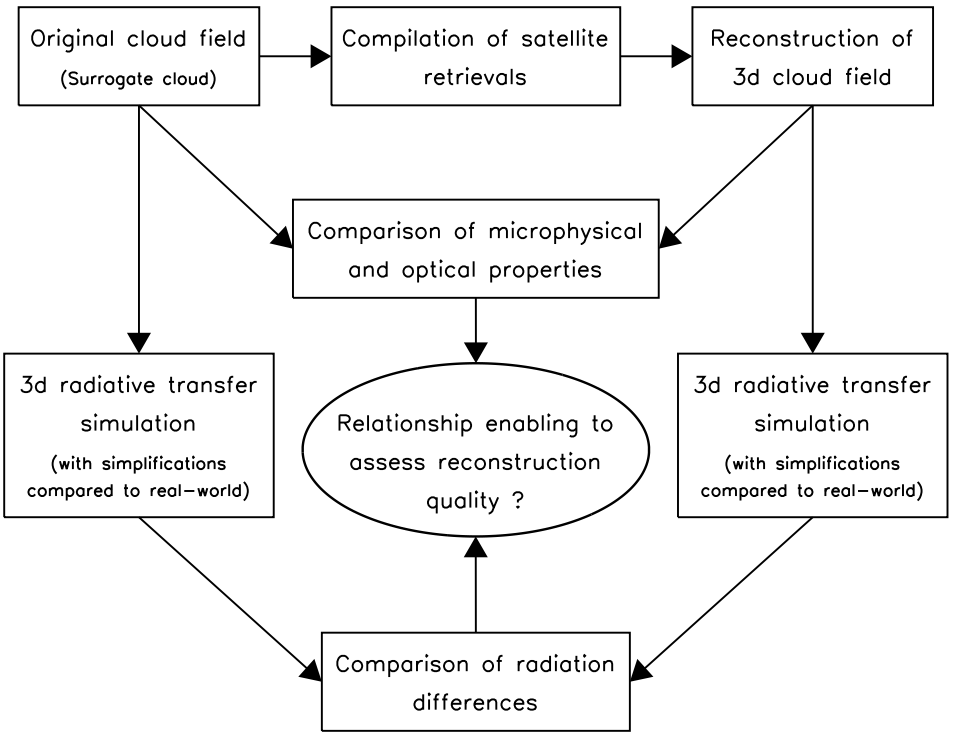

Figure 1.2: Flowchart of this study

grid is the subject of chapter 6. The last chapter includes a summary of the results and gives an outlook on questions for and research requirements of the future.

Chapter 2

Theory

The following chapter presents several theoretical aspects of cloud formation restricted to liquid water clouds. Processes are explained with regard to the development of cloud micro- and macrophysical properties. Methods to derive cloud properties from instruments with varying measurement principles and their limitations are addressed. The theory for the calculation of radiative properties of cloud droplets and the surrounding air is briefly described. Because aerosols play a fundamental role in cloud formation and are added to radiative transfer simulations in a later part of this study, simplified aerosol profiles and their radiative properties are explained, too. Since also a sensitivity study on the influence of surface conditions on the radiative transfer is performed, some aspects of surface reflection functions in the applied radiative transfer code are outlined. This chapter closes with the description of the original Monte Carlo code simulating the radiative transfer and its modifications in order to deal with the present questions.

2.1 Liquid water clouds

Liquid water clouds are a mixture of cloud droplets of different sizes, aerosols which act as cloud condensation nuclei (CCN) if activated, water vapour, and air molecules. If sufficient cloud condensation nuclei are available, cloud droplets will form where the air is cooled below its dew point temperature, called heterogeneous nucleation. The cooling may be caused by the rising of the parcel and adiabatic expansion due to free or forced convection, radiative cooling or mixing of volumes with different thermodynamic properties (Rogers and Yau, 1989). The ability of aerosol particles to act as condensation nuclei is determined by their size and composition depending on the surrounding thermodynamic conditions and the superior suitability compared to other particles of the overall aerosol population.

Due to the limited presence of ice nuclei, which need other properties than cloud condensation nuclei, in about 40 % of clouds with a cloud-top temperature of -10 °C no ice was found (Rogers and Yau, 1989). While some authors (e.g. Giraud et al., 2001) propose a linear relationship between cloud-top temperature and the frequency of occurrence of ice in clouds, other studies claim that the occurrence of ice is also a question of cloud age and drop sizes (Fleishauer et al., 2002).

The environmental conditions like temperature, humidity and the content of aerosols as well as the processes leading to cloud formation like updraft speed and turbulences act on a wide range of spatial and temporal scales. The variability of cloud properties reflects these scales and when comparing properties derived from varying instruments, it is inevitable to specify the sampling volume and also the method data have been recorded with.

Liquid water clouds can be described from observations and for simulation purposes by different measures which are distinguished in macrophysical and microphysical properties. Macrophysical properties quantify cloud geometrical features like cloud fraction, cloud-base, and cloud-top. Microphysical properties like liquid water content, drop size distribution, and effective radius are properties of a certain cloud volume and the result of condensation, mixing, collision, and coalescence. The exceeding of an instrument or model defined threshold of microphysical properties like liquid water path or number density of droplets on the instrument or model resolved scale determines the likewise scale-dependent macrophysical properties.

2.2 Macrophysical parameters

2.2.1 Cloud fraction

Cloud fraction or cloud cover describes the ratio of the cloudy parts to the overall area of an arbitrarily placed projection plane. This plane can be positioned for example parallel to the ground or rectangular to the vector of the incoming radiation or the observation direction. The clouds contributing to the cloud fraction can be the clouds of a certain level or the entire volume. As a parameter used in satellite remote sensing as well as in atmospheric models, overall cloud fraction does not provide any information about the individual layers, cloud sizes, and phases of the clouds contributing to this parameter.

Remote sensing methods of cloud properties not knowing the subgrid cloud fraction and assuming a completely covered pixel underestimate the optical depth of the cloudy area (Oreopoulos and Davis, 1998). Also in single-layer clouds the assignment of subgrid cloud fraction to clouds of different sizes and shapes has an influence on the radiative transfer (Di Giuseppe and Tompkins, 2003).

Assumptions about the underlying cloud field are difficult because it has to be known if cloud fraction is determined by stratiform or convective clouds. If cumulus clouds are present, they may be organized by more or less regular convection. Over land the spatial organization with sizes, shapes, and the pattern of the clouds depends not only on the gridsize thermodynamic properties of the atmosphere but also on local variations of surface properties and the subcloud layer as well as on orographic features. For maritime environments the aforementioned influences reduce due to the rather homogeneous lower boundary conditions. Several investigations have shown some characteristic properties of cloud field organization from measurements (Plank, 1969; Hozumi et al., 1982) or from Large-Eddy Simulations (Neggers et al., 2003) useful for cloud fraction partitioning. As soon as cloud fraction is described as a subgrid layer variable from model output, assumptions about the overlap statistics (Tian and Curry, 1989) of the individual layers have to be made to determine the overall cloud fraction.

For the determination of cloud fraction from satellite as a gridscale quantity, threshold or histogram cluster techniques on one or more channels are applied. The derivation of subpixel cloud fraction is more complex and utilizes information of spatial coherence. Arking and Childs (1985) identified partly cloud-filled pixels in histograms by assuming that completely filled cloud and cloud-free pixels form clusters while remaining scattered data points represent the partly cloudy pixels. Their cloud fraction is determined by the simulation of the radiative properties for the entire pixel using cloud properties from completely filled neighboring pixels. This implies that cloud and surface properties are homogeneous for areas extending the pixel size. Therefore, results are biased due to variabilities already mentioned in the introduction.

From time series of profiling instruments like cloud radars, cloud fraction is calculated as the ratio of time steps with clouds to the entire number of time steps. The comparison of cloud fraction derived from time series with cloud fraction from spatial data is difficult because of the required assumptions about representativity and the averaging techniques applied on temporal as well as spatial data.

2.2.2 Cloud-base and Cloud-top

Cloud-base and cloud-top describe the vertical boundaries of clouds. The definition of the cloud-base is not straightforward and depends on the research requirements (Wang and Sassen, 2001) as well as on the instruments used to determine it. In the present study cloud-base is defined after Platt et al. (1994) as the height above which hydrometeors exist. Accordingly the cloud-base does not have to coincide necessarily with the height where saturation vapor pressure exceeds and condensation in the rising parcel starts. The discrepancy between cloud-base height and condensation level is caused by the mixing of dry air from below and the evaporation of cloud droplets. The mixing of dry air from the surrounding into the cloud is called entrainment (Blyth, 1993). The opposite process, called detrainment, may lead to the same discrepancy: cloudy air of a limited layer is displaced laterally from a vertical extending but horizontal bounded cloud. Profiling instruments may then observe just the detrainend layer, so subsequently cloud-base height and condensation level will differ (Miller et al., 1998). Besides the small-scale nature of entrainment, fluctuations of thermodynamic variables in the subcloud layer and the resulting variations in the condensation level (Wood and Taylor, 2001) are responsible for the variability within an individual cloud. Berendes et al. (1992) present an example where the differences in upward velocity and hence the formation time of droplets can cause higher cloud-bases in the center than at the edge of convective clouds.

Cloud-top in this study is defined as the height above which no hydrometeors exist. In this height thermodynamic buoyancy usually becomes negative and upward motion stops. However, processes like the entrainment of dry air leading to local evaporation of liquid water as well as overshooting from remaining kinetic energy cause variabilities of cloud-top height. The entrainment of dry air into the cloud from the top may originate from turbulence and radiative cooling.

There are several methods for remote sensing of cloud boundaries, both from the ground like radar and ceilometer (Venema et al., 2000), and in-situ with threshold methods applied to radiosoundings (Karstens et al., 1994). If several instruments exist which determine the same parameter, as it is the case for the cloud-base, results may become ambiguous. Because the cloud radar signal is driven by the sixth moment of the drop size distribution, the fallout of large droplets like drizzle will designate the cloud-base though the liquid water content in the drizzle volumes is small compared to the rest of the cloud. The ceilometer detects a higher cloud-base for the same cloud due to the dependence of its signal on the second moment of the drop size distribution. On the other hand the cloud radar may overestimate cloud-base height if drizzle is absent, missing small droplets at cloud-base (Kim et al., 2005). Moreover, evolving clouds with small droplets or clouds below the lowest measurement level might not be detected by the radar. Techniques based on radiosoundings suffer from the ambiguous threshold of relative humidity or spread that is applied to indentify cloudy levels. All results, at least when the profilers are not operating in a scanning mode, are one-dimensional and therefore questionable if extended in horizontal directions.

Various approaches exist to determine cloud boundaries from satellite. Cloud-top height for instance can be deduced from radiances in an infrared window channel (Wylie et al., 1998). This method works for clouds covering the complete satellite pixel, whereas the signal may originate

from inside the cloud if cloud-top is not sufficiently dense (Minnis et al., 1992). The reliability of the atmospheric temperature profile extracted from atmospheric models or radiosoundings is crucial for the conversion of cloud-top temperature to geometrical cloud-top height. Another method less affected by auxiliary data like temperature profiles is the CO_2-slicing technique, where cloud-top is determined from the difference in radiances in a CO_2 window channel and a channel where radiance is absorbed by this species. Because CO_2 is uniformly distributed in the atmospheric column, the difference due to absorption can be employed to derive cloud-top height (Menzel et al., 1983). Additionally there are stereographic methods for either two satellites observing the same cloud field with the same resolution or one satellite which scans the same cloud field from two perspectives without significant changes of the field between the scans (Naud et al., 2005). These methods are fairly reliable, but since the requirements are rarely found, their application seems improper for extended cloud-top observations.

The derivation of cloud-base from space by means of passive instruments is much more difficult than for cloud-tops. The simplest methods determine cloud-base by calculating cloud geometrical thickness from cloud optical thickness while assuming a homogeneous extinction coefficient within the cloudy column (Wilheit and Hutchison, 2000). Advanced methods use relationships between cloud optical and geometrical thickness based on adiabatic cloud profiles (Chambers et al., 1997). In case high-resolution satellite images are available, the cloud-base of broken cloud scenes can be calculated by perspective methods (Berendes et al., 1992). Other approaches assign cloud-base heights from ground based profilers or observers to cloud types and try to recover these cloud types in satellite images to attach the respective cloud-base height (Forsythe et al., 2000).

All methods described here are affected by their assumptions or their limited applicability. Moreover, cloud boundaries will only be available as gridscale properties. But even the small-scale variability of cloud-top has a significant influence on the radiation field especially for large solar zenith angles (Loeb et al., 1998; Richter et al., 2007). Improvements of cloud boundary retrievals from space are expected from active sensors on spaceborne platforms (Stephens et al., 2002), but results will be bound to a narrow segment within the satellite observed area.

2.3 Microphysical parameter

2.3.1 Liquid water content

The liquid water content (LWC) is the amount of liquid cloud condensate within a predefined volume (e.g. gm^{-3}). If enough cloud condensation nuclei (CCN) are available, the LWC is affected by several processes most descriptively explained by a rising air parcel. When the parcel is cooled and its vapor pressure exceeds the saturation vapor pressure, liquid water is released. The amount depends on the spread between the current vapour pressure and the saturation vapour pressure, called supersaturation. If the ascent of the parcel continues, further condensation due to further cooling occurs and additional condensate is added to the parcel. The liquid water content profile is designated as the adiabatic profile if the aforementioned processes are the only processes determining the LWC. The adiabatic profile marks the upper limit of LWC for every level. The vertical gradient of liquid water content $\beta_{ad} = (dW/dZ)$ is calculated after Korolev (1993) as

$$\beta_{ad} = g \left(\frac{LR_m}{C_p R_v T} - 1 \right) / \left(\frac{R_v T P}{E_s} + \frac{L^2 R_m}{C_p R_v T} \right) \tag{2.1}$$

where R_v is the gas constant of water vapour, R_m the gas constant of moist air, g the gravitational

acceleration and L the latent heat of condensation. The parameter C_p is the specific heat of air at constant pressure, E_s the saturation vapor pressure, T the temperature and P the pressure. The ratio between present LWC and adiabatic LWC is called subadiabaticity. LWC values higher than their adiabatic reference value, so called superadiabtic values, are rare and may be found if the measured cloud-base used to calculate the adiabatic reference profile does not coincide with the lifting condensation level (Miller et al., 1998). Chin et al. (2000) analyzed subadiabaticity profiles of stratiform clouds and depicted increased LWC values in lower levels for profiles with drizzle compared to non-drizzle profiles. Though drizzle leads to a significant downward LWC transport in these profiles, liquid water content of the receiving layers does not become superadiabatic. However, other authors (e.g. Miles et al., 2000) consider the contribution of drizzle to the overall LWC as negligible. In the majority of cases the LWC is lower than the adiabatic value due to the mixing of dry air from the boundaries or the decoupling of the cloud layer from the subcloud layer (Korolev, 1993). The rate of entrainment of dry air depends on the turbulence within the cloud environment. Therefore, convective clouds not only have lower subadiabaticity values than stratiform clouds but also exhibit more spatial variability. Horizontal LWC variability is also related to varying updraft speeds leading to varying supersaturation conditions encountered by rising parcels (Rogers and Yau, 1989). According to Blyth (1993), entrainment mainly takes place at cloud-top and cloud-base. Even in cumulus clouds no significant lateral entrainment rates could be found (Warner, 1955). On the other hand Malinowski and Zawadski (1993) account lateral entrainment of eddies with varying sizes to be responsible for the fractal surface of clouds.

Due to the problem to measure LWC profiles, information about subadiabaticity profiles in clouds is rare. The main characteristics of entrainment profiles are the decreasing rates from top and base to the inner parts of the clouds and therefore higher subadiabaticity values within the cloud (Chin et al., 2000). Stephens and Platt (1987) found enhanced LWC variability from cloud-base to cloud-top and assigned this to varying entrainment rates, too.

The average liquid water content within a cloud field is calculated after Räisänen et al. (2003) as

$$\overline{\mathrm{LWC}} = \frac{1}{\mathrm{N}} \sum_{\mathrm{i}} \mathrm{LWC_i} \tag{2.2}$$

where $\mathrm{LWC_i}$ is the liquid water content of the volume i and N is the number of volumes of equal size. Vertical integration of liquid water content as

$$\mathrm{LWP} = \int_{\mathrm{cb}}^{\mathrm{ct}} \mathrm{LWC_z dz} \tag{2.3}$$

yields the liquid water path (LWP) where $\mathrm{LWC_z}$ is the liquid water content of level z, cb is the cloud-base and ct the cloud-top height.

Figure 2.1 illustrates the averaged liquid water content profile of a cloud field used in this study, the corresponding adiabatic LWC profile and the LWC profile following a fitted subadiabatic profile after Chin et al. (2000). The cloud-base for the adiabatic LWC profile and the subadiabatic approximation was estimated as the highest level where all LWC values become subadiabatic.

The liquid water content can be measured with aircraft mounted instruments like the Nevzorov probe and the Particle Volume Monitor (PVM). Korolev et al. (2001) specify a detection threshold of 0.001 - 0.003 $\mathrm{gm^{-3}}$ for the Nevzorov probe, whereas Arends et al. (1994) quote 0.01 $\mathrm{gm^{-3}}$ as the threshold for the PVM. The instruments obtain the highest spatial resolutions mainly depending

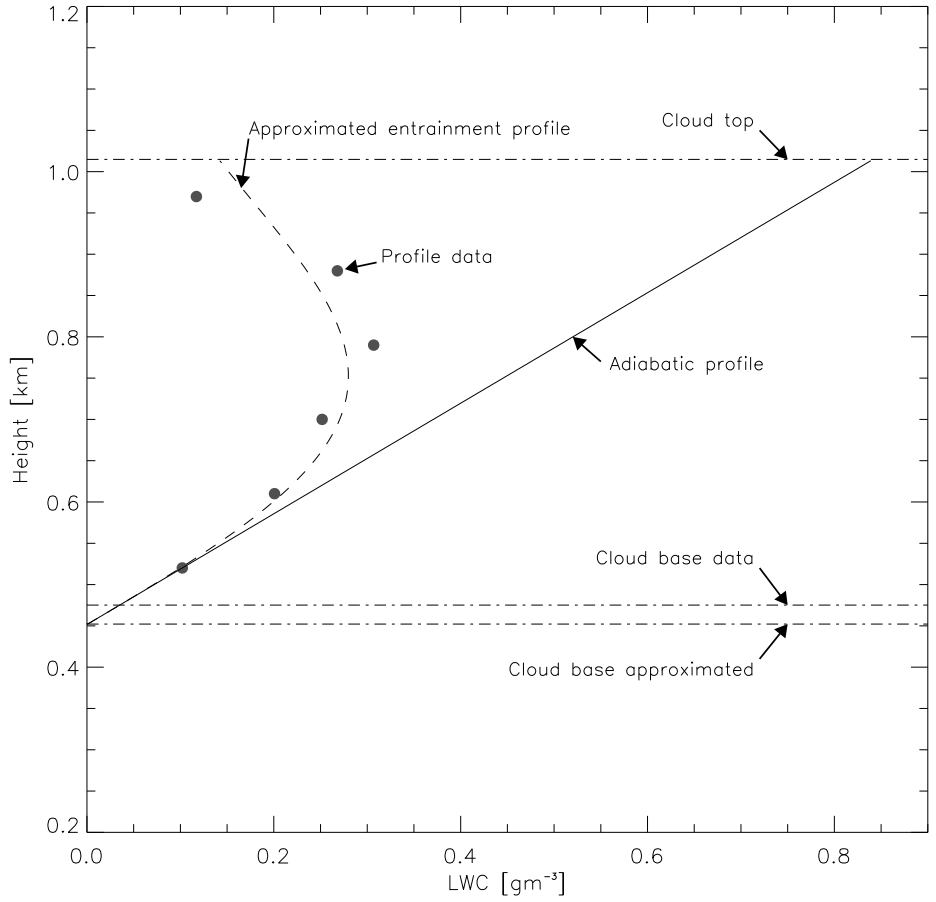

Figure 2.1: Mean liquid water content profile for a cloud field used in this study. The adiabatic profile was fitted by searching for the highest cloud-base so that LWC of all cloud levels becomes subadiabatic or at least adiabatic. Based on this cloud-base a parametrization for subadiabtic profiles was approximated.

on the aircraft speed and the response time of the instrument but fail to measure instantaneous profiles due to the limitation of the instruments to horizontal flight directions.

Remote sensing of liquid water content by satellite is performed either in the solar or in the microwave spectral range. In the solar range optical depth and cloud droplet effective radius are derived from radiances in a shortwave and a near-infrared channel (Nakajima and King, 1990) assuming homogeneous properties within a completely covered pixel and neglecting horizontal photon transport. The substitution of the volume extinction coefficient in Eq. 2.18 with the optical depth, while assuming the effective radius as vertically homogeneous, will result in the liquid water path. When cloud boundaries are known or assumed, the liquid water content can be calculated according to Eq. 2.3 for a cloud column wherein LWC does not vary in vertical direction. Liquid water path can also be inferred from microwave radiometer channels onboard of satellites, but this approach is limited to maritime environments with marginal surface inhomogeneities and is characterized by a rather coarse resolution.

Active instruments as well as combinations of active and passive sensors, which are so far mainly ground-based, have the capability to determine profiles of liquid water content. Fox and Illingworth (1997) found empirical relationships between radar reflectivity and liquid water content. This

approach is biased in the presence of drizzle because of the radar sensitivity to large droplets. A method to derive LWC profiles for stratiform clouds is presented in Frisch et al. (1995) combining a cloud radar and a microwave radiometer. The vertical partitioning of the radiometer-derived liquid water path is accomplished by means of the radar reflectivity, assuming a height invariant drop size distribution. Advanced methods like the Integrated Profiling Technique (IPT) described in Löhnert et al. (2004) combine measurements of several instruments like microwave radiometer, cloud radar, ceilometer and radiosoundings by means of the optimal estimation framework to derive profiles of liquid water content. This approach is so far limited to liquid water clouds without heavy drizzle.

The comparison of liquid water content derived from various instruments and hence the combination of several sources of LWC data is a challenging task because of the highly variable nature of LWC, which is not only determined by the varying scales of turbulence governing entrainment and mixing but also by the spatial heterogeneity of CCN and local drizzle formation with subsequent displacement of liquid water.

2.3.2 Drop size distributions and effective radius

Cloud liquid water is distributed to drops of different sizes. Their number is determined by the number of activated aerosol particles at cloud-base (Brenguier et al., 2000), though secondary activation of cloud condensation nuclei from entrained air during the convection process is possible (Austin et al., 1995). The activation of aerosol particles depends on the aerosol population, namely the number, size and chemical composition of the individual aerosol particles and the encountered supersaturation (Rogers and Yau, 1989). The higher the vertical windspeed in the cloud, the higher the supersaturation due to the response time of the condensation process (Arends et al., 1994) and the more aerosol particles can be activated. However, observational data reveal even in the updraft regions narrow droplet spectra (Austin et al., 1985). Drop size distributions are also influenced by processes like fallout of drizzle, coalescence, mixing of different cloudy air masses, and entrainment.

The process of entrainment may be described by two different mixing schemes; homogeneous and heteorogeneous mixing (Baker et al., 1980). The concept of homogeneous mixing represents the process where all droplets of one layer are imposed to the same saturation deficit because entrained air is spread over the complete layer before the evaporation starts. Here the droplet number remains the same while droplet radii and effective radius, defined in a later part of the chapter, decrease (Arends et al., 1994). If the time of evaporation is shorter than the time needed to mix the entrained air into the whole layer, heterogeneous mixing occurs. Locally all droplets are evaporated whereas the rest of the layer remains unaffected and effective radius is maintained. This scheme induces more variability of liquid water content. Since both schemes represent extremes, consequently stages in between will be found in measurements.

Cloud drop size distributions are mostly positively skewed, though negatively skewed and bimodal spectra have been observed, too. Bimodal drop size distributions are found for example in areas where dry air entrainment resulted in the secondary activation of aerosols. They may also be caused by mixing of different cloud volumes. If drizzle is absent, cloud drop size distributions can be approximated by the lognormal distribution

$$n(r) = \frac{N_d}{\sqrt{2\pi} r \ln \sigma} \exp\left(-\frac{\ln^2(r/r_m)}{2\ln^2 \sigma}\right) \tag{2.4}$$

with $n(r)$ the number of droplets with radius r, N_d the number density, r_m the geometric mean of

the drop radius and σ the standard geometrical deviation of r. Another theoretical distribution to describe drop sizes in non-raining water clouds is the gamma distribution

$$n(r) = ar^{\alpha} exp(-br^{\gamma}) \tag{2.5}$$

with the concentration parameter a, distribution shape parameter α, size parameter b and another adjustable parameter γ. The number density N_d can be calculated as

$$N_d = \frac{a\Gamma(\frac{\alpha+1}{\gamma})}{\gamma b^{\frac{\alpha+1}{\gamma}}} \tag{2.6}$$

where Γ is the Gamma function. If γ is fixed as 1, the distribution is called standard gamma distribution (Lenoble, 1993). The parameter α of the gamma distribution describes the width of the distribution whereas a broader distribution yields a smaller α. This parameter is hard to measure because microphysical instruments are not able to detect small droplets. Brenguier et al. (2003) for example indicate a threshold for the Fast Fourier Scattering Spectrometer Probe (Fast-FSSP) of 1.3 μm. The influence of α has been analyzed by Damiano and Chýlek (1994), who found that radiative properties of droplet ensembles are more dependent on the width of the distribution if wavelength and the effective radius are small.

The parameter α is modified by entrainment because of spectral broadening. Following from this, α varies within the cloud but is assumed as height invariant in most studies. Assumptions of α vary from 2 (Khrgian and Mazin, 1952) to 6 (Deirmendjian, 1969) or 7 (Boers and Rotstayn, 2001). Kokhanovsky (2004a) recommends a value of 6 for small-scale volumes, which was adopted in this study. Several realizations of the standard gamma distribution calculated for varying combinations of microphysical properties are displayed in Figure 2.2.

Important features of the drop size distribution concerning the radiative transfer can be summarized in the effective radius (Hansen and Travis, 1974) which therefore is an important input parameter to radiation parametrizations in climate models (eg. Hu and Stamnes, 1993). It is calculated as

$$r_e = \frac{\int_0^{\infty} \pi r^3 n(r) dr}{\int_0^{\infty} \pi r^2 n(r) dr} \tag{2.7}$$

where r is the radius in the center of the bin of the drop size distribution and $n(r)$ is the number of droplets within this bin. Due to the variable nature of turbulence, effective radius is a function of the observed volume. Liu et al. (2002) found minimum volumes from theoretical investigations whereof effective radius remains constant when the observed volume increases.

Besides the horizontal variability, several types of effective radius profiles were observed. Bower et al. (1994) presented examples of cumulus clouds, where effective radius does not vary vertically. They also found stratiform clouds where effective radius increases with height. If these clouds become too deep, effective radius remains constant from a certain height within the cloud.

There are concepts of adiabatic effective radius profiles for clouds not exceeding a depth of 1 km (Brenguier et al., 2000), where the effective radius profile is determined by the number of activated droplets at cloud-base and the rate of condensation with height during the adiabatic ascent of the

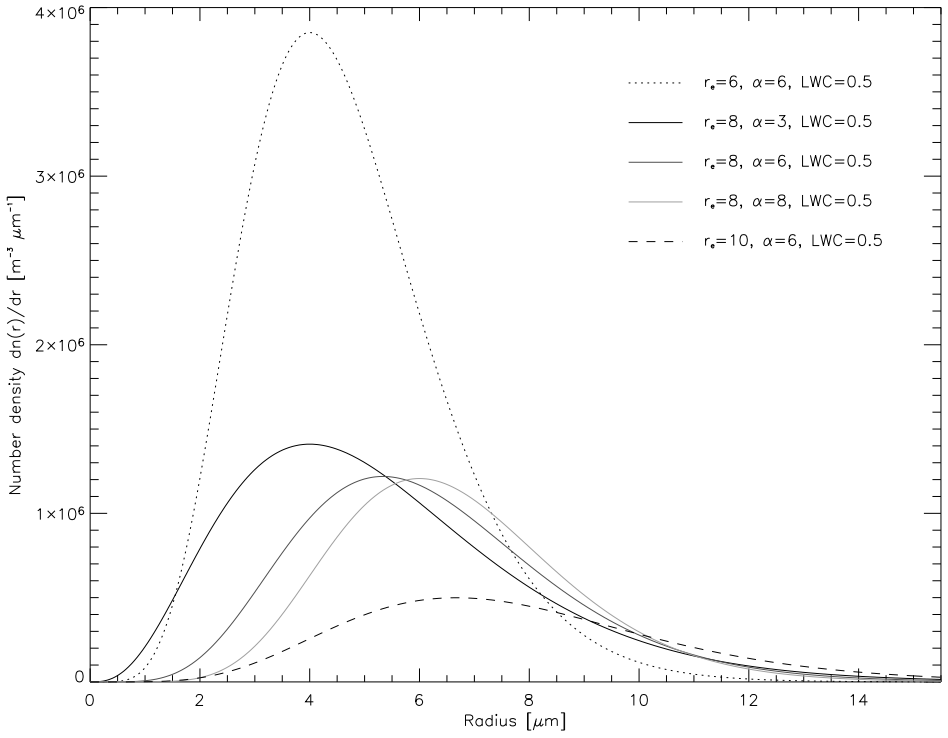

Figure 2.2: Cloud drop size distributions with a fixed liquid water content but varying effective radii and spread.

parcel. When the assumption of inhomogeneous mixing is applied, the profile of effective radius is not modified in entrainment regions. Effective radius is averaged as

$$\overline{r_e} = \sum_i LWC_i / \left(\sum_i LWC_i / r_{e,i} \right) \tag{2.8}$$

(Räisänen et al., 2003) where index i indicates cloudy volumes. Figure 2.3 depicts the profile of the horizontally averaged effective radius of a cloud field employed in this study. Additionally adiabatic effective radius profiles for continental and marine environments have been approximated with parameters given in Brenguier et al. (2000), using the cloud-base displayed in Figure 2.1.

When the drop size distribution is calculated from LWC and effective radius in the present study, following the approach of the microphysics module of Evans (1998), the parameter b in Equations 2.5 and 2.6 is a function of effective radius. Since the parameters α and γ have been fixed to 6 and 1, a and subsequently N_0 are adjusted to retain the predefined liquid water content. This approach contradicts the concept of adiabatic profiles of effective radius with a height invariant number density of droplets.

Besides the measurements with optical instruments like the Fourier Scattering Spectrometer Probe (FSSP), which are capable to monitor small-scale fluctuations of drop size distributions and effective radius, there are several remote sensing methods to obtain the effective radius. Nakajima and King (1990) retrieved effective radius from satellite data by analyzing reflectances in the visible and near-infrared spectrum. Platnick and Valero (1995) found the effective radius derived by this scheme to originate from a certain layer in the cloud when comparing the results with in-situ measurements. This layer is located in the distance of an optical depth of $\sim$2 below cloud-top.

Chang and Li (2002) derived effective radius profiles simulating the radiation for 4 near-infrared channels and one channel in the visible range of MODIS. Their approach minimizes a cost function including observed and simulated radiances to find the best solution. The simulation of the radiances is complicated by the fact that the weighting function for the individual channel and with it the depth inside the cloud where the radiation originates from, depends on the effective radius profile above that layer (Platnick, 2000). This problem is avoided by assuming a linear effective radius profile. Despite this advanced approach it should be mentioned that also remote sensing of effective radius is biased by 3d radiative effects caused by the variability of effective radius in the subpixel and pixel scale (Marshak et al., 2006).

Frisch et al. (1995) applied the method described in the liquid water content section, also for effective radius profile retrievals. To accomplish this, they assumed a fixed droplet number density and a predefined width of the lognormal droplet size distribution, which is most likely for stratiform clouds. Dong and Mace (2003) reduced the assumptions of Frisch et al. (1995) by adding the transmission to the constraints of the algorithm, but limited its applicability to unbroken cloud scenes.

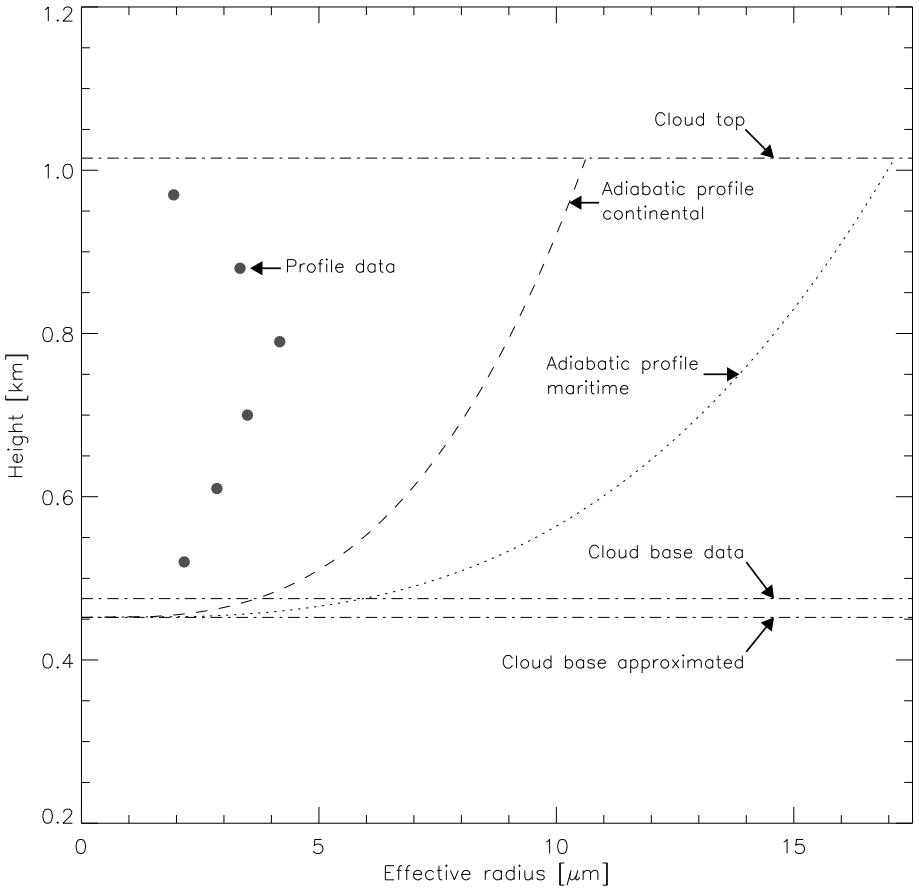

Figure 2.3: Mean effective radius profile of the cloud field presented in Fig. 2.1. The cloud-base for the adiabatic profiles of effective radius profiles was adopted from the approximation of the adiabatic liquid water content.

2.4 Radiative properties and radiative transfer

2.4.1 Radiative properties of clouds

The radiative properties of a cloud volume are described completely by the wavelength dependent extinction coefficient, the single scattering albedo, and the phase function. Henceforth, wavelength indices in formulas are omitted for convenience.

The extinction coefficient β_e is a measure for the attenuation of radiation by scattering and absorption. In cloudy air water droplets, aerosol particles, and air molecules cause scattering. The contribution of scattering to the overall extinction is described by the scattering coefficient β_s. The residual part of extinction is attributed to absorption quantified by the absorption coefficient β_a. In cloudless air attenuation of radiation originates from the scattering of aerosols and air molecules and from aerosol and gaseous absorption within the absorbing range of the spectrum.

The integration of the extinction coefficient between the points s_1 and s_2 of the extinction coefficient, e.g. from the ground to the satellite, results in the optical depth δ calculated as

$$\delta_{(s_1,s_2)} = \int_{s_1}^{s_2} \beta_e(s) ds \tag{2.9}$$

where $\beta_e(s)$ is the local extinction coefficient at position s. The single scattering albedo $\tilde{\omega}$ is calculated as

$$\tilde{\omega} = \frac{\beta_s}{\beta_e} \tag{2.10}$$

and determines the fraction of attenuation caused by scattering.

The phase function determines the angular distribution of scattered radiation or in terms of Monte Carlo radiative transfer simulation the probability that the photon is scattered in a certain direction. Scattering and absorption of cloud droplets and aerosol particles can be calculated using Mie theory (Mie, 1908). The theory assumes that scatterers are homogeneous spheres. This simplification neglects that cloud droplets might enclose an aerosol particle or have a non-spherical form due to the flow around the droplet. Because Mie Theory is limited to spherical scatterers, the phase function is symmetric around the axis of rotation which coincides with the vector of the incoming radiation.

The asymmetry parameter g describes the essential behaviour of the phase function and is calculated as

$$g = \frac{\int_{-1}^{+1} \cos\theta \, p(\cos\theta) d\cos\theta}{\int_{-1}^{+1} p(\cos\theta) d\cos\theta} \tag{2.11}$$

where $p(\cos\theta)$ is the phase function value for the scattering angle θ. The factor describes the main direction of radiation after the scattering event. An asymmetry parameter of 1 means complete scattering in the forward direction, whereas total backward scattering results in an asymmetry parameter of -1.

2.4.2 Radiative characteristics of cloud droplet ensembles

The radiative properties of cloud droplet ensembles with varying drop sizes are computed integrating the quantities of the individual bins of the drop size distribution derived by Mie calculations.

The extinction coefficient β_e of the cloud ensemble is calculated as the integral over the product of extinction efficiency $Q_e(r)$, geometrical cross section πr^2, and the number $n(r)$ of drops with radius r as

$$\beta_e = \int_0^\infty n(r)[Q_e(r)\pi r^2]dr. \tag{2.12}$$

Analogous the scattering coefficient β_s is calculated as

$$\beta_s = \int_0^\infty n(r)[Q_s(r)\pi r^2]dr \tag{2.13}$$

with Q_s the extinction efficiency. The phase function $p(\cos\theta)$ of the ensemble is calculated from the phase function of the individual droplet $p(\cos\theta; r)$ in the following way

$$p(\cos\theta) = \frac{1}{\beta_s}\int_0^\infty n(r)[Q_s(r)\pi r^2 p(\cos\theta; r)]dr. \tag{2.14}$$

The combination of the extinction coefficients of Rayleigh scattering β_{er}, Mie scattering β_{em}, and aerosol scattering β_{ea} results in the overall extinction coefficient β_e

$$\beta_e = \beta_{er} + \beta_{em} + \beta_{ea}. \tag{2.15}$$

The overall single scattering albedo $\tilde{\omega}$ is calculated as

$$\tilde{\omega} = \frac{\beta_{sr} + \beta_{sm} + \beta_{sa}}{\beta_{er} + \beta_{em} + \beta_{ea}} \tag{2.16}$$

with β_{sr} the Rayleigh scattering coefficient, β_{sm} the Mie scattering coefficent, and β_{sa} the aerosol scattering coefficent. The overall phase function $p(\cos\theta)$ for the scattering angle $\cos\theta$ is determined from the phase functions of the constituents by

$$p(\cos\theta) = \frac{\beta_{sr}p_r(\cos\theta) + \beta_{sm}p_m(\cos\theta) + \beta_{sa}p_a(\cos\theta)}{\beta_{sr} + \beta_{sm} + \beta_{sa}} \tag{2.17}$$

where $p_r(\cos\theta)$, $p_m(\cos\theta)$, and $p_a(\cos\theta)$ are the phase function values of Rayleigh, Mie, and aerosol phase function for the scattering angle $\cos\theta$, respectively.
Several approximations of cloud optical properties for radiative transfer calculations are widely used (Räisäinen et al., 2003), for example the approximation of the cloud extinction coefficient β_{cld} as

$$\beta_{cld} \cong \frac{3}{2}\frac{LWC}{\rho_w r_e} \tag{2.18}$$

with LWC the liquid water content, r_e the effective radius, and ρ_w the density of liquid water.

Differences between the extinction coefficient derived from Mie calculations and the approximation 2.18 were calculated for the parameter space defined by the cloud fields used in the present study. Figure 2.4 depicts the deviations and additionally the combinations of LWC and effective radius appearing in the cloud fields. Differences increase for regions with low size parameters, as found by Räisänen et al. (2003).

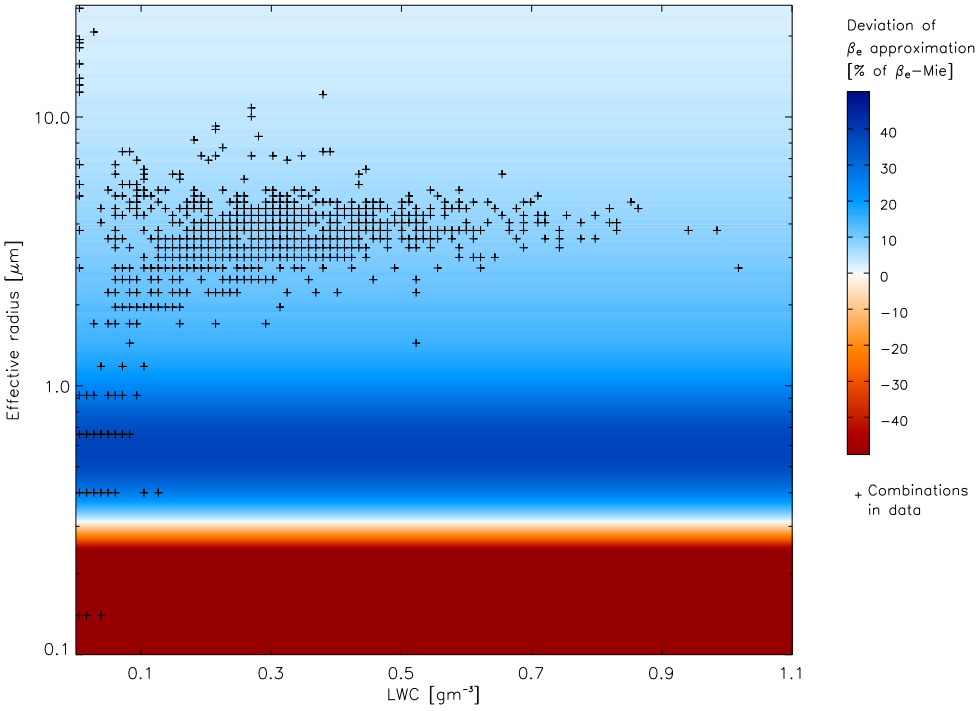

Figure 2.4: Relative differences in the extinction coefficient when instead of complete Mie calculations the approximation of Eq. 2.18 is used. Additionally, combinations of LWC and effective radius arising in the employed cloud fields are plotted. It has to be noted that the combinations have been binned before plotting and the symbol indicates existing values in this bin but provides no information about the frequency.

Besides the treatment of optical properties of cloud droplets, aerosols, and air molecules as bulk properties in Monte Carlo radiative transfer simulations, there are methods to determine the constituent involved in the next scattering event (Barker et al., 2003). The scatterer is selected by a random process where the probability for the individual component is determined by the ratio of its scattering coefficient to the overall scattering coefficient. Radiative properties of the scattering constituent define the scattering process.

2.4.3 Aerosol particles and their radiative properties

The amount and composition of aerosol particles are highly variable in the troposphere reflecting the spatial and temporal variability of natural and anthropogenic sources and transport processes as well as the varying lifetime of particles in the atmosphere (Andrews et al., 2004). Satheesh and Krishna Moorthy (2005) quote the average optical depth of natural and anthropogenic aerosols as 0.055 and 0.050, respectively, whereas the origin of some aerosols is difficult to determine. Aerosol particles originate from man's activities like combustion of fuels and industrial emissions but also plant life and biomass burning, photochemical processes, chemical reactions, wind erosion, sea spray and volcanic eruptions. During their lifetime the chemical composition of aerosol particles may change. Coagulation and coalescence may form mixed nuclei. Also water uptake und evaporation due to the surrounding humidity cause swelling and drying-out of the particles and thus change their size and optical properties.

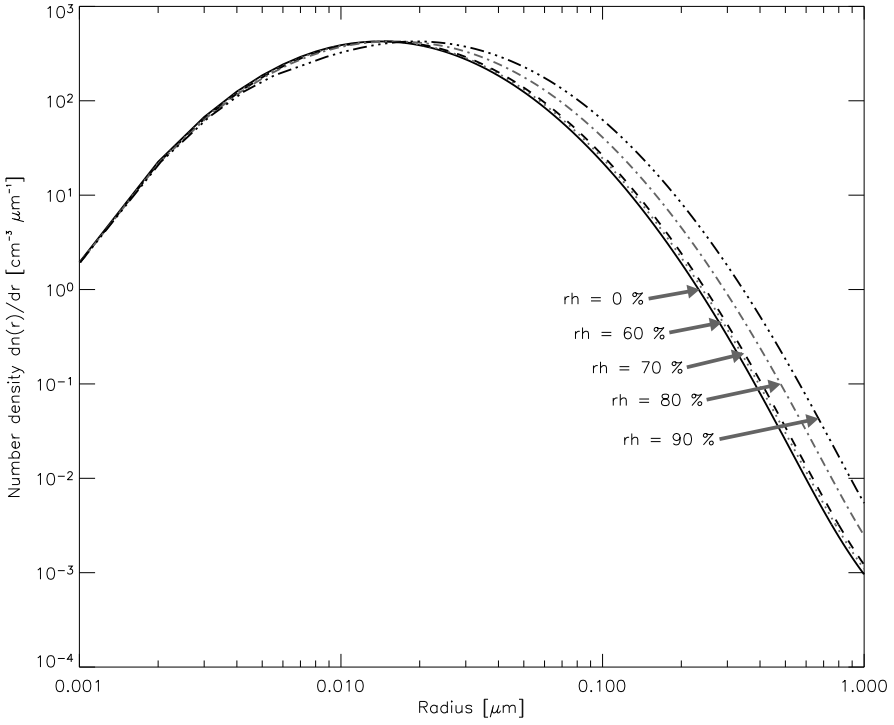

Figure 2.5: Size distributions of a rural aerosol population with a particle concentration of 16780 cm^{-3} for varying ambient humidities.

Aerosols influence the radiation budget in several ways termed as the direct, the first, and the secondary indirect aerosol effect (Boers and Rotstayn, 2001). The direct aerosol effect refers to the reflection of shortwave radiation back to space and the absorption of longwave radiation. Because of the composition of aerosols varying in time and space, the direct aerosol effect may have a heating or cooling effect (Menon, 2004). When additional aerosols become cloud condensation nuclei, modification of droplet size distribution and the decrease of effective radius result in enhanced reflected solar radiation and in a cooling effect, called the first indirect aerosol effect (Twomey, 1977). The second indirect aerosol effect is linked to this effect by the prolonged lifetime of clouds due to the reduction of precipitation efficiency of clouds with smaller droplets (Albrecht, 1989).

For the simulation of optical properties of aerosol profiles their composition has to be known. Only few profile measurements with complete information are available. The composition also determines the water uptake which can cause up to 50 % of aerosol optical depth (Andrews et al., 2004). Figure 2.5 shows the modification of a rural aerosol population due to water uptake applying models of Shettle and Fenn (1979) and Hänel (1976).

Because of the variability of aerosol properties and missing small-scale profile measurements including all parameters required for radiative transfer simulations, radiative transfer studies often employ climatological aerosol profiles (Lenoble and Brogniez, 1984), which consist of mean properties of populations representative for different environments like rural, urban, or maritime. In these profiles different aerosol species are treated as an internal mixture where all particles have the same refractive index. Another approach assumes an external mixture consisting of individual particles of different substances or clusters of mixed composition and individual refractive indices (Yan et al., 2002). When accounting for water uptake of the particles due to surrounding humidity, it becomes obvious that an external mixture is more realistic than an internal mixture because of

the rather irregular growth of particles with mixed composition when humidity increases (Sloane, 1984). In order to determine optical properties for swollen particles two different approaches are conceivable. The first one assumes that the aerosol particle is dissolved in water and forms a homogeneous sphere with a refractive index that is calculated as volume-weighted average of the refractive indexes of water and effective refractive index of the dry internal-mixed aerosol. The assumption that the particles are homogeneous spheres with refractive indices permits the use of an ordinary Mie routine to calculate the optical properties. The second approach accounts for the other extreme, a non-soluble particle enclosed by a coat of water (Sloane, 1984) and applies a coated sphere algorithm to calculate the optical properties (Toon and Ackerman, 1981). Both approaches are simplifications assuming spherical aerosols though these are in the majority of cases non-spherical. This is especially the case if the humidity of the ambient air lies below a threshold which depends on composition and shape of the particle and above which the particle is enclosed by a complete coat (Hänel, 1976).

2.4.4 Rayleigh optical properties

Rayleigh scattering is applied when the scatterers are much smaller than the wavelength of radiation, which is the case for air molecules in atmospheric problems. Petty (2004) quotes a value of 2 for the size parameter χ as the upper limit, calculated as

$$\chi = \frac{2\pi r}{\lambda} \tag{2.19}$$

where r is the radius of the scatterer and λ is the wavelength of radiation. Rayleigh scattering properties are calculated in the present study according to Bucholtz (1995), where the Rayleigh scattering cross section σ of the individual molecule for the wavelength λ is calculated as

$$\sigma(\lambda) = \frac{24\pi^3({n_s}^2 - 1)^2}{\lambda^4 {N_s}^2({n_s}^2 + 2)^2} \left(\frac{6 + 3\rho_n}{6 - 7\rho_n}\right) \tag{2.20}$$

where n_s is the refractive index for standard air and the given wavelength and N_s is the molecular number density ($2.54743 \cdot 10^{19}$ cm^{-3}) for standard air. The depolarization factor ρ_n depends on the wavelength and accounts for the anisotropy of air molecules.

The Rayleigh scattering coefficient $\beta_{sr}(z)$ for the altitude z is calculated from the Rayleigh cross section σ as

$$\beta_{sr}(z) = N_s(z)\sigma \tag{2.21}$$

where $N_s(z)$ is the molecular number density in the altitude z. The Rayleigh scattering phase function $p_r(\theta)$, which has an asymmetry parameter of 0, is calculated after Chandrasekhar (1950) as

$$p_r(\theta) = \frac{3}{4(1 + 2\gamma)}[(1 + 3\gamma) + (1 - \gamma)\cos^2\theta] \tag{2.22}$$

for the scattering angle θ with γ defined as

$$\gamma = \frac{\rho_n}{2 - \rho_n}. \tag{2.23}$$

2.4.5 Surface reflection

The reflection of radiation at the ground is described by the albedo, which depends on the wavelength of the incident radiation and the type of surface. For Monte Carlo radiative transfer simulations the albedo quantifies the probability for an individual photon to be reflected at the surface, or in case of photon parcels the number of reflected and absorbed photons, respectively.

Even in three-dimensional radiative transfer simulations the surface reflection is often simplified applying Lambertian albedo, which does take into account neither the direction of incident radiation nor the angular distribution of scattered radiation. In terms of Monte Carlo simulations the probability of a photon to be scattered or absorbed is independent of its direction of incidence. The hemispheric distribution of the probability for the photon to be scattered in a certain direction is isotropic and with it neither dependent on its direction of incidence nor dependent on the anisotropic surface reflection function.

However, black-sky albedo (Lucht et al., 2000), the angular distribution of scattered radiation for non-diffuse illumination, is a function of the solar zenith angle or the direction of the incident photon. An assumption more close to reality is provided by bidirectional reflectance distribution functions (BRDF). The functions describe the angular distribution of scattered radiation or, in Monte Carlo terms, the probability of a photon to be scattered in a certain direction dependent on its propagation direction before the scattering event and the surface properties. Though efforts have been made to measure BRDFs from space, this approach is limited by the number of observation angles and atmospheric effects. Subsequently, BRDF have to be modeled whereas in most approaches reflection is a function of zenith angle of incident radiation and does not account for anisotropic surfaces.

Within the present study Lambertian albedo was assumed except for simulations analyzed in Section 6.3, where the influence of a bidirectional reflectance distribution function on the radiation results was examined. A random process determines the propagation direction of the photon by means of a cumulated probability distribution function, where the probability of a certain direction is calculated as the ratio of the BRDF value to the black-sky albedo. According to the treatment of Lambertian albedo in the employed radiative transfer model, black-sky albedo determines the weight of the photon after the scattering event or the number of scattered photons of the photon package.

Black-sky albedo $a_{bs}(\theta_0, \lambda)$ for the zenith angle of incident radiation θ_0 and the wavelength λ is calculated as

$$a_{bs}(\theta_0, \lambda) = \frac{1}{\pi} \int_0^{2\pi} \int_0^{\pi/2} R(\theta_0, \theta, \phi, \lambda) \sin(\theta) \cos(\theta) d\theta d\phi \tag{2.24}$$

where $R(\theta_0, \theta, \phi, \lambda)$ is a surface dependent function describing the reflection in zenith direction θ and the relative azimuth direction ϕ. The Lambertian albedo used in the present study corresponds to the white-sky albedo (Lucht et al., 2000), which is calculated from the BRDF by the integration of the black-sky albedo over all directions of incident radiation as

$$a_{ws}(\lambda) = 2 \int_0^{\pi/2} \frac{1}{\pi} \int_0^{2\pi} \int_0^{\pi/2} R(\theta_0, \theta, \phi, \lambda) \sin(\theta) \cos(\theta) \sin(\theta_0) \cos(\theta_0) d\theta d\phi d\theta_0. \tag{2.25}$$

2.4.6 Solar radiation

The spectral range of solar radiation consists of the ultraviolet (UV) band (0.28 - 0.4 μm), the visible band (0.4 - 0.7 μm), and the near-infrared (NIR) band (0.7 - 1.5 μm). Solar radiation quantities are given by the radiant flux Φ [W], which does not provide any information about

wavelength distribution of the radiation or direction of propagation (Lenoble, 1993). In the present study calculations were performed for a single wavelength, so specification of the wavelength for the following spectral quantities by subscript is omitted.

When the dependence of radiation from the direction is considered, the radiance L [$\mathrm{Wm^{-2}sr^{-1}}$] is calculated as

$$L = \frac{d^2\Phi}{d\omega dA} \tag{2.26}$$

where $d^2\Phi$ is the radiant flux within a solid angle $d\omega$ crossing the surface dA which is orientated perpendicular to the axis of the radiation beam. The irradiance F [$\mathrm{W\ m^{-2}}$] is defined as the radiant flux incident on a horizontal plane $dA_\perp$

$$F = \frac{d\Phi}{dA_\perp}. \tag{2.27}$$

The integration of radiance L over the upper hemisphere, defined by the azimuth angles ϕ and the zenith angles θ measured in radiant, yields the downward irradiance $F^\downarrow$ [$\mathrm{Wm^{-2}}$]:

$$F^\downarrow = \frac{d\Phi}{dA_\perp}\bigg\downarrow = \int_0^{2\pi}\int_0^{\pi/2} L(\theta,\phi)\cos(\theta)d\phi d\theta. \tag{2.28}$$

Upward irradiance $F^\uparrow$ is calculated analogously to the downward irradiance $F^\downarrow$ integrating over the lower hemisphere with the convention that this quantity becomes negative. The albedo a is then defined as

$$a = \frac{F^\uparrow}{F^\downarrow} \tag{2.29}$$

whereas albedo is independent of direction except for upward and downward. The reflectance $\rho(\theta,\phi)$ depends on the considered direction of the outgoing radiation and is calculated as

$$\rho(\theta,\phi) = \frac{\pi L(\theta,\phi)}{S_0\cos\theta_0} \tag{2.30}$$

with S_0 the solar irradiance on a plane that is perpendicular to the earth-sun vector and θ_0 the solar zenith angle (Barker et al., 2003).

The radiative transfer for an infinitesimal volume accounting for scattering, absorption, and emission is then described by the radiative transfer equation (RTE) as

$$\mu\frac{dL(\theta,\phi)}{d\delta} = -L(\theta,\phi) + (1-\tilde{\omega})B + \frac{\tilde{\omega}}{4\pi}\int_0^{2\pi}\int_{-1}^{1} p(\theta,\phi;\theta',\phi')L(\theta',\phi')d\theta' d\phi' \tag{2.31}$$

with $\mu = \cos\theta_0$. The parameter δ is the optical depth, $\tilde{\omega}$ the single scattering albedo and B the Planck function. The phase function $p(\theta,\phi;\theta_0,\phi_0)$ describes scattering from the direction defined by zenith angle θ_0 and azimuth angle ϕ_0 into the direction with zenith angle θ and azimuth angle ϕ. The quantity $L(\theta_0\phi_0)$ is the radiance entering the volume from the direction (θ_0,ϕ_0).

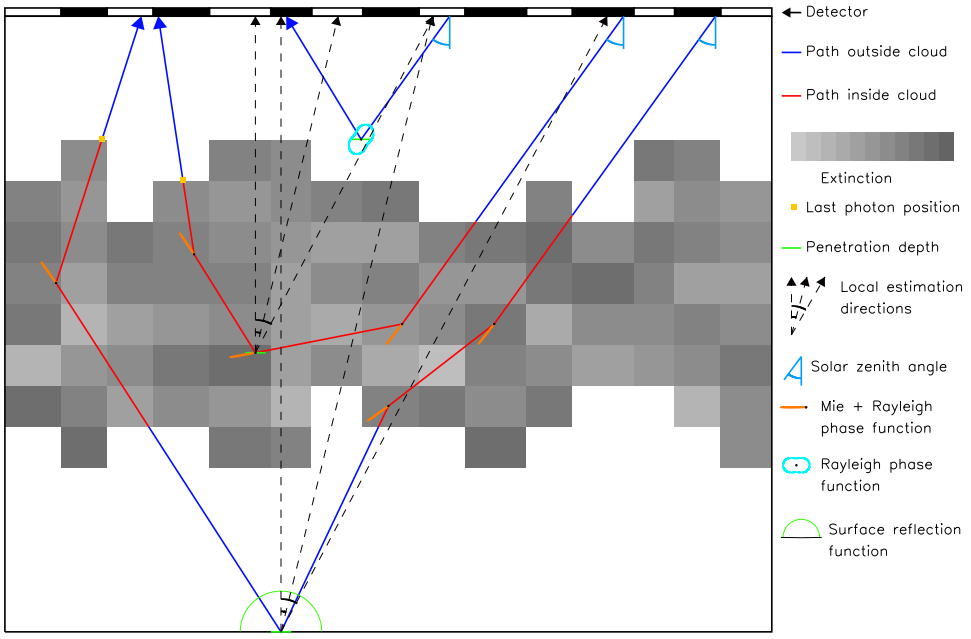

Figure 2.6: Schematic depiction of the Monte Carlo model with the local estimate approach and the added output parameter describing photon path properties.

2.4.7 Radiative transfer modeling

Currently there are two methods widely used to solve the radiative transfer equation for three-dimensional problems (Cahalan et al., 2005): the Spherical Harmonics Discrete Ordinate Method (SHDOM) (Evans, 1998) and the Monte Carlo Method (Marshuk et al., 1980). Both are able to deal with problems with an arbitrary complexity solely dependent on the available computer power.

SHDOM uses an iterative way to compute the source function term of the radiative transfer equation on a three-dimensional grid covering a prescribed volume. The angular part of the phase function is represented by a varying number of spherical harmonics whereas the radiation within the volume is described by discrete ordinates. To deal with highly variable optical properties in space, SHDOM provides the possibility to solve the radiative transfer equation by means of an adaptive grid that can be refined where strong gradients occur.

In the present study the Monte Carlo model MCUnik (Macke et al., 1999), developed at the IFM Geomar in Kiel, was used. The Monte Carlo method is based upon the idea to track photons or packages of photons on their path through the volume, which is determined by the optical properties within the volume but also by the random nature of processes affecting these photons. If the number of tracked photons is sufficiently large, their statistics represent the radiation field. The model MCUnik benefits from handling very large or high-resolution domains by storing the memory-consuming phase functions in a list and assigning the phase functions to the three-dimensional grid by indices. This procedure is preferable to gridded phase functions if several grid cells or stratified areas have the one phase function in common. In spite of this feature, some cloud fields in the present study have been so variable that computational limitations demanded an aggregation of phase functions. The features of the Monte Carlo model are illustrated in Figure 2.6.

In MCUnik photons with a certain weight are released at a random position at the upper boundary of the domain with the direction of propagation determined by the solar azimuth and zenith angle. The pathlength of the photon between two events depends on a random optical depth. The summation of local optical thicknesses along the path determines the geometrical position of the next event. According to the local single scattering albedo, the weight of the individual photon is reduced or, thinking in photon packages, the number of photons is reduced by the number of absorbed photons, respectively. The new direction of the photon propagation is calculated by a random process. The first random number determines the relative zenithal direction from a cumulated probability distribution function derived from the local phase function. The second random number infers the azimuthal direction. When the photon reaches a lateral boundary of the domain, it is inserted at the opposite boundary and continues traveling in the given direction due to the periodic boundary conditions. When the photon hits the ground, its weight is recalculated according to the albedo. Though the reflection function is isotropic assuming Lambertian albedo, photons are forced to propagate in a direction with a zenith angle below a predefined value to avoid crossing the subcloud layer several times. Photons are either tracked until their weights fall below a certain threshold or they enter the detector plane corresponding with the upper boundary of the domain.

If radiances have to be simulated, inappropriate amounts of photons are required to obtain a significant number of photons scattered in the desired direction. Therefore, MCUnik is equipped with the local estimation technique (Marchuk et al., 1980) where during every scattering event secondary photons are released into the predefined radiance directions. The weight of the secondary photon is determined by the primary photon weight and the value of a redistribution function in the radiance direction. The redistribution function can be either a bulk scattering phase function derived from one or more of the phase functions for water droplets, aerosols, and Rayleigh scattering or a function describing surface scattering properties. Secondary photons are not exposed to further scattering events but their weight is lowered according to the optical depth of the path between their release position and the detector. Hence every scattering event contributes to the overall radiance in a predefined local estimation direction with zenith angle θ and azimuth angle ϕ by ζ calculated as

$$\zeta(i,j;\theta,\phi) = \Xi(\theta,\phi;\theta_0,\phi_0) exp\left[-\left|\int_{s_0}^{s} \beta_e(s')ds'\right|\right]. \tag{2.32}$$

Here i and j are the indices of the detector grid cell, Ξ is the normalized redistribution function, s_0 the location of the scattering event, s the position where the secondary photon hits the detector and $\beta_e(s')$ the local extinction coefficient. The propagation direction of the photon before the scattering event is defined by the zenith angle θ_0 and the azimuth angle ϕ_0 (Barker et al., 2003).

Because even secondary photons with small contributions to the overall radiance are time consuming when tracked, several techniques to increase efficiency have been developed, summarized by Iwabuchi (2006). In a common approach the tracking of the secondary photon is stopped if the photon weight falls below a fixed threshold or a threshold determined by a random number when the photon is released. Another method combines the redistribution function value in the desired direction, the weight of the photon, and a random value to determine if the tracking of the photon is skipped. In the applied version of MCUnik, tracking stops if the photon weight falls below a predefined threshold.

Another problem calculating radiances by Monte Carlo models is the sensitivity of the local estimation technique to directions located close to the forward scattering direction of the primary photon. Secondary photons in this direction contribute to the radiance result to a greater extent

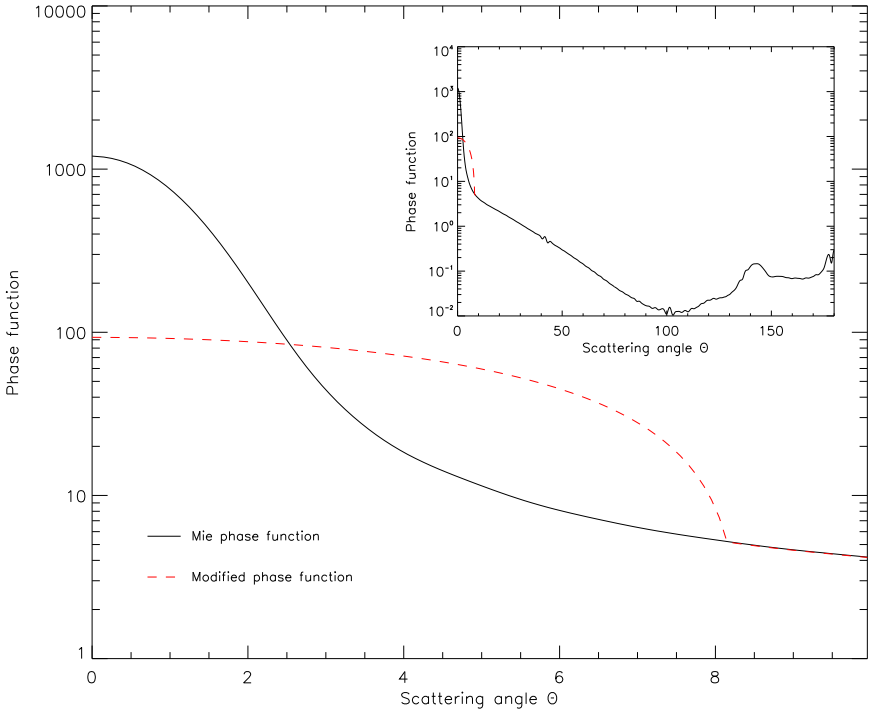

Figure 2.7: Original and modified scattering phase function for an ensemble of water droplets described by an effective radius of 5.21 μm and a LWC of 0.2217 gm^{-3} (wavelength = 0.6 μm)

than other photons but may be sampled infrequently, leading to peaks in the radiation field (Barker et al., 2003). Several variance reduction techniques preclude this effects by modifying the phase function. Iwabuchi (2006) describes approximations where the peaks of the phase function used to calculate the local estimation contributions ζ in forward and backward direction are truncated and redistributed within predefined sections. The extent of these sections is determined by the shape of the original phase function. It has to be noted that phase functions used to derive the propagation direction of the primary photon after the scattering event remain unaffected. In the applied Monte Carlo code only the forward direction is modified (Antuyfeev, 1996), whereas the extension of the redistribution section is independent of the original phase function (Fig. 2.7). Aerosol phase functions are not altered because of their less pronounced peak in forward direction.

A second approach that is implemented in the Monte Carlo model to reduce noisy results due to infrequent sampling has been proposed by Barker et al. (2003). This approach determines a radiation threshold by the local asymmetry parameter of the cloud phase function. In case the radiation entering the detector exceeds this threshold, exceeding radiation is stored into a depot. At the end of the simulation the content of the depot is redistributed to the radiation field according to the spatial distribution of the proportions of overall radiation caused by cloud scattering. Contributions to the radiation caused by aerosol and Rayleigh scattering are not subjected to this redistribution approach.

2.4.8 Modifications of the Monte Carlo model

Several modifications of the Monte Carlo model were made to run it on different operating systems as well as to gain more insight in the radiative transfer through additional output parameters. The

cloud fields of this study do not have an equidistant grid. The assignment of gridcells to the photon path were modified to deal with differing gridcell sizes.

Because simulations with huge amounts of photons are very time-consuming, the model was enabled to deal with splitted jobs and run either on several desktops or on a super computer. Therefore, attention has to be paid that time-initialized random processes of different realizations produce random output. This is accomplished by checking simulation results of splitted jobs for randomness of selected output parameters before merging the data to the overall result.

Because variance reduction methods like phase function modification and redistribution of radiances above a certain threshold are only applied in case of cloud scattering processes, their identification is done by a three-dimensional cloud mask. As a consequence the local estimation contributions are divided in contributions due to cloud scattering and contributions due to Rayleigh or aerosol scattering.

In order to gain more insight in the differences between radiative transfer in several cloud fields, the Monte Carlo code was extended to calculate and store additional parameters like the geometrical and optical pathlength of photons in cloudy areas as well as the deepest altitude photons reached in the domain, called penetration depth (Fig. 2.6). Additionally, horizontal position and weight of primary photons, when leaving the cloud to the detector, may be recorded. With the aid of these parameters it should be possible to get an impression of the region of cloud influence on the radiation signal. A modification, addressing the lower boundary conditions, is the option to use bidirectional reflectance distribution functions instead of Lambertian albedo.

Chapter 3

Data

3.1 4D Clouds and the BBC-campaign

Simulated cloud fields applied in the present study are based on measurements conducted within the framework of the Baltex Bridge Campaign (BBC) thus the campaign is briefly outlined here. Field experiments of BBC were carried out by the groups of the Cloud Liquid Water Network (CLIWA-NET) and the 4D-CLOUDS project in two parts, BBC1 (3-28 September, 2001) and BBC2 (1-31 March, 2003), around Cabauw / Netherlands (51°58'N, 4°55'E). Whereas CLIWA-NET focused on cloud observations and the development of model parametrizations, the 4D-CLOUDS project had the aim to improve the understanding of how the three-dimensional cloud structure influences transport and exchange processes in the atmosphere (Crewell et al., 2004). During the experiments low level boundary layer clouds were observed by groundbased and airborne instruments. Measurements were supplemented by the analysis of satellite data. Seven sites equipped with microwave radiometer and ceilometer were set up in and around Cabauw to obtain spatial information about cloud macro- and microphysical properties. Additionally, three aircrafts performed coordinated flights above, below, and within the clouds when predefined atmospheric conditions arose. Several instruments were mounted on these aircrafts to measure microphysical and radiative properties. Cloud radars, a tethered balloon carrying a platform with instruments to record microphysical properties, an increased frequency of radiosonde launches as well as measurements on several levels of a 213 m tower and on the ground completed the measurements.

Besides the analysis of temporal and spatial variability of cloud and radiative parameters, data were used to compare retrievals of the same parameter by different instruments like LWP from satellite and microwave radiometer. Synergetic use of the data were realized by the Integrated Profiling Technique (IPT), obtaining cloud parameters with an improved quality compared to parameters derived from individual instruments (Löhnert et al., 2004). Results of the IPT served as input data for stochastic cloud models and the obtained cloud fields were used for radiative transfer investigations.

3.2 Simulated cloud fields

The aim of the present study requires three-dimensional cloud fields with a spatial resolution depicting all radiatively relevant scales. Cahalan and Snider (1989) found similar slopes for the power spectrum of radiances and LWP for scales larger than 200-500 m, analyzing Landsat scenes. Below this scale radiative smoothing becomes important. The slope of the radiance power spectrum

differs from the slope of the LWP power spectrum due to decreased small-scale variance caused by horizontal photon transport.

Because three-dimensional measured cloud fields do not exist, it is necessary to simulate them (Evans and Wiscombe, 2004). Several approaches like dynamic modeling by Large-Eddy Simulations (LES) and Cloud Resolving Models (CRM) or stochastic models employing statistical properties derived from measurements are in use.

Large-Eddy Simulations are capable to simulate the boundary layer with high resolution. Domain size of the simulations is limited by computational costs. Cloud fields derived by LES capture lots of macrophysical properties like cloud size distributions (Neggers et al., 2003). Cloud microphysics are either parametrized (Stevens and Lenshow, 2002) or LES models are equipped with explicit microphysical bin models (Khairoutdinov and Kogan, 1999). Whereas models with parametrizations may show varying quality of microphysical results (e.g. Moeng et al., 1996, Chlond and Wolkau, 2000), explicit bin model results are in agreement with measurements at least when comparing average profiles. Cloud fields from Large-Eddy Simulations are widely in use for radiative transfer studies (e.g. Coley and Jonas, 1997).

Cloud Resolving Model resolutions are more coarse than resolutions of LES models (Stevens and Lenschow, 2002) and therefore cover larger domains. Their application is mostly limited to two dimensions omitting one horizontal dimension (Moeng et al., 1996; Randall et al., 2003).

Stochastic models on the other side are capable to generate cloud fields with various predefined statistical properties depending on the complexity of the applied method. The simplest models like the Bounded Cascade models (Cahalan et al., 1994b) and Fourier methods (Barker and Davies, 1992) reproduce a predefined power spectrum of optical depth or liquid water path. Both methods have in common that they do not maintain the probability distribution function of measured values. Power spectra are isotropic in horizontal directions. The vertical distribution of column integrated properties like liquid water path and optical depth is often done by assuming homogeneous profiles.

Adding further constraints becomes difficult when applying these models. Barker and Davies (1992) simulated overcast cloud fields with a predefined power spectrum of liquid water path. To obtain an also predefined cloud fraction, they reduced the LWP in every column by the same value so that the desired number of columns became cloud-free. With this approach the predefined power spectrum is changed. More advanced cloud simulators are capable to deal with these problems and constrain simulations by additional statistics available from measurements. An example for one of these models is the Spectral Idealized Thermodynamically Consistent Model (SITCOM) described by Di Guiseppe and Tompkins (2003), which uses as input parameter beneath predefined power spectra also a vertical profile of subadiabatic liquid water content and an overlap assumption arranging the individual cloud layers.

Cloud fields used in the present study are surrogate cloud fields (Venema et al., 2005) generated by the Meteorological Institute of the University of Bonn. Simulation of these clouds is based on the Iterative Amplitude Adapted Fourier Transformation (IAAFT) described in Schreiber and Schmitz (1996), which reproduces the power spectrum and the probability distribution function of a measured quantity like liquid water content within a certain accuracy. It is described for simplicity and because of its application in a later part of the present study here for two dimensions but is applicable for higher dimensions, too.

The method starts with a probability distribution function and the slope of the power spectrum extracted from one-dimensional measurements. The power spectrum is calculated as

$$E(k) = real(F(k))^2 \tag{3.1}$$

with $F(k)$ the complex Fourier coefficients for the wavenumber k, and $real(\cdot)$ the function which determines the real part. The Fourier coefficients $F(k)$ of a series of temporal or spatial data $f(n)$ are calculated with the forward transform as

$$F(k) = \frac{1}{N} \sum_{n=0}^{N-1} f(n) e^{-i2\pi nk/N} \tag{3.2}$$

where N is the number of measurements in the series and i is the imaginary unit. The real part of the Fourier coefficient determines the amplitude and the imaginary part the phase. In a log-log plot of the power spectrum versus wavenumber k, parameter β describes the slope of a least-square regression line fit and therefore provides no information about phase location.

When a two-dimensional field with isotropic one-dimensional slopes β_{1d} has to be generated, the 2d slope β_{2d} has to be modified. Austin et al. (1994) proposed to use the relation

$$\beta_{2d} = \beta_{1d} - 1 \tag{3.3}$$

or more generally described by Beaulieu et al. (2007) as

$$\beta_{qd} = \beta_{1d} - q + 1 \tag{3.4}$$

where q is the dimension of space.

The IAAFT-algorithm starts with a 2d field filled with the randomly shuffled PDF values and a noise field weighted by the 2d Fourier coefficients. The symmetries to distribute the 2d Fourier coefficients from Eq. 3.3 on the field can be taken for example from Pardo-Iqúzquiza and Chica-Olmo (1993).

In the following iterative two-step procedure, at first the phases of the data field, which might be a random field at the beginning, are determined by a forward Fourier transform. The 2d field of phases is then combined with the amplitudes derived from the noise field weighted by the 2d Fourier coefficients. A backward transform yields the new field of the desired quantity. In the second step the new field is sorted without giving up information of the original 2d location of every value. Sorted values are replaced by the predefined PDF sorted similarly. The new values are redistributed on the 2d grid corresponding to the positions of the values they replace. With this step the power spectrum of the field becomes different from the predefined power spectrum and therefore the procedure continues with the first step. After several iterations the current and the predefined PDF as well as the current and the predefined power spectrum converge and the procedure is stopped.

When applying the IAAFT-algorithm for the generation of surrogate cloud fields, probability distribution functions and slopes of the power spectrum were derived from time series of LWC profiles. These time series were a result of the Integrated Profiling Technique (Löhnert et al., 2004). The height-dependent effective radius for every profile was derived from radar reflectivity and LWP from the microwave radiometer (Frisch et al., 2002). For the simulation of the surrogate cloud fields the liquid water content and the effective radius of every profile level were linked.

Liquid water content often increases with height due to the adiabatic nature of LWC profiles. Because Fourier analysis assumes a periodic behaviour of the time or spatial series, the power spectrum would express these jumps as high power values at high frequencies. To exclude these effects, simulation was performed on residuals calculated as the difference between the LWC gridcell

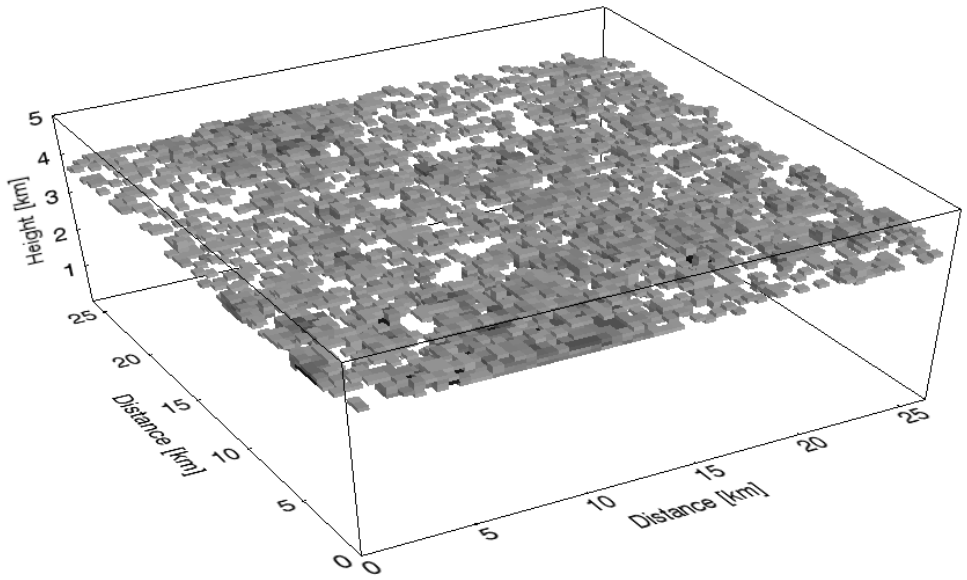

Figure 3.1: Cloud field 1 used in the present study. The extinction coefficient of cloudy volumes is plotted but because of applying an illumination model to enhance the variability of geometrical properties like the cloud-top height a legend is omitted.

values and the mean LWC of the respective layer. At the end of the simulation the 3d grid of residuals and mean LWC profile were summed up. Due to entrainment rates variability of LWC depends on the height in the clouds. To recover these anisotropies of variability in the 3d cloud field, the IAAFT-algorithm uses height dependent PDFs which also assure that cloud-base and top variability are preserved. The 2d Fourier coefficients derived from the time series of profiles of LWC-residuals were scaled to receive a horizontal isotropic power spectrum with the predefined slopes. Following this, modified 2d Fourier coefficients were distributed on a 3d grid and the IAAFT procedure was performed.

Linked effective radii were assigned to the gridcells with the respective LWC to obtain a 3d grid of LWC and effective radius. This approach implies a certain correlation of liquid water content and effective radius, which might be found in profiles where structures of adiabatic LWC and effective radius profiles still exist but cannot be found in airborne microphysical measurements. Evans and Wiscombe (2004) also used this linkage for their stochastic cloud generator.

Surrogate cloud fields have been available in the time domain and were transformed into the space domain by applying the wind speed at cloud-base. The Figures 3.1 and 3.2 present surrogate cloud fields employed in the present study. The figures show the extinction coefficient of cloudy volumes. Because an illumination model was applied to highlight the variability of cloud geometrical properties a legend is omitted.

3.3 Description of surrogate cloud fields

This section describes 8 surrogate cloud fields selected for this study because of their variety of statistical properties. For quality assessment macro- and microphysical properties of the surrogate cloud fields were compared with observations described in the literature. Several of these properties may have the potential to be used as constraints for cloud field reconstruction. It has to be noted that most statistics presented in this section are scale dependent (Fomin and Mazin, 1998) and

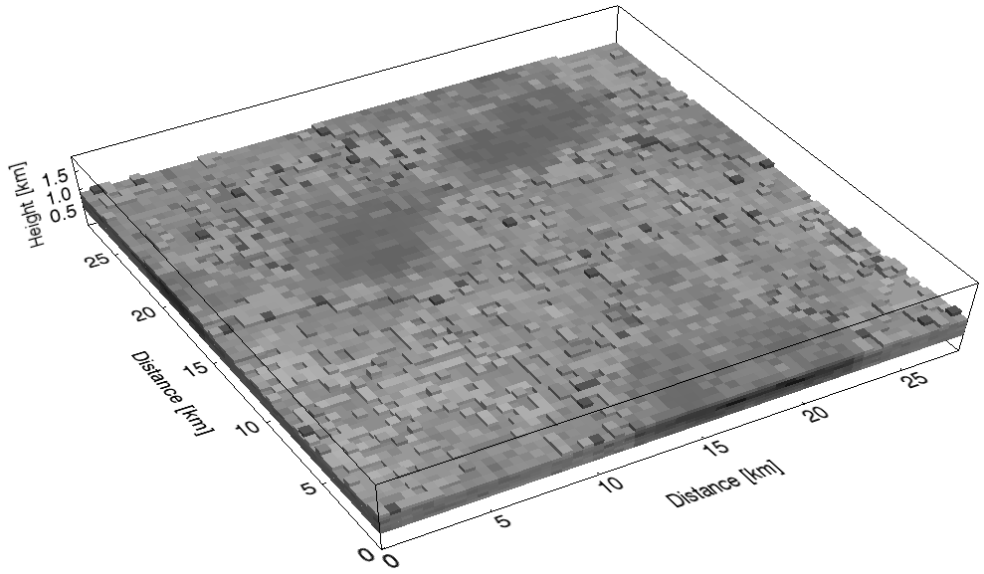

Figure 3.2: Cloud field 8 used in the present study. The extinction coefficient of cloudy volumes is plotted but because of applying an illumination model to enhance the variability of geometrical properties like the cloud-top height a legend is omitted.

therefore comparison in the strict sense requires the same resolution of the data. This demand is not realized in this investigation.

Figure 3.3 gives a first impression of the cloud fields by means of their cloud optical depth. All cloud fields were reconstructed from data of the BBC2 campaign and consist of liquid water clouds. The horizontal resolution of the cloud fields ranges from 0.24 to 0.48 km due to the wind speed at cloud-base whereas cloud gridcells are not equidistant and show slight deviations from the mean length of up to 3 %. The vertical resolution differs between cloud-free areas and cloudy areas with mean resolutions of 0.089 km and maximum deviations of 1.6 % from the mean for the cloudy levels. Though cloud cells are not equidistant, some statistical properties in this chapter assume cloud cells of the same size. In that case it is indicated in the text.

Some statistics of cloud macrophysical properties of the used cloud fields are presented in Table 3.1. In the majority of cases cloud-base variability exceeds cloud-top variability, corresponding to the results of Considine et al. (1997) for marine boundary layer clouds formed below a strong capping inversion. Kim et al. (2005) found similar values for cloud-top and cloud-base variability but also higher cloud-top variability analyzing continental liquid water clouds.

Especially cloud fields 2 and 3 are characterized by lots of multilayer cloud columns. Beneath the problem of multilayer detection by passive instruments, these columns pose a problem for cloud reconstruction. Though concepts to estimate cloud hole statistics for the entire field from transects by making assumptions of the cloud hole shapes exist (Korolev and Mazin, 1993), modeling of cloud-free layers is difficult and therefore neglected in most cloud simulations.

When cloud geometrical thickness has to be estimated for cloud field simulations two approximations are in use, both deriving thickness from cloud optical depth by adabatic profile assumptions. The first one estimates cloud geometrical thickness Z as $Z \backsim \delta^{0.5}$ (Chambers et al., 1997) and the second one as $Z \backsim \delta^{0.6}$ (Pawlowska et al., 2000), where δ is cloud optical depth. Comparing the mean geometrical thickness of the surrogate cloud fields with the thickness obtained by these approximations applying the mean optical depth, cloud fields are at least 3.2 km and up to 12 km

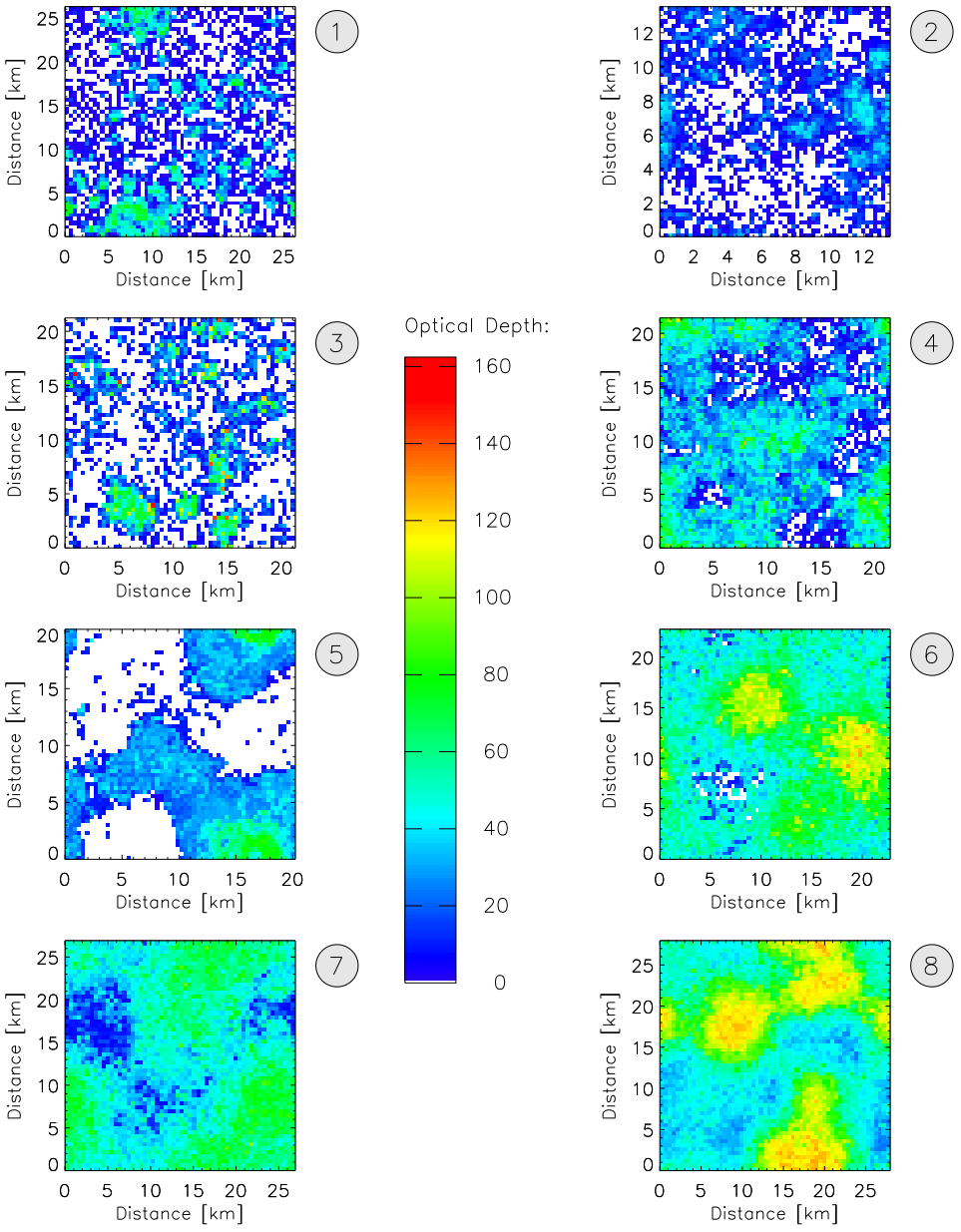

Figure 3.3: Zenithal projected cloud optical depths of all surrogate cloud fields.

Table 3.1: Cloud-top, cloud-base and cloud layer statistics

Field	Cloud-base		Cloud-top		Max #	Multilayered
	Mean	Std.Dev.	Mean	Std.Dev.	Cloud	Cloud Col.
	[km]	[km]	[km]	[km]	Layers	[% of Cloudy Col.]
1	3.771	0.076	3.953	0.092	2	7.59
2	3.029	0.192	3.295	0.146	3	27.82
3	2.127	0.156	2.388	0.095	3	14.10
4	2.156	0.068	2.385	0.064	3	9.44
5	2.179	0.062	2.413	0.055	2	6.21
6	2.198	0.034	2.539	0.019	2	0.06
7	0.543	0.067	0.984	0.047	3	4.52
8	0.475	0.000	0.965	0.055	2	0.38

thinner than their respective approximations. It has to be noted that cloud thickness for this comparison was calculated as the sum of cloudy cells height and not as the distance between cloud-top and cloud-base. As it will be demonstrated below, cloud liquid water content is far from adiabatic and according to this differences between cloud fields and approximations are caused by effective radii below their adiabatic reference values.

Iwabuchi and Hayasaka (2002) scaled local geometrical cloud thickness Z by local cloud optical depth δ and domain averages of these parameters employing the relation

$$\frac{Z}{\sqrt{\delta}} = \frac{\langle Z \rangle}{\langle \sqrt{\delta} \rangle} \tag{3.5}$$

found by Minnis et al. (1992) where $\langle \cdot \rangle$ denotes the domain average. The differences between standard deviation of cloud thickness approximated by Eq. 3.5 and observed standard deviation range between -0.041 and 0.052 km, which is quite high compared to the standard deviations of cloud boundaries in Table 3.1.

The cloud fraction calculated for several perspectives is summarized in Table 3.2. Calculation was done by tracking rays, released with a regular pattern of starting points from a plane orientated parallel to the ground. If a ray hits a cloudy cell, cloud fraction increases by the weight of the ray which depends on the number of rays released. Determination of cloud fraction in this way requires a sufficient amount of rays to capture small cloudy or cloud-free areas. Cloud fields are treated as periodic in horizontal directions to avoid effects where rays leave the domain on the edges without hitting a cloud leading to the underestimation of the overall cloud fraction. It becomes evident that cloud fraction increases mostly for scattered cloud fields when the zenith angle of the tracked rays increases. Because of the small vertical extent of broken cloud fields, increase of cloud fraction with increase of zenith angle is moderate. From these results there is no evidence for significant differences between the Independent Pixel Approximation and the Tilted Independent Pixel Approximation (TIPA), where independent columns are aligned along the ray of solar incidence (Várnai and Davis, 1999). Furthermore, internal cloud structure may have the potential to counteract cloud fraction increase.

Miles et al. (2000) compiled measurements of microphysical properties of many aircraft campaigns and found weak evidence for the determination of the origin of clouds by analyzing the

Table 3.2: Cloud fraction for different perspectives with a azimuth angle of 0° and zenith angles of 0°, 30° and 60°

Field	Cloud fraction 0°	Cloud fraction 30°	Cloud fraction 60°
1	0.65	0.68	0.74
2	0.64	0.71	0.79
3	0.53	0.56	0.63
4	0.91	0.92	0.95
5	0.56	0.57	0.59
6	0.98	0.99	0.99
7	1.00	1.00	1.00
8	1.00	1.00	1.00

combination of mean effective radius and mean liquid water content (Fig. 3.4). The combinations of surrogate clouds indicate that though the experiment site may be influenced due to its distance to the ocean by maritime air masses, too, surrogate cloud fields are likely of continental origin. Figure 3.4 also makes clear that mean effective radius values of surrogate cloud fields are very low compared to the in-situ measurements.

Figure 3.5 presents a density plot of appearing microphysical combinations of LWC and effective radius for cloud field 4. Gultepe et al. (1996) found high correlations for individual marine stratus clouds, which might be intuitive having adiabatic models with minor modifications due to entrainment in mind. Korolev et al. (2001) observed rather low correlations between liquid water content and effective radius in continental clouds above freezing temperature but reported an increase of correlation with decreasing temperature. The correlation coefficients for the surrogate cloud fields range between -0.03 and 0.71. From this figure a feature becomes obvious, which can be found in several surrogate clouds: the existence of cloud volumes with very high effective radii but low values of liquid water content and vice versa. To reveal additional characteristics of the surrogate clouds, cloud volumes were identified that in-situ measurement devices would not report as cloudy. Therefore, the detection threshold of the Nevzorov probe as a device for liquid water content was assumed to be 0.001 gm^{-3} (Korolev et al., 2001) and also volumes with effective radii below 1.3 μm as the detection threshold for the Fast-FSSP (Brenguier et al., 2003) were treated as cloud-free. Applying these thresholds cloud volume reduces by 3 - 37 % of the original volume and vertical projected cloud fraction by up to 46 %. Mean liquid water path and optical depth are 1 - 7 % and 1 - 43 % lower than the original values, respectively. Nearly all reductions are attributed to the effective radius threshold.

Simulating cloud radar results for the surrogate clouds reflectivity factor Z was calculated due to Rogers and Yau (1989) as

$$Z = \sum_{V} D^6 = \int_0^\infty N(D) D^6 dD \tag{3.6}$$

for every gridcell with volume V. The parameter D is the droplet diameter and $N(D)$ is the number of droplets in the drop size bin derived for a standard gamma distribution with $\alpha = 6$. The radar received power is expressed in logarithmic units as

$$Z(dBZ) = 10 \log Z \tag{3.7}$$

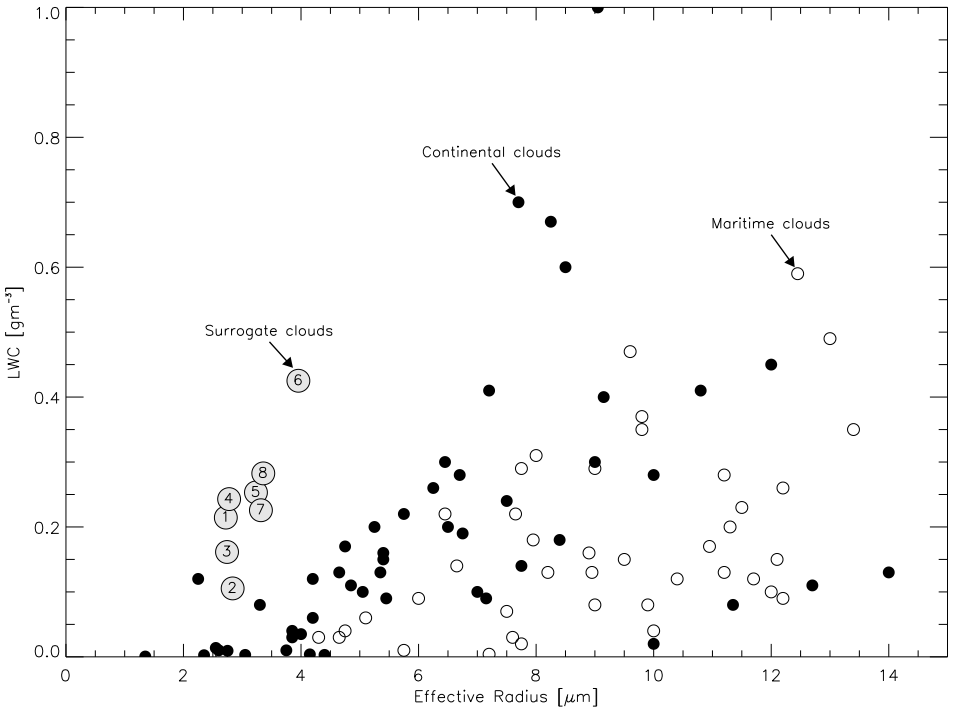

Figure 3.4: Combinations of mean LWC and r_e for maritime and continental clouds from the Miles-compilation and the surrogate cloud fields.

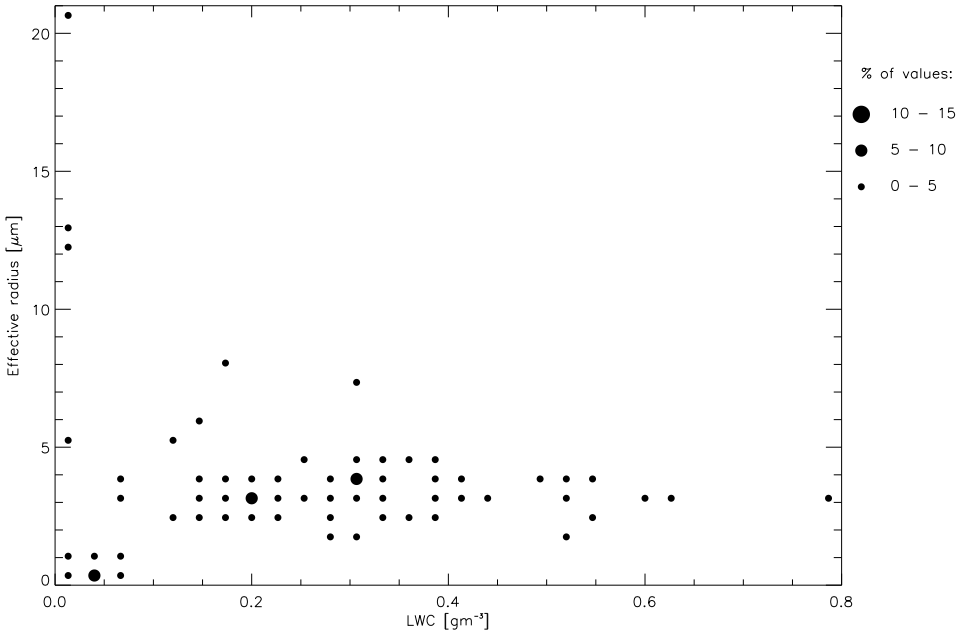

Figure 3.5: Density of the combinations of LWC and r_e appearing in cloud field 4.

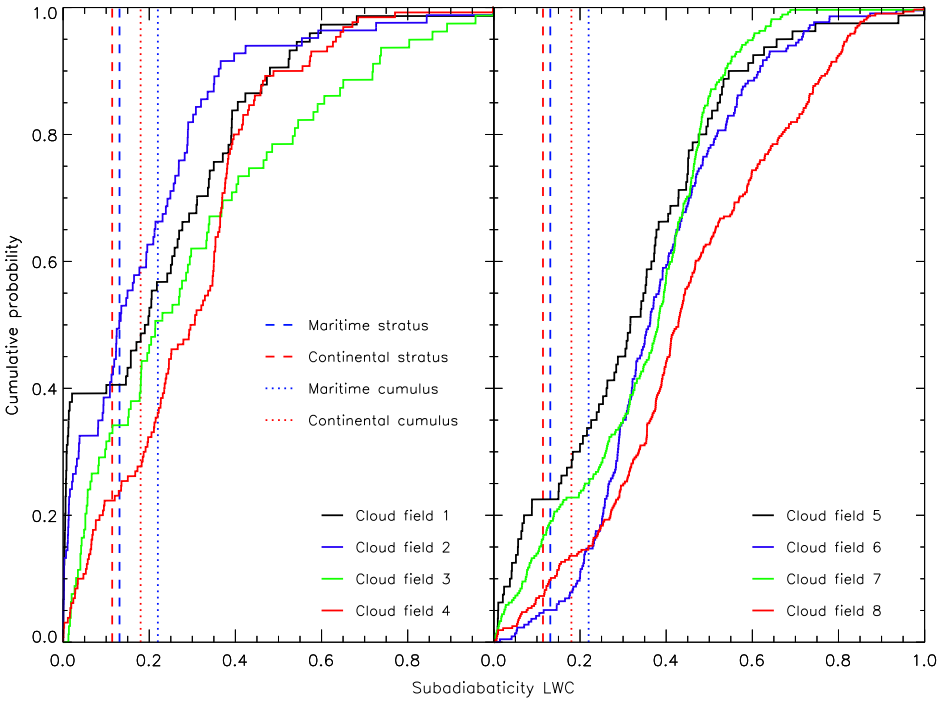

Figure 3.6: Cumulative PDFs of subadiabaticity of LWC for the surrogate cloud fields. Additionally, mean subadiabaticity values for several cloud types derived from microphysical measurements are plotted for comparison.

where Z is commonly specified in mm^6m^{-3}. The height and setup dependent thresholds of a 35.5 GHz radar operated at the Meteorological Observatory of the German Weather Service in Lindenberg/Germany were applied to classify cloud volumes that would not be detected by the radar. Simulations reveal that cloud volumes reduce by 8 - 68 %, cloud fraction by 0 - 53 %, mean LWP by 2 - 43 %, and mean optical depth by 4 - 61 % of the original values. It has to be noted that mean liquid water path and optical depth were been calculated for the threshold fields as averages of the entire cloud field including cloud-free columns.

The findings provide an indication for high entrainment rates and low subadiabaticity values. Estimating cloud-base as in described in chapter 2 so that all LWC values do not exceed their adiabatic reference, adiabatic LWC profiles and adiabatic effective radius profiles for continental clouds and corresponding subadiabaticity values for every cell were calculated. Cumulative PDFs of subadiabaticity for LWC are shown in Figure 3.6. Mean values of microphysical measurement campaigns of maritime and continental stratus (Yum and Hudson, 2002) and cumuli (Hudson and Yum, 2001) were added for comparison. It becomes obvious that subadiabaticity values agree well with in-situ measurements like LWC values in Fig. 3.4 for cloud fields 1 to 4 but differ markedly for cloud fields 5 to 8. Cumulative PDFs of effective radius subadiabaticity (Fig. 3.7) were derived by adopting the LWC cloud-base and a continental adiabatic effective radius profile following Brenguier et al. (2000). These PDFs show besides low subadiabaticity values also superadiabatic values giving a clue that cloud-base was estimated too high.

As a consequence of the inhomogeneous nature of entrainment Räisänen et al. (2003) expect increasing variability of liquid water content from cloud-base to cloud-top, found by Stephens and

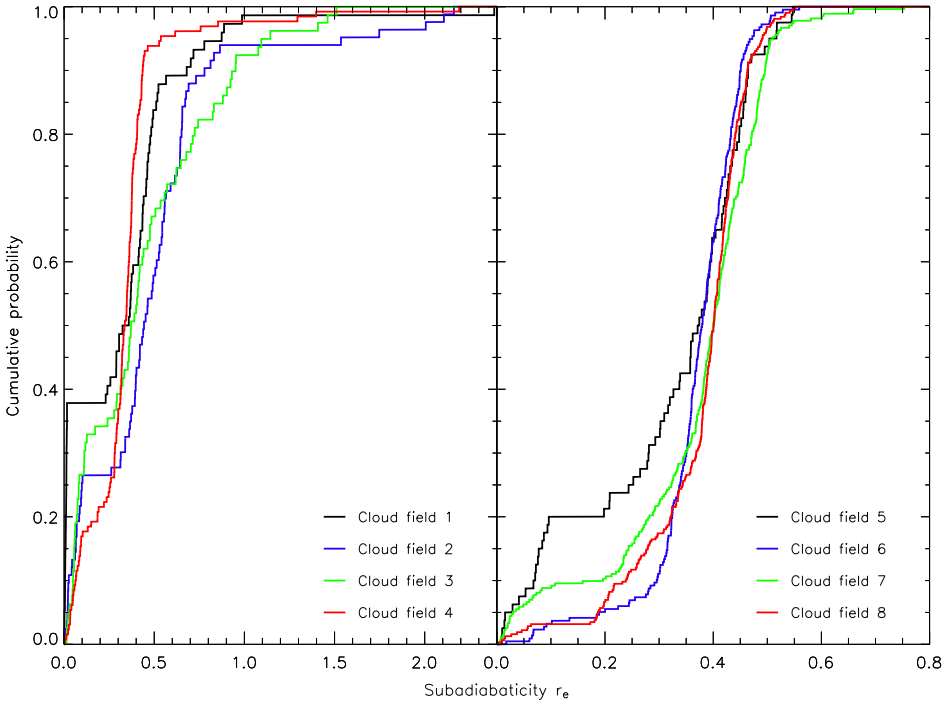

Figure 3.7: Cumulative PDFs of the subadiabaticity of r_e for the surrogate cloud fields. Reference adiabatic values were calculated applying the continental model of Fig. 2.3.

Platt (1987) in maritime stratocumulus and cumulus clouds. Figure 3.8 presents profiles of the standard deviation for the LWC. The scaled height in this plot is the height above cloud-base normalized by the distance between mean cloud-base and cloud-top. Some of the cloud fields show the expected variability whereas the uppermost level is affected by cloud-top variability and therefore might show reduced LWC variability.

In chapter 2 it has been noted that effective radius derived from satellite data is approximately the effective radius in the distance of 2 optical depth below cloud-top. When remotely sensed effective radius is compared with the mean effective radius of the column, mean differences for cloud fields range from -0.74 to 0.46.

The extinction coefficients of the surrogate cloud fields were computed performing complete Mie calculations with a standard gamma drop size distribution. Figure 3.9 presents the cumulative probability distribution functions of extinction coefficients. Observations of continental clouds from aircraft campaigns compiled by Korolev et al. (2001) were added whereas the cumulative PDF was derived for clouds with temperatures between 0 and 10 °C. Korolev et al. (2001) reported the maximum detected extinction coefficient to be 320 km^{-1}. Figure 3.9 makes clear that extinction coefficients of surrogate cloud fields are considerably high mainly due to low effective radii.

The vertical integration of liquid water content yields the liquid water path. Kim et al. (2005) found for continental liquid water cloud fields increasing standard deviations of LWP with increasing mean LWP. Table 3.3 provides no evidence for such a relation for the surrogate cloud fields. Kim et al. (2005) fitted a distribution to observations for description of LWP variability within

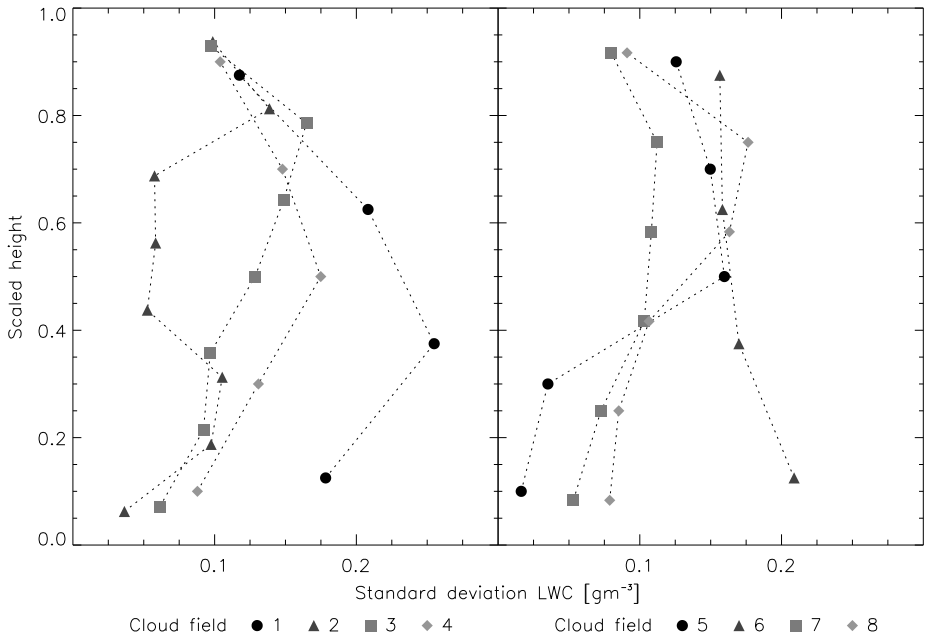

Figure 3.8: Standard deviation of the liquid water content of the surrogate cloud fields in different layers.

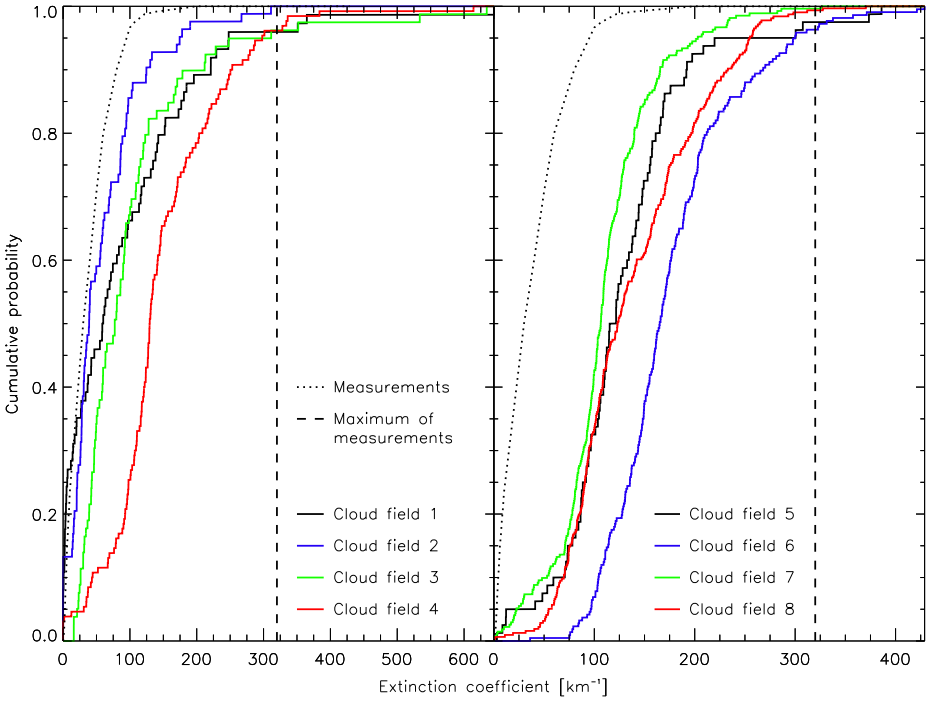

Figure 3.9: Cumulative probability density function of extinction coefficient for the surrogate cloud fields. For comparison values of a compilation for continental clouds from airplane campaigns are added.

Table 3.3: Liquid water path statistics

Field	Mean LWP	Standard Deviation LWP
1	37.41	44.42
2	21.61	21.88
3	38.55	51.36
4	53.28	34.79
5	57.65	36.46
6	144.88	60.91
7	98.61	35.39
8	138.42	59.34

the field. The distribution is intended for parametrization in models. The probability $P(LWP)$ of LWP is calculated as

$$P(LWP) = \frac{1}{\sqrt{4\pi\Gamma'\sigma_h^2 LWP}} \exp\left\{-\frac{\{LWP^{1/2} - (\overline{LWP} - \Gamma'\sigma_h^2/2)^{1/2}\}^2}{\Gamma'\sigma_h^2}\right\} \tag{3.8}$$

where Γ' represents the rate of LWC increase with height h. The parameters σ_h and $\overline{LWP}$ are standard deviation of cloud thickness and mean LWP, respectively. Liquid water path and cloud thickness h are related according to Kim et al. (2005) by

$$LWP = \Gamma' h^2/2. \tag{3.9}$$

The parameter Γ' is obtained from the slope of a regression line fitted to the plot of LWP versus the square of cloud thickness. While Kim et al. (2005) used data of profiler time series for the plot and compared results of the parametrization with the same time series, the present study uses the extracted transects employed in a later part of the study for cloud field reconstruction to derive Γ' but also for determining $\overline{LWP}$ and σ_h in Eq. 3.8. With this approach the potential of applying the approximation as a constraint for cloud field reconstruction is investigated. Observed and modeled liquid water path PDFs for the surrogate cloud fields are plotted in Figure 3.10. It becomes obvious that LWP distributions of surrogate cloud fields do not follow the distributions described by the parametrization. Furthermore, multimodal distributions appear which are not a consequence of the bin size. Due to the observed multimodal PDFs, values of Table 3.3 have to be treated with caution.

Analogous to the parametrization of LWP variability, Barker et al. (1996) applied a gamma distribution to model optical depth variability. The probability $P(\delta)$ of optical depth δ is calculated as

$$P(\delta) = \frac{1}{\Gamma(\upsilon)} \left(\frac{\upsilon}{\overline{\delta}}\right)^{\upsilon} \delta^{\upsilon-1} \exp^{-\upsilon\delta/\overline{\delta}} \tag{3.10}$$

where $\upsilon = (\overline{\delta}/\sigma)^2$ with $\overline{\delta}$ and σ as the mean and standard deviation of δ, respectively and $\Gamma(\upsilon)$ the gamma function. It has to be noted that Equation 3.10 and also Figure 3.11 include only values of cloud optical depth greater than 0. In contrast to the LWP parametrization the parameter for the optical depth parametrization were derived for the entire cloud field. Figure 3.11 shows a reasonable fitting of the parametrization for the unimodal distributions but bimodal PDFs are not

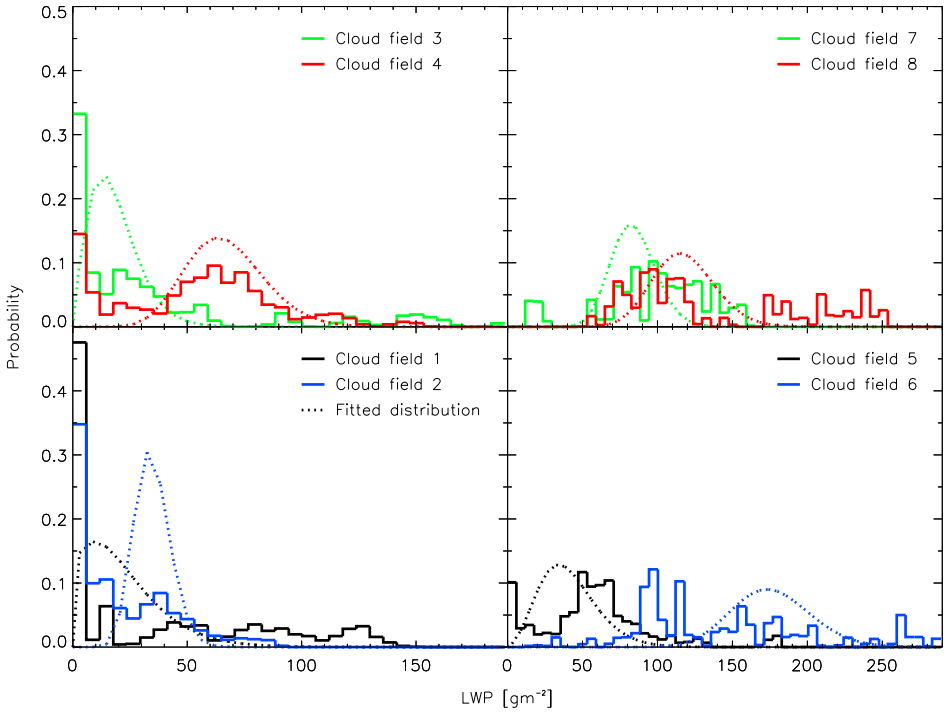

Figure 3.10: Probability distribution functions of the liquid water path for the surrogate cloud fields and approximations derived from the respective slices.

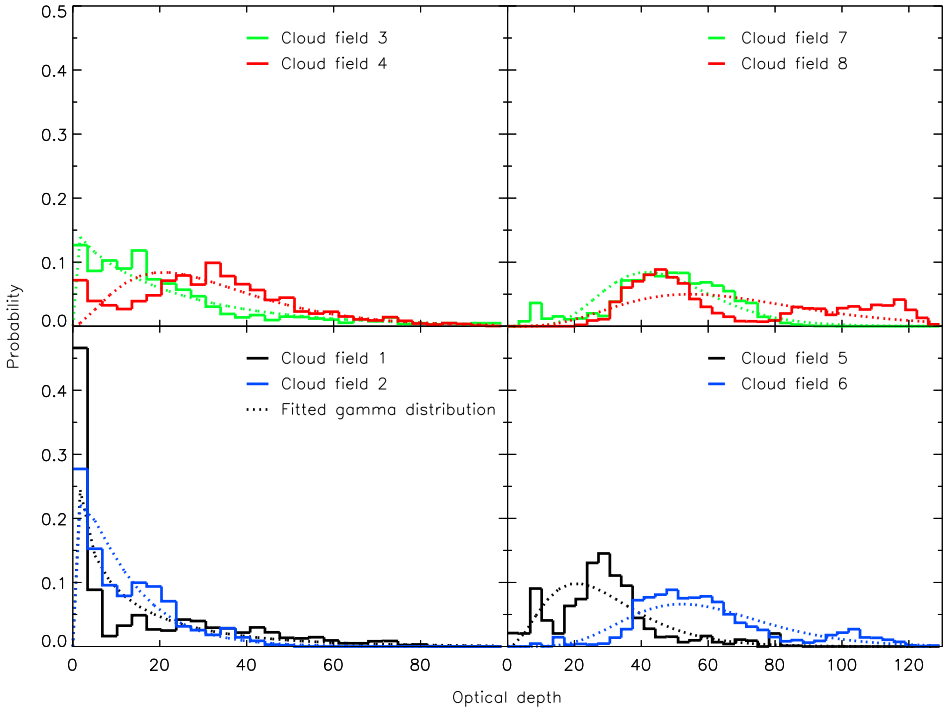

Figure 3.11: Probability distribution functions of the cloud optical depth for the surrogate cloud fields and respective approximations

Table 3.4: Cloud optical depth statistics

Field	Mean all col.	Mean cloudy col.	Std. dev. cloudy col.	β	χ
1	10.1	15.3	19.3	-1.98	0.13
2	7.6	11.8	10.7	-1.23	0.29
3	12.8	24.1	24.7	-1.23	0.61
4	29.5	32.1	19.1	-2.53	0.61
5	16.4	29.1	15.8	-2.86	0.82
6	59.1	59.9	21.6	-2.73	0.93
7	47.8	47.8	16.9	-1.86	0.90
8	67.5	67.5	29.5	-3.24	0.90

adequately represented. Several statistics of optical depth are displayed in Table 3.4. Though cloud fields do not have an equidistant grid, the mean slope of the power spectrum β was calculated by the Fourier transform. In doing so it was assumed that the error induced by not applying the Lomb periodogram (Press et al., 1992) will be smaller then the effect of averaging Fourier coefficients from several transects of the fields. In addition to the slope of the power spectrum the parameter χ describes the inhomogeneity of the optical depth field but without taking into account the spatial distribution (Cahalan et al., 1994b). It is calculated as the ratio of logarithmic and linear average of the distribution of optical depth within the field as

$$\chi = \frac{e^{\overline{ln\delta}}}{\overline{\delta}}, \quad 0 < \chi \leq 1 \tag{3.11}$$

$$\overline{\delta} = \int \delta P(\delta) d(\delta) \tag{3.12}$$

$$\overline{ln\delta} = \int ln\delta(\delta) d\delta \tag{3.13}$$

where δ is the optical depth and $P(\delta)$ is the probability of occurrence of δ within the field. Table 3.4 reveals that there exists no relation between the variability of optical depth and the spatial scales of the variability. Due to Parseval's theorem the power spectrum integral in the frequency or wavenumber domain represents the variance of the time or spatial series. If an increased ratio of the overall variance would be explained by higher wavenumbers, the slope of the power spectrum would decrease. This relation is not found for the surrogate cloud fields indicating that the spatial representation of the variability differs between the surrogate cloud fields.

Remote sensing of cloud optical depth by reflected solar radiation suffers from saturation problems. Retrieval accuracy decreases below optical depths of 1 and above 70 (Dim et al. 2007). Analyzing the surrogate cloud fields for affected columns, 0 - 32% and 1.8 - 38% of the cloudy area have optical depth below and above these values, respectively.

Besides the presentation of potential constraints applicable in cloud field reconstruction derived from observations cited in literature, this chapter shows that some features of the surrogate cloud fields are in good agreement with measurements of various instruments. The most crucial deviation

is caused by low values of effective radius and might be responsible for deviations of extinction coefficient and optical depth, too.

Chapter 4

Reconstruction of cloud fields

4.1 Introduction

This chapter presents three approaches for the reconstruction of cloud fields from datasets as shown in Figure 1.1. These datasets were compiled from the surrogate cloud fields. The reconstruction approaches differ in applying profile information or relying solely on cloud properties that can be derived from satellite radiometer data. Following the description of the reconstruction algorithms, their performance is evaluated by analyzing the differences in macro- and microphysical properties between the reconstructed cloud fields and the respective surrogate cloud fields.

4.2 Reconstruction without information of profiling instruments

The approach presented in this section and denoted as the 'adiabatic profile reconstruction' (AP) makes use of information about the cloud fields available from passive radiometers onboard current satellites. Cloud-top height, cloud optical thickness, and effective radius are products derived for example from NOAA-AVHRR or MODIS data. The only free parameter in this model is the cloud-base, which is approximated in this way that a single-layer cloud with an adiabatic LWC profile and a homogeneous effective radius profile accounts for the satellite-derived optical depth of the column.

The effective radius located in the distance 2 optical depths below cloud-top was assigned to the overall cloud column. The LWC profile between cloud-base and cloud-top was assumed to be adiabatic (Fig. 4.1) with a well mixed subcloud layer (Miller et al., 1998). Temperature and pressure of the base layer were taken from radiosoundings but might also be adopted from surface measurements or model data. Applying a standard gamma drop size distribution, cloud extinction was calculated by Mie routines. An iterative procedure adjusted the cloud-base height for the individual column so that

$$\sum_{z=0}^{\infty} \beta_{ext}(LWC(z), r_e(z))dz = \sum_{z=0}^{\infty} \beta_{ext}(LWC_{ad}(z), r_e(\delta = 2))dz \tag{4.1}$$

with extinction coefficient $\beta_{ext}(LWC(z), r_e(z))$ deduced from liquid water content $LWC(z)$ and effective radius $r_e(z)$ in height z of the surrogate cloud field. The extinction coefficient β_{ext} $(LWC_{ad}(z), r_e(\delta = 2))$ for the respective adiabatic cloud column is a function of the adiabatic

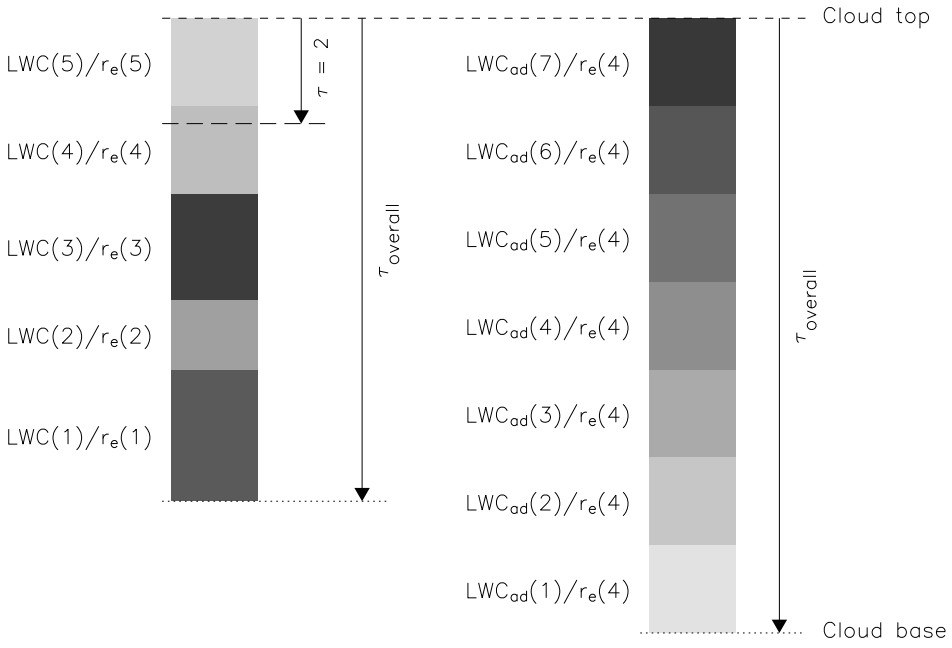

Figure 4.1: Schematic depiction of the reconstruction of cloudy columns by assuming a vertical non-varying effective radius and an adiabatic liquid water content profile.

liquid water content $LWC_{ad}(z)$ and the height-invariant effective radius $r_e(\delta = 2)$ and its integration yields the predefined optical depth. The assumption of an adiabatic LWC profile is most likely for stratiform clouds without entrainment. However, effective radius profiles similar to the reconstructed ones are not in line with the adiabatic model (Brenguier et al., 2000) but have been found in continental cumulus clouds (Bower et al., 1994). The same configuration of LWC and effective radius profiles was used in previous studies (e.g. Wen et al., 2008), too.

Though the cloud-base was approximated fairly exact, small differences between predefined and reconstructed cloud optical depth may arise due to vertical discretization effects. Pincus et al. (1995) analyzed the uncertainties of cloud optical depth retrievals from satellite due to sensor discretization, calibration, and atmospheric model uncertainties and found uncertainties of at least 5%. Comparing reconstruction inaccuracy and retrieval uncertainty, 3 cloud fields exhibit areas of up to 6% of the cloudy area where the absolute difference in cloud optical depth between reconstructed and surrogate cloud field exceeds the retrieval uncertainty of 5% of the surrogate cloud optical depth. The greatest values of absolute optical depth difference with a maximum of 0.52 appear in columns with small optical depth. Clouds in these columns are geometrically thin but the effective radius is very low and thus the extinction coefficient is large even for low liquid water contents. Consequently, the vertical resolution leads especially in these columns to deviations from the predefined optical depth.

4.3 Reconstruction with information of the mean profile

This section delineates an approach in which cloud fields are reconstructed by means of information from the cross-section. The reconstruction starts with the simulation of cloud geometrical thickness and cloud-base followed by the adjustment of the microphysical profiles.

Analyzing the profiles, robust correlations between cloud optical depth and cloud geometrical thickness were found for 4 cloud fields. In order to find a cloud-base reconstruction scheme applicable to all cloud fields, an approach was chosen that does not rely on this correlation. The cloud thickness field was estimated from the spatial correlation and the probability distribution function of cloud geometrical thickness derived from the cross-section (Fig. 4.2).

In the first step, cloud geometrical thickness was calculated for the columns of the slice as the sum of the thicknesses of cloudy levels. For this series the probability distribution was derived. Furthermore, the power spectrum was calculated assuming an overcast cloud field. Instead of filling cloud-free columns and using the Fourier analysis for equidistant data points, the Lomb-Scargle algorithm for unevenly sampled data (Press et al., 1992) was applied. The slope of the derived spectral coefficients and the PDF yielded the constraints for the IAAFT algorithm, which determined the 2d field of geometrical cloud thickness. Combining the fields of cloud-top and cloud thickness results in the cloud-base for columns indicated as cloudy by the cloud-top field. Because cloud thickness was discarded in cloud-free columns, the slope of the 1d power spectrum as well as the PDF differ between the transect and the 2d field. It also has to be noted that cloud-base reconstruction in this way does not maintain the cloud-base of the cross-section.

The microphysical profiles for every column were determined by profile information, too. To this end mean profiles of LWC and effective radius were adjusted by shifting within predefined boundaries to yield the predefined cloud optical depth of the columns (Fig. 4.3). In the following the algorithm will be described in more detail.

From the cross-section mean values of LWC and effective radius were calculated for every cloud level. Minimum and maximum values of these parameters determined the range for the respective level whereas microphysical parameters are not limited to this range when no solution could be found. Additionally, the mean relative height $\overline{h}_{rel}(\delta = 2)$ between cloud-base and cloud-top for the level where the retrieval of the effective radius originates from was calculated from the profiles. Constraints for the microphysics profile reconstruction were completed by several threshold values. The threshold value for the effective radius minimum results from the discretization of the cloud drop size distribution. Reduction of the effective radius in the iterative adjustment process aims to increase cloud extinction. When the effective radius becomes lower than the minimum threshold, most bins of the drop size distribution have low size parameters with extinction efficiencies significantly lower than 2. Consequently, a further reduction of effective radius results in decreasing extinction. The maximum threshold of effective radius results from the maximum of effective radius found in the set of surrogate cloud fields and is therefore not deduced from the individual transects. Assuming that maximum values of the transect are also representative for the extreme values of the entire cloud field, this threshold could be determined as a bulk threshold or even as a height-dependent threshold from the cross-section. The minimum threshold of the liquid water content is caused by numerical requirements.

Besides this definition of the thresholds, there are other thresholds conceivable determined by the thresholds of microphysics devices or by microphysical assumptions. In the present study it was assumed that clouds are non-drizzling water clouds. Due to this assumption the maximum threshold for effective radius would be about 14 μm. Drop size distributions with higher effective radius are characterized by coalescence and subsequent drizzle formation. However, further reduction of the range defined by this thresholds may prevent the algorithm from finding a solution.

The adjustment of the microphysical profiles was done by shifting the mean profiles of LWC and effective radius in opposite directions. The procedure is split in two parts, adjusting first the upper and then the lower part of the profile. The upper part is bounded by the cloud-top and the

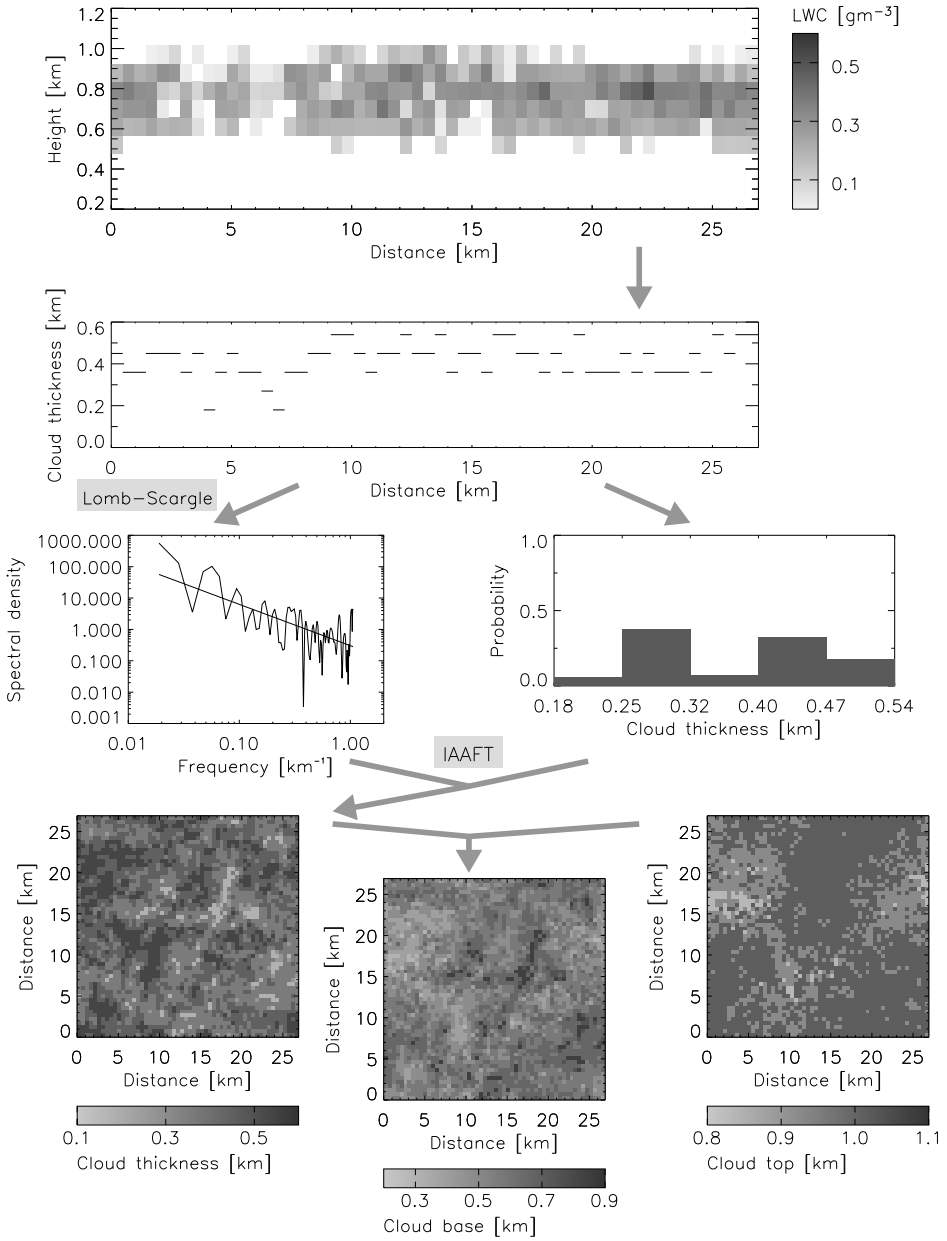

Figure 4.2: Cloud-base approximation for cloud field 7. Input data for the IAAFT are calculated from the cloud geometrical thicknesses of the slice. The result of the IAAFT is a 2D field of cloud geometrical thickness which is used to derive the cloud-base height for the cloudy columns.

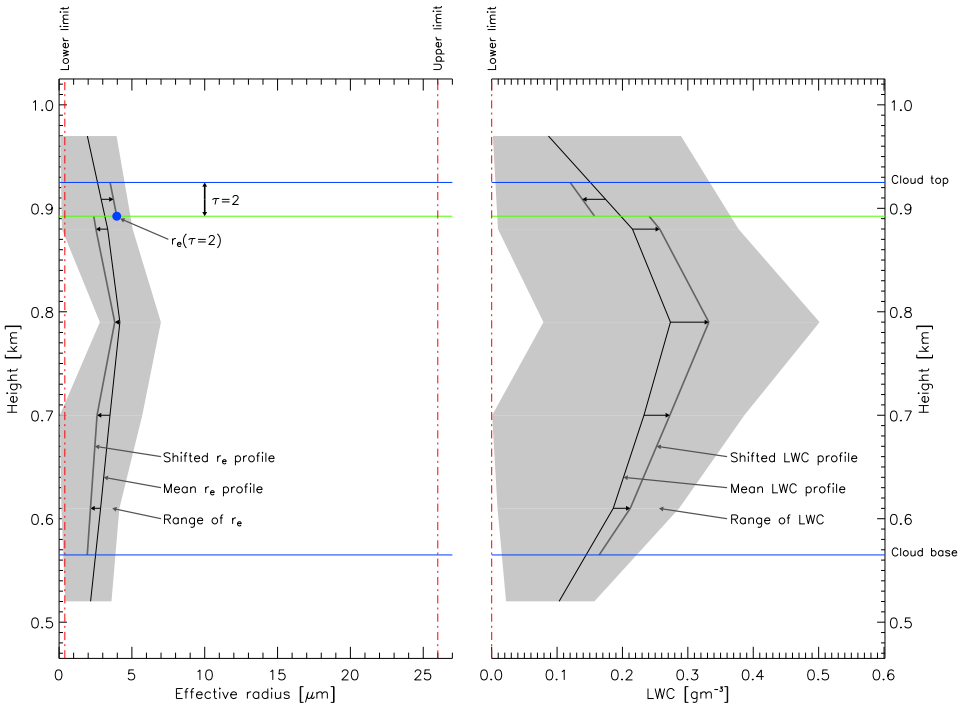

Figure 4.3: Adjustment of the profiles of LWC and effective radius. This is done in a two-step procedure starting with the adjustment of the upper part of the profile to preserve the effective radius in the predefined height and the following adjustment of the rest of the profile.

height where the effective radius, known for all columns, originates from. Consequently, its optical thickness is 2. The geometrical thickness dz was calculated as

$$dz = \overline{h}_{rel}(\delta = 2)(ct - cb) \tag{4.2}$$

where ct is the cloud-top and cb is the cloud-base. The absolute height $h_{abs}(\delta = 2)$ was computed as

$$h_{abs}(\delta = 2) = ct - dz. \tag{4.3}$$

The mean effective radius profile was shifted so that the predefined effective radius and the value of the shifted profile coincide in the height $h_{abs}(\delta = 2)$. The ranges of LWC and effective radius values of every level deduced from the cross-section were considered to be representative for the variability of the entire layer. Consequently, the offset $dr_e(z)$ and the effective radius value $r_e(z)$ for every layer z were calculated as

$$r_e(z) = \overline{r_e}(z) + dr_e(z) \text{ with } dr_e(z) = \begin{cases} q_{r_e}(r_{e,max}(z) - \overline{r_e}(z)), \text{ if } q_{r_e} \geq 0 \\ q_{r_e}(\overline{r_e}(z) - r_{e,min}(z)), \text{ if } q_{r_e} < 0 \end{cases} \tag{4.4}$$

where $\overline{r_e}(z)$, $r_{e,min}(z)$ and $r_{e,max}(z)$ are mean value, minimum, and maximum of the effective radius deduced from the cross-section, respectively. The parameter q_{r_e} is a scaling coefficient, which may differ between the upper part and the lower part of the reconstruction, but is, except

for a special case mentioned later, height-independent within in each part. When the effective radius profile of the upper part has been determined and described by the scaling coefficient, the LWC profile had to be adjusted so that the optical depth of this part became 2. This was done by an iterative procedure based on the same principles as the effective radius adjustment routine. The offset $dLWC(z)$ and the liquid water content, denoted by $LWC(z)$ for the height z, were computed as

$$\begin{aligned} LWC(z) &= \overline{LWC}(z) + dLWC(z) \\ \text{with } dLWC(z) &= \begin{cases} q_{LWC}(LWC_{max}(z) - \overline{LWC}(z)), \text{ if } q_{LWC} \geq 0 \\ q_{LWC}(\overline{LWC}(z) - LWC_{min}(z)), \text{ if } q_{LWC} < 0 \end{cases} \end{aligned} \tag{4.5}$$

where $\overline{LWC}(z)$, $LWC_{min}(z)$, and $LWC_{max}(z)$ are mean value, minimum, and maximum of LWC found in the cross-section, respectively. It has to be mentioned that the absolute values of q_{LWC} and q_{r_e} may exceed 1. They were bounded in this way that LWC or effective radius in any level never exceed the maximum threshold or fall below the minimum threshold. If the iteration procedure reached the scaling coefficient where the microphysical value in a certain height corresponded to one of the thresholds, the value was fixed and the layer was excluded from further iterations of this parameter. This is the special case where the scaling parameter is not uniform within the part of the cloud column.

The reconstruction of the lower part bases upon the same principles but differs in some details. The constraints for this part are the height $h_{abs}(\delta = 2)$, the cloud-base height, and the rest of the optical depth, namely the columns optical depth minus 2. Profiles were adjusted according to Eqs. 4.4 and 4.5. The difference to the approach for the upper part is that q_{LWC} and q_{r_e} differ in sign but not in magnitude. Shifting in opposite directions yields a straightforward progression in the iteration procedure. The same magnitude results in a unique solution. The iterative procedures of the upper and the lower part of the profile relies on computations of extinction profiles realized by Mie calculations.

Several situations appeared applying the presented reconstruction method. If the overall cloud optical depth was below 2, the effective radius signal was assumed to originate from the cloud-base level. Consequently, the adjustment of the lower part was skipped. It also happened that the iterative procedure did not found a solution for the lower part of the profile. If the derived maximum optical depth was lower than the preset optical depth, the cloud-base height was lowered by a fixed value and the adjustment procedure restarted. If the new cloud-base was lower than the the lowest cloud-base of the slice and therefore no LWC and effective radius were available, both values were adopted from the lowest available level. Stepwise lowering of the cloud-base was done until a solution was found. If on the other hand the derived minimum optical depth was too high, the cloud-base was lifted. It has to be noted that modifying the cloud-base in this way changes the power spectrum of cloud geometrical thickness.

Like the cloud-base reconstruction approach, the profile reconstruction method is not an exact method in geostatistical sense, because profiles at the sampling points, here the cross-section, are not retained. Absolute differences in surrogate and reconstructed cloud optical depth are lower than for the adiabatic reconstructions with a maximum of 0.22. Examining the area where reconstruction accuracy is lower than remote sensing accuracy, only 1 field exhibits around 4 % of its cloudy area. The method presented in this section is denoted as 'Scheme 1' in subsequent chapters.

4.4 Reconstruction with profile information of the complete transect

This reconstruction method, denoted as 'Scheme 2', is quite similar to the previous one. The difference is that instead of the mean profile individual profiles of the slice were adopted as a priori profiles and adjusted to receive the optical depth of the column. The initial fields of cloud-base height were the same as used by the method presented in the previous section so that comparisons of cloud fields reconstructed by the methods reveal differences in the profile reconstruction part.

The initial profile for the scaling step was found by the minimum absolute difference in cloud optical depth between the considered column and the cloudy columns of the slice. Other approaches are conceivable, for example the minimization of a cost function including besides optical depth additional parameters like cloud-top height and effective radius. The relative height dz in the cloud, where the remotely-sensed effective radius is located, was determined from the selected profile. Furthermore, height-dependent extreme values were employed to determine the scaling coefficients and thus Eqs. 4.4 and 4.5 change to

$$r_e(z) = r_{e,i}(z) + dr_e(z) \text{ with } dr_e(z) = \begin{cases} q_{r_e}(r_{e,max}(z) - r_{e,i}(z)), \text{ if } q_{r_e} \geq 0 \\ q_{r_e}(r_{e,i}(z) - r_{e,min}(z)), \text{ if } q_{r_e} < 0 \end{cases} \tag{4.6}$$

and

$$\begin{aligned} &LWC(z) = LWC_i(z) + dLWC(z) \\ &\text{with } dLWC(z) = \begin{cases} q_{LWC}(LWC_{max}(z) - LWC_i(z)), \text{ if } q_{LWC} \geq 0 \\ q_{LWC}(LWC_i(z) - LWC_{min}(z)), \text{ if } q_{LWC} < 0 \end{cases} \end{aligned} \tag{4.7}$$

respectively, with i the index of the chosen column of the slice. Because of applying the IAAFT-simulated cloud geometrical thickness, even reconstructions of the single-layer cloud profiles of the slice might not retain the original microphysical properties.

The maximum absolute difference in optical depth between reconstructed and original cloud fields is 0.21. In one cloud field in about 4 % of the cloudy area reconstruction inaccuracy of optical depth exceeds the inaccuracy due to remote sensing. Thus, reconstruction accuracy compares to the reconstruction accuracy of the mean profile approach.

4.5 Quality of the reconstructed cloud fields

In this section the quality of the reconstructed cloud fields will be assessed by comparing macro- and microphysical cloud properties of surrogate and reconstructed cloud fields. Results will reveal the capabilities of each reconstruction scheme.

Because cloud-top height and cloud optical depth were constraints of the algorithms, differences between cloud fields are described by the deviations of profiles of volume extinction coefficient, liquid water content, and effective radius as well as differences in cloud geometrical thickness and liquid water path.

Table 4.1 lists root-mean-squared errors (RMSE) and mean differences in geometrical thickness, calculated from the reconstructed and the original cloud fields. Here, cloud geometrical thickness is the distance between the highest cloud-top and the lowest cloud-base of the column and does not take into account that multi-layered cloud columns appear in the surrogate cloud fields.

Table 4.1: Differences in cloud geometrical thickness [km]

Field	RMSE AP (Mean difference)	RMSE Scheme 1/2 (Mean difference)
1	0.205 (0.100)	0.142 (-0.057)
2	0.181 (-0.079)	0.277 (0.075)
3	0.129 (-0.054)	0.240 (-0.026)
4	0.121 (0.048)	0.114 (0.010)
5	0.120 (0.036)	0.108 (-0.015)
6	0.173 (0.139)	0.056 (0.003)
7	0.163 (-0.123)	0.125 (-0.021)
8	0.165 (-0.132)	0.080 (-0.017)

Except for cloud fields 2 and 3 information from the slice improves the cloud-base reconstruction. Both cloud fields also exhibit the greatest deviations for Scheme 1 and 2, which results from the higher variability of cloud thickness in the slice of the original cloud fields (see Table. 3.1 for statistics of cloud geometrical properties of the entire cloud fields). Even if the statistics of the cloud thickness from the slice are representative for the entire cloud field and the spatial characteristics of cloud thickness are simulated properly, slight horizontal displacements of reconstructed fields will result in great deviations when thickness is highly variable. Examining Table 3.1 suggests the influence of the multi-layered cloud columns on the reconstruction quality of Scheme 1 and 2, but it has to be kept in mind that cloud thickness calculations for the reconstruction method and the quality assessment differ. However, adiabatic profile reconstruction quality shows no influence of multi-layered cloud columns.

For comparison liquid water content and effective radius of surrogate and reconstructed cloud fields were resampled on a consistent grid with high resolution for cloudy levels. The interpolation for resampling was done applying Eqs. 2.2 and 2.8. The extinction coefficient was not resampled but was recalculated from resampled LWC and effective radius to account for the nonlinear relationship of microphysical and optical properties.

The reconstruction quality of cloudy columns is expressed by the RMSEs of LWC, effective radius, and extinction coefficient for cloudy cells. Deficient algorithms would support right-shifted PDFs of RMSE compared to the PDFs of superior algorithms, as it is illustrated for cloud field 7 in Figure 4.4.

Visual inspection of the PDFs reveals only for the cloud fields 6, 7, and 8 patterns indicating better overall reconstruction results of the algorithms taking the profile information into account. The RMSEs of LWC, effective radius, and extinction coefficient were correlated with the absolute cloud thickness differences. Therefore, the Pearson correlation coefficient was calculated for the single-layer cloud columns. With most of the correlation coefficients smaller than 0.6, there is no evidence that the RMSEs depend on the quality of the cloud thickness reconstruction. When comparing the RMSEs of the multi-layered cloud columns with those for the single-layered ones, for most of the cloud fields and parameters the mean value for the single-layered ones lies below those for the multi-layered ones, indicating that reconstruction is less adequate for multi-layer cloud columns. In addition to the three-dimensional cloud parameters analyzed above, there are also differences in the liquid water path of the cloudy columns. The RMSE of LWP for the reconstruction schemes is displayed in Table 4.2.

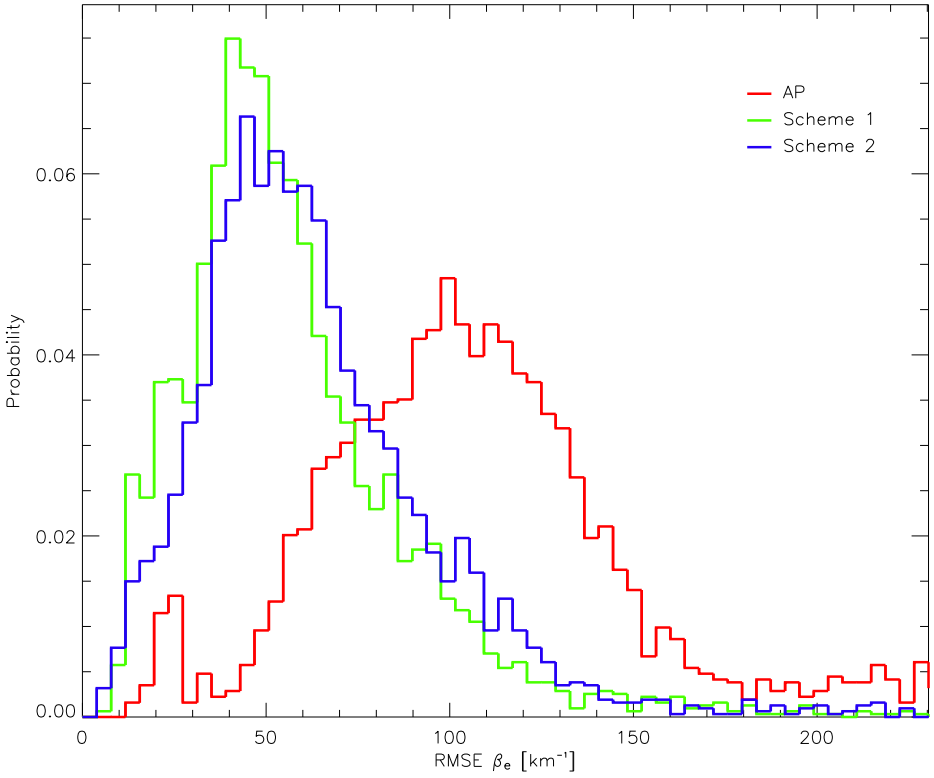

Figure 4.4: Probability distribution functions of the RMSE of volume extinction coefficient of cloud field 7. The RMSE was calculated for every cloud column from the extinction of the original cloud field and the reconstructions.

Table 4.2: Differences in cloud liquid water path [gm^{-2}]

Field	RMSE AP	RMSE Scheme 1	RMSE Scheme 2
1	35.12	39.57	30.63
2	14.73	12.70	15.07
3	35.42	50.12	51.46
4	22.51	23.80	30.35
5	21.05	34.98	30.35
6	23.70	29.50	21.69
7	36.40	25.72	19.67
8	50.53	39.50	23.78

Table 4.3 summarizes the reconstruction quality for the parameters mentioned before by flagging the cloud fields, where Schemes 1 and 2 perform better than the adiabatic profile method. The table reveals that employing additional information from the profiles does not necessarily result in improved reconstructions. At least the reconstructions of the overcast cloud fields 7 and 8 benefit from the profile information.

When the deviations are mapped like in Figure 4.5, it is possible to indentify regions where cloud properties match better than in the surrounding areas. In a subsequent part of this study microphysical properties are related to radiative transfer results. It is expected that radiation and consequently radiation differences between original and reconstructed cloud fields for a column do not only depend on microphysical differences in the column but due to horizontal photon transport also on differences in adjacent columns. This expectation was addressed by introducing a concept called 'well reconstructed area' (WRA). The concept identifies areas characterized by an advanced reconstruction quality. These areas will be analyzed separately in further investigations. The concept of well reconstructed areas is defined for all gridcell properties like LWC, effective radius, and extinction coefficient. There are four conditions columns have to meet to be assigned to these areas. First of all the reconstructed and the surrogate column have to be cloudy. Examining vertical columns, as it has been done so far, either both columns are cloudy or both columns are cloud-free. When in a subsequent part of this study differences of tilted columns are analyzed, it may happen that due to inadequate cloud-base reconstruction in columns near cloud edges only the original or the reconstructed column is cloudy.

The second condition claims that the RMSE of the column is lower than the mean RMSE derived for the field. Because the mean RMSE may differ between the individual realizations, the concept of well reconstructed areas is not a global concept but is appropriate for refined investigations for individual cloud fields. The third condition refers to the bias of reconstructed profiles, which is calculated as

$$bias = \frac{1}{n} \sum_{i=1}^{n} d_{rec}(i) - d_{orig}(i) \tag{4.8}$$

with the number of levels n that are at least in one of the profiles cloudy and the vertical index i. The value d may be the LWC, the effective radius, or the extinction coefficient of the reconstructed profile *rec* and the original profile *orig*, respectively.

Table 4.3: Synopsis of microphysical and optical properties reconstruction quality

Field	RMSE thickness	PDF RMSE β_e	PDF RMSE LWC	PDF RMSE r_e	RMSE LWP
1	✔				
2					
3					
4	✔				
5	✔				
6	✔	✔	✔	✔	
7	✔	✔	✔	✔	✔
8	✔	✔	✔	✔	✔

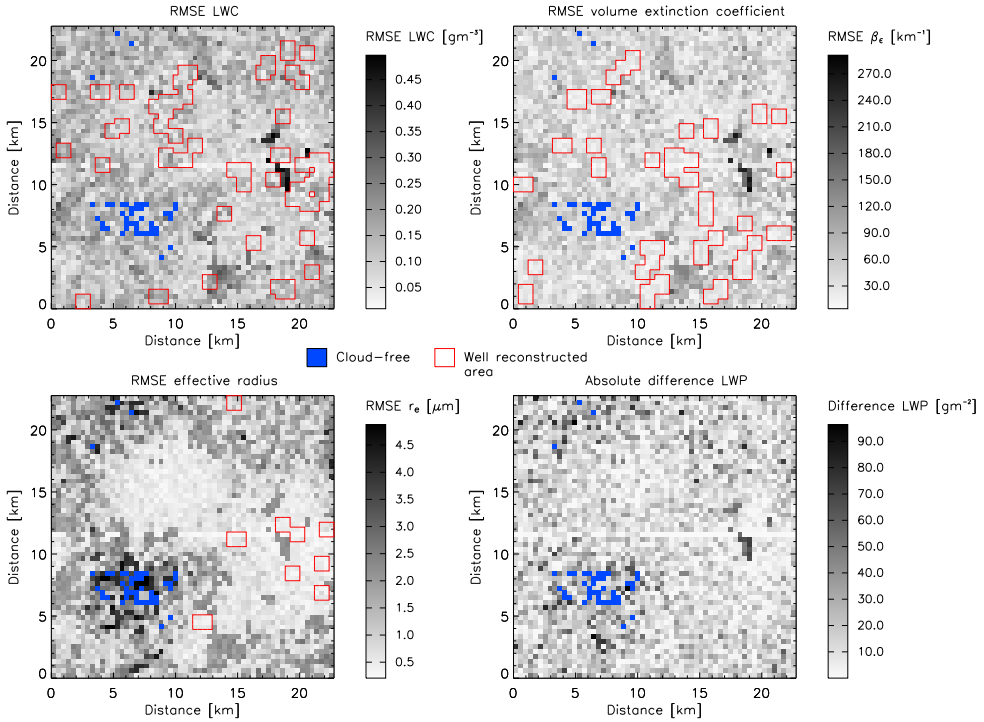

Figure 4.5: RMSE of cloud microphysics and optical properties and differences in LWP of cloudy columns for Scheme 2 reconstruction of cloud field 6.

Instead of determining profiles with a minor bias by comparing the bias of the profiles with the mean bias of the realization, the Mann-Whitney-Wilcoxon rank sum test (Wilks, 2006) was applied. This test determines whether two samples originate from the same distribution or in this case whether two profiles or histograms coincide (Sengupta et al., 2004). To exclude highly biased profiles from well reconstructed areas, solely these columns were subjected to further analysis where the null hypothesis stating that reconstructed and original profile originate from the same population was not rejected applying a 0.05 significance level. The final condition claims that a well reconstructed area is composed of at least 3 pixels in each direction whereas periodic boundaries were taken into account.

In Figure 4.5 the cross-section can be identified by exceptionally low RMSEs of LWC, extinction coefficient and effective radius as well as low absolute difference in LWP. They are a consequence of a low variability of cloud-base and choosing an appropriate a priori profile from the cross-section. Due to the low variability of cloud-base it is likely that cloud-base reconstruction is appropriate and the combination with a high probability that the a priori profile is the original profile of the considered column, this leads to an accurate reconstruction of the cloud profile.

Well reconstructed areas were mainly found for the RMSE fields of LWC and volume extinction coefficient of Scheme 1 and Scheme 2 reconstructions but less frequently for the RMSE fields of effective radius and for the fields simulated by the adiabatic approximation scheme. In two Scheme 2 reconstructions areas occur which meet the criteria of well reconstructed areas for LWC, effective radius and volume extinction coefficient in parallel. In the subsequent study well reconstructed areas will be used to investigate the question if an influence of the reconstruction quality of surrounding columns on the deviations of radiative properties of the corresponding column can be identified.

Chapter 5

Differences between the radiative transfer in original and reconstructed cloud fields

This chapter addresses the differences between radiative transfer in the original and the reconstructed cloud fields. It will provide insight if and to which extent differences in radiative properties reflect the quality of cloud field reconstruction.

To this end three-dimensional radiative transfer simulations with the Monte Carlo code were performed for the parameter combinations listed in Table 5.1. The wavelength was fixed at 0.6 μm. Solar zenith angles θ_0 were chosen as 0°, 30°, and 60° with a fixed azimuth angle ϕ_0 of 0°. Reflectances were simulated for 5 viewing directions, three with an azimuth angle ϕ of 0° and zenith angles θ of 0°, 30°, and 60°, respectively and two with an azimuth angle of 90° and zenith angles of 30° and 60°, respectively. In each simulation 10^7 primary photons were tracked. Due to the applied wavelength molecular absorption was neglected. The surface reflection was assumed to be lambertian. Its value of 0.0286 was computed from Eq. 2.25 for the BRDF of pasture land (Rahman et al., 1993). Rahman et al. (1993) note that model parameters describing the BRDF are not absolute and mainly intended to describe the anisotropy of the surface reflection. Consequently, one of the parameters can be scaled to derive a certain absolute reflectance function but this has not be done in this study and the model was used applying the original values. A quite similar albedo of 0.02 for the wavelength of 0.66 μm was used by Wen et al. (2008) to carry out radiative transfer simulations in the biomass burning region of Brazil. Besides Mie-scattering of cloud droplets Rayleigh-scattering was taken into account. In addition to reflectances photon properties, described in section 2.14 and depicted in Fig. 2.6, were derived.

The following section compares statistics of photon properties from simulations with the original and the reconstructed clouds fields. They will provide some insight into the footprints of radiation signals and their variations due to the different cloud field realizations. Várnai and Davies (1999) compared this kind of radiative transfer analysis to the Lagrangian approach in atmospheric modeling in contrast to the Eulerian approach where the radiation signal is investigated. This approach where differences between reflectances will be analyzed to answer the question if they reflect the reconstruction quality, will be the subject of Section 5.2.

Table 5.1: Parameters of radiative transfer simulations

Cloud fields	1, 2, 3, 4, 5, 6, 7, 8
Realizations	Original, AP, Scheme 1, Scheme 2
Illumination geometry (θ_0, ϕ_0)	(0°,0°), (0°,30°), (0°,60°)
Observation geometry (θ, ϕ)	(0°,0°), (0°,30°), (0°,60°), (90°,30°), (90°,60°)
Wavelength	0.6 μm
Albedo	0.028

5.1 Differences in photon statistics of the reconstructed cloud fields

Besides the random nature of photon pathes due to the Monte Carlo approach, photon properties also differ because of differences in geometrical and microphysical properties of cloud fields. Though photon properties are combined in a subsequent part of this study, it is not possible to recover individual photon pathes by means of the stored properties. However, combinations may be used to estimate the regions influencing the radiation signal.

An initial insight into differences in the radiative transfer between surrogate and reconstructed cloud fields may be obtained by comparing the patterns of the last position of the photons. The positions are defined by the horizontal coordinates where the photons either leave the cloud to enter the detector or where they are reflected on the ground and enter the detector without passing cloudy volumes in between (Fig. 2.6). Differences in these patterns may be caused by enhanced or reduced photon channeling, a process where photons are forced to propagate in regions with lower extinction and therefore are less frequently exposed to scattering events. Coley and Jonas (1996) found this effect most significant for low solar zenith angles and a more pronounced forward scattering due to larger droplets. Because optical depth of vertical orientated columns of the surrogate cloud fields is preserved by the reconstruction algorithms, differences in photon channeling for simulations with overhead sun can be caused solely by differences in microphysical profiles and cloud-base in regions favoured for photon channeling. A more pronounced photon channeling effect for one cloud field realization would result in a more clustered pattern of the final positions of the photons. For the detection of differences, Ripleys K parameters (Ripley, 1977) were calculated as

$$\hat{K}(t) = n^{-2} A \sum_{i} \sum_{j, j \neq i} w_{ij}^{-1} I_t(u_{ij}) \tag{5.1}$$

with Ripleys K value $\hat{K}(t)$ for the distance interval t, n the number of photon positions per unit area and A the region of interest. The parameter $\hat{K}(t)$ determines for every photon the number of photons I_t within the distance u_{ij} which is calculated as

$$u_{ij} = \sqrt{(x_i - x_j)^2 + (y_i - y_j)^2}. \tag{5.2}$$

The parameter w_{ij} in Eq. 5.1 is a weighting factor, accounting for cases where the area around the photon position defined by the distance K is truncated by the boundaries of the domain. This edge correction (Haase, 1995) assumes that the point pattern outside the domain is represented by the pattern inside the domain. Because the computation of Ripleys K for all photons of a simulation is unacceptable time-consuming, test areas with a side length of 1/4 of the domain side length were

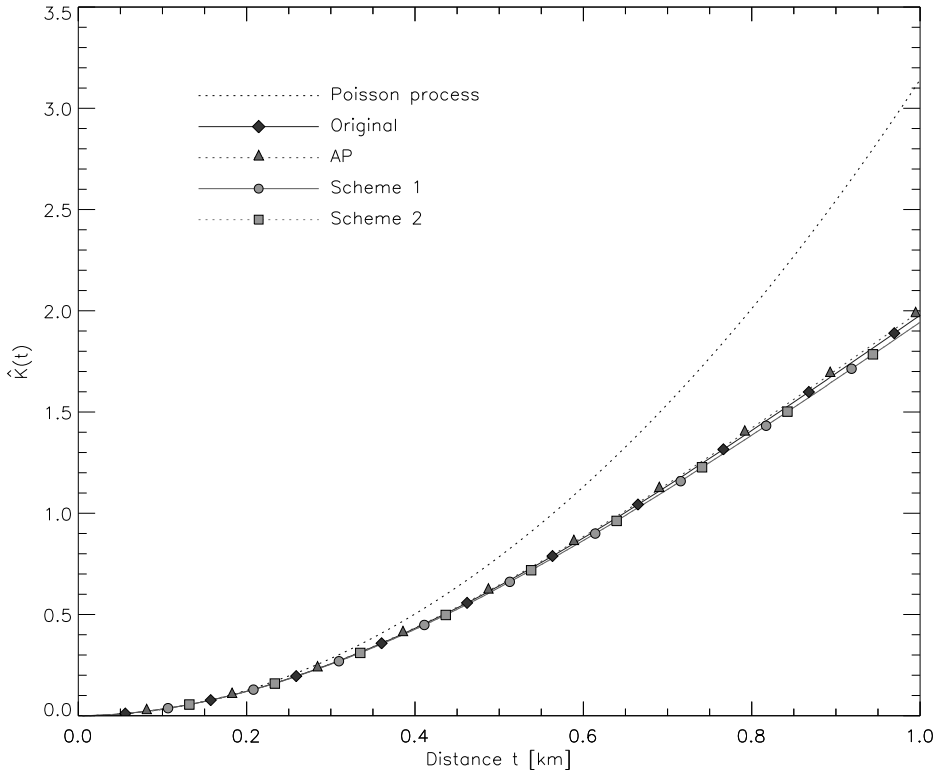

Figure 5.1: Ripleys K for the photon patterns of the realizations of cloud field 2 with $\theta_0 = 0°$.

defined for every cloud field. When Ripleys K is plotted against the diameter k, k^2 defines a point pattern process characterized by a Poisson distribution (Fig 5.1). Positive deviations from this line indicate enhanced clustering of photon positions, whereas a more regular distribution causes negative deviations. Visual inspection reveals that all realizations of the cloud fields exhibit a more homogeneous distribution than the Poisson process, independent of the solar zenith angle of the simulation. There are no significant or systematic differences between the different realizations, neither in magnitude nor in direction.

During the Monte Carlo simulations, the penetration depth, the lowest vertical position of the individual photon (Fig. 2.6), was recorded. It has to be emphasized that this parameter indicates a vertical coordinate and not a distance in the present study. This depth increases with wavelength due to increasing absorption (Kokhanovsky, 2004b), whereas local bands with enhanced absorption have to be taken into account. Penetration depth also increases with increasing solar zenith angle. Pronounced forward scattering expressed by an increased asymmetry parameter of the phase function enhances the vertical component of the photon vector and hence decreases the penetration depth. All the considerations refer to plane parallel clouds and relations may become complicated by cloud-top variability and horizontal inhomogeneities. Figure 5.2 presents the PDFs of the penetration depth for the simulations of the original and the reconstructed cloud fields. Additionally, the cloud masks for a randomly chosen slice are displayed to illustrate cloud geometrical properties. The maxima of the PDF reflect the distinct cloud-top levels within the cloud field. Also the height 2 optical depths below cloud-top exhibits a certain peak for the Scheme 1 reconstruction, because in most columns this height is characterized by discontinuities of microphysical and optical properties. Table 5.2 summarizes three measures for the comparison of

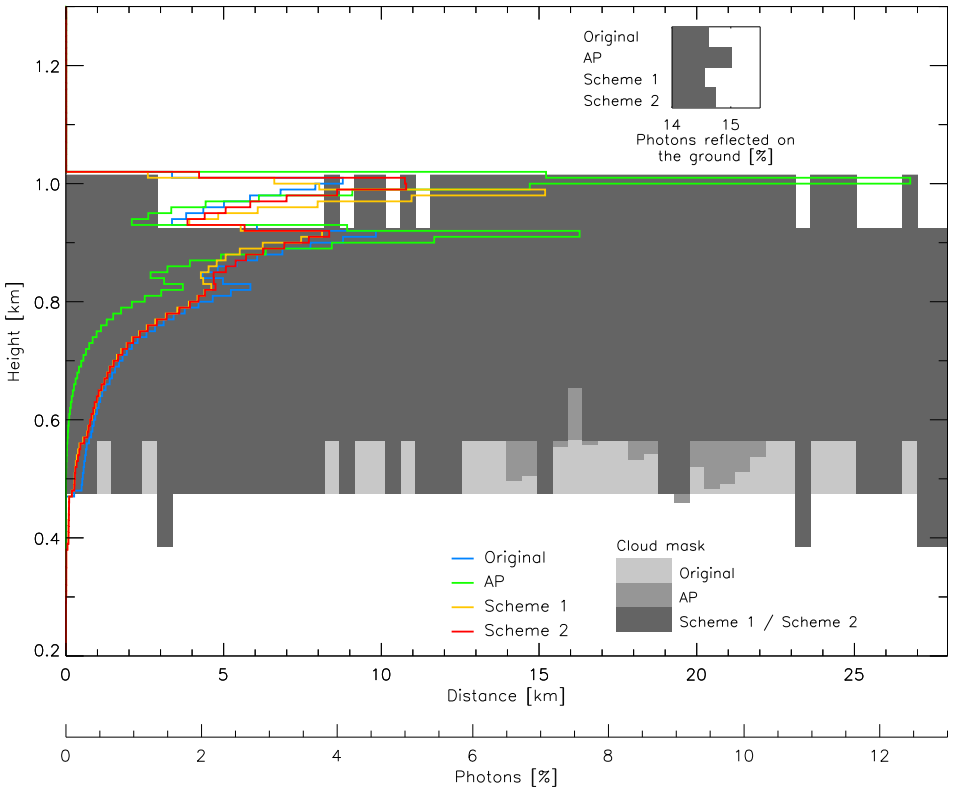

Figure 5.2: PDFs of photon penetration depth for the realizations of cloud field 8 ($\theta_0 = 30°$). Additionally, the cloud boundaries of a randomly chosen slice are plotted.

histograms (Xu, 2006) calculated for the penetration depth with bin sizes of 10 m. The Euclidian distance, also called L2 distance, corresponds to the RMSE and is calculated as

$$L2 = \left(\sum_{i=1}^{N} [f(x_i) - g(x_i)]^2 \right)^{0.5} \tag{5.3}$$

with $f(x_i)$ and $g(x_i)$ the frequencies of occurrence in bin x_i and N the number of bins of the histogram. The Jeffries-Matusita distance JM is defined as

$$JM = \left(\sum_{i=1}^{N} [\sqrt{f(x_i)} - \sqrt{g(x_i)}]^2 \right)^{0.5} . \tag{5.4}$$

In contrast to the L2 distance and the JM distance, the Kolmogorov-Smirnov distance KS does not integrate over all bins. It represents the maximum difference derived when the cumulative distribution functions are compared and is calculated as

$$KS = Max_i \left(\sum_{1}^{i} |f(x_i) - g(x_i)| \right) \quad \text{where } i = 1, 2, ..., N. \tag{5.5}$$

Xu (2006) introduced a bootstrap method to estimate the significance of histogram deviations. The PDFs of two realizations are combined and numerous pairs of PDFs are resampled from the

Table 5.2: L2, JM and KS for PDFs of global penetration depth

Field	θ_0	L2			JM			KS		
		AP	S1	S2	AP	S1	S2	AP	S1	S2
	0	0.014	0.036	0.036	0.141	0.201	0.203	0.023	0.061	0.068
1	30	0.016	0.041	0.042	0.148	0.202	0.206	0.025	0.059	0.068
	60	0.022	0.057	0.061	0.160	0.198	0.203	0.033	0.058	0.067
	0	0.019	0.013	0.012	0.137	0.091	0.095	0.038	0.015	0.011
2	30	0.020	0.015	0.013	0.150	0.102	0.106	0.037	0.018	0.014
	60	0.031	0.012	0.013	0.156	0.114	0.111	0.033	0.016	0.015
	0	0.032	0.019	0.015	0.137	0.089	0.066	0.051	0.016	0.018
3	30	0.034	0.019	0.015	0.139	0.090	0.064	0.051	0.019	0.015
	60	0.037	0.022	0.016	0.138	0.096	0.070	0.047	0.023	0.018
	0	0.039	0.031	0.021	0.136	0.135	0.099	0.069	0.038	0.035
4	30	0.041	0.032	0.021	0.136	0.138	0.098	0.068	0.038	0.032
	60	0.042	0.034	0.022	0.131	0.140	0.095	0.063	0.032	0.029
	0	0.041	0.026	0.018	0.150	0.121	0.079	0.068	0.039	0.031
5	30	0.044	0.027	0.018	0.147	0.121	0.076	0.068	0.038	0.029
	60	0.045	0.030	0.019	0.135	0.120	0.071	0.062	0.032	0.025
	0	0.054	0.009	0.007	0.160	0.032	0.043	0.092	0.016	0.013
6	30	0.056	0.009	0.007	0.154	0.032	0.042	0.089	0.015	0.012
	60	0.057	0.010	0.010	0.139	0.032	0.042	0.077	0.011	0.009
	0	0.131	0.046	0.047	0.394	0.137	0.141	0.257	0.074	0.101
7	30	0.135	0.048	0.048	0.383	0.138	0.135	0.250	0.072	0.098
	60	0.145	0.050	0.048	0.343	0.132	0.113	0.215	0.064	0.079
	0	0.116	0.053	0.025	0.359	0.156	0.102	0.230	0.085	0.055
8	30	0.118	0.053	0.024	0.350	0.151	0.097	0.223	0.080	0.053
	60	0.126	0.048	0.022	0.320	0.131	0.081	0.192	0.062	0.042

(θ_0: solar zenith angle, AP: adiabatic profile rec., S1: Scheme 1, S2: Scheme 2)

combined PDF. The distance measures are derived for these pairs and compared with the distance for the realizations. If more than 95% of the distances for the resampled histograms are lower than the distance of the realizations, the null hypothesis, that both histograms originate from the same population, is rejected at the 0.05 significance level.

Except for cloud field 1 and some JM distances of cloud field 4, all distance measures reveal more accurate PDFs for Scheme 1 and Scheme 2 than for the AP cloud fields. Analyzing the number of cases where the Scheme 2 distances are lower than Scheme 1 distances would recommend the Scheme 2 reconstruction method. On the other hand there are only two cloud fields (5 and 8) for which all distances decrease from AP via Scheme 1 to Scheme 2 for all solar zenith angles. Results of the bootstrap test demonstrate that all histograms differ at the 0.05 significance level.

When the penetration depth of the photon is localized by the position where the photon leaves the cloud towards the detector (Fig. 2.6), local PDFs can be calculated. Though this position may not coincide with the horizontal position where the penetration depth was reached, the statistics of the penetration depth may provide some insight in local radiative transfer differences and possibly in local cloud field reconstruction quality.

Spearman rank correlation coefficients of column RMSEs of microphysical as well as optical properties and RMSEs of penetration depth PDFs were calculated for all combinations of reconstructed and original cloud fields and solar zenith angles of the radiative transfer simulations listed in Table 5.1. Analyzed by a permutation test (Moore et al., 2003) about 40% of the 72 correlation coefficients do not significantly differ from 0.0. They never exceed 0.235 and no systematic differences are found for the coefficients derived for LWC, effective radius, and extinction coefficient.

The RMSEs of the microphysics well-reconstructed areas were checked against the remaining RMSEs, expecting that local penetration depth PDFs will be more similar for simulations with original and reconstructed cloud fields in WRAs than in the remaining areas. To explore this, the percentages of non-WRA columns where the RMSE exceeds the maximum RMSE of the WRA columns were computed. The maximum is about 25%, but most of the values are far lower. Additionally, a randomization test (Manly, 1996) was performed, testing for the null hypothesis that the mean RMSE of the WRA-classified columns is significantly lower than the mean of the remaining columns. The null hypothesis was rejected at the 0.05 significance level for 25% of the realizations with cloud fields containing WRAs.

Besides the penetration depth, also the pathlength of the photon in the clouds (Fig. 2.6) was stored during the simulations. The geometrical pathlength is defined in the present study as the overall distance covered by the photon inside cloudy volumes. Integration of the extinction coefficient along the photon path in the clouds yields the optical pathlength. In non-absorbing, horizontal homogeneous media geometrical pathlength depends on solar zenith angle, the extinction coefficient, and the asymmetry parameter of the phase function. When the solar zenith angle is large, photons do not enter the deeper layers of the cloud and less scattering events are necessary to redirect the photon in upward direction. Higher extinction coefficients reduce the geometrical pathlength by shortening the distances between the scattering events. An asymmetry parameter allowing enhanced scattering in sideway directions promotes the entering of the upward propagation direction after a reduced number of scattering events. These dependencies become blurred when media are horizontally heterogeneous like real-world clouds. Variabilities of cloud-top and base as well as variabilities of optical properties cause effects, described by Várnai and Davies (1999) as trapping, where the geometrical pathlength increases compared to the homogeneous case and escape, resulting in a reduced pathlength. Table 5.3 displays the difference measures for the global PDFs of geometrical pathlength in cloud.

Except for cloud field 1 and individual Jeffries-Matusita distances of cloud fields 3 and 4, pathlength distances exhibit characteristics similar to the distances of penetration depth with lower values for Schemes 1 and 2. In most cases distances for Scheme 2 are lower than for Scheme 1, favouring this reconstruction method. Bootstrap tests indicate for all simulations differences between PDFs for the original and the reconstructed cloud fields at the 0.05 significance level.

Like penetration depth also the geometrical pathlength in cloud has been localized and the RMSEs of the PDFs of original and reconstructed cloud fields were calculated. The permutation test reveals, that except for 6 cases, all Spearman rank correlation coefficients for the RMSE of geometrical pathlength and microphysical as well as optical properties differ significantly from zero. The largest coefficients are found for the correlation between the pathlength RMSE and

Table 5.3: L2, JM and KS for PDFs of global geometrical pathlength

Field	θ_0	L2			JM			KS		
		AP	S1	S2	AP	S1	S2	AP	S1	S2
	0	0.109	0.091	0.090	0.373	0.269	0.281	0.236	0.060	0.070
1	30	0.092	0.070	0.076	0.332	0.221	0.249	0.213	0.045	0.067
	60	0.063	0.025	0.034	0.265	0.109	0.143	0.183	0.018	0.061
	0	0.057	0.035	0.035	0.245	0.148	0.150	0.133	0.041	0.047
2	30	0.051	0.029	0.029	0.224	0.117	0.121	0.128	0.036	0.043
	60	0.039	0.014	0.016	0.187	0.072	0.083	0.118	0.027	0.038
	0	0.030	0.018	0.019	0.116	0.109	0.109	0.079	0.047	0.052
3	30	0.030	0.018	0.017	0.113	0.106	0.104	0.082	0.049	0.051
	60	0.032	0.020	0.019	0.111	0.115	0.110	0.084	0.074	0.071
	0	0.052	0.012	0.013	0.194	0.056	0.059	0.136	0.020	0.030
4	30	0.054	0.011	0.013	0.196	0.053	0.056	0.140	0.020	0.031
	60	0.064	0.014	0.011	0.195	0.057	0.051	0.147	0.024	0.028
	0	0.040	0.011	0.010	0.157	0.054	0.048	0.111	0.020	0.021
5	30	0.042	0.011	0.008	0.160	0.052	0.041	0.119	0.023	0.019
	60	0.049	0.014	0.007	0.163	0.062	0.037	0.121	0.039	0.025
	0	0.065	0.004	0.002	0.179	0.017	0.014	0.142	0.012	0.009
6	30	0.070	0.004	0.002	0.182	0.016	0.013	0.145	0.011	0.008
	60	0.091	0.004	0.002	0.187	0.015	0.011	0.152	0.009	0.006
	0	0.081	0.022	0.022	0.247	0.080	0.081	0.194	0.027	0.057
7	30	0.088	0.024	0.023	0.254	0.083	0.081	0.202	0.029	0.058
	60	0.113	0.030	0.027	0.266	0.093	0.077	0.214	0.048	0.052
	0	0.101	0.028	0.014	0.244	0.081	0.048	0.202	0.051	0.036
8	30	0.108	0.028	0.014	0.250	0.081	0.047	0.206	0.050	0.036
	60	0.132	0.029	0.013	0.257	0.079	0.043	0.211	0.041	0.034

(θ_0: solar zenith angle, AP: adiabatic profile rec., S1: Scheme 1, S2: Scheme 2)

the extinction coefficient RMSE with 25%- and 75%-quartiles of 0.37 and 0.57, respectively, and a maximum value of 0.88 (25%- and 75%-quartiles LWC: 0.18, 0.45, and r_e: 0.04, 0.37). There is no systematic pattern found for all cloud field realizations but for individual realizations most of the coefficients either increase or decrease monotonically with increasing solar zenith angle of the radiative transfer simulation.

Visual inspection of scatter plots reveals a typical pattern, illustrated in Figure 5.3. Data are arranged in two lobes with the one marked by the triangle composed of cloud edge columns with low optical depths. This pattern is most pronounced for simulations with the adiabatic profile reconstructions. Comparing the RMSEs of well-reconstructed areas for extinction coefficient, LWC, and effective radius with non-WRA areas, the maximum of non-WRA pixels with RMSEs greater than the maximum WRA RMSE is 57%. At least the randomization test yields for 38 of the 45 cases including WRA a significantly lower RMSE mean for the WRA pixels.

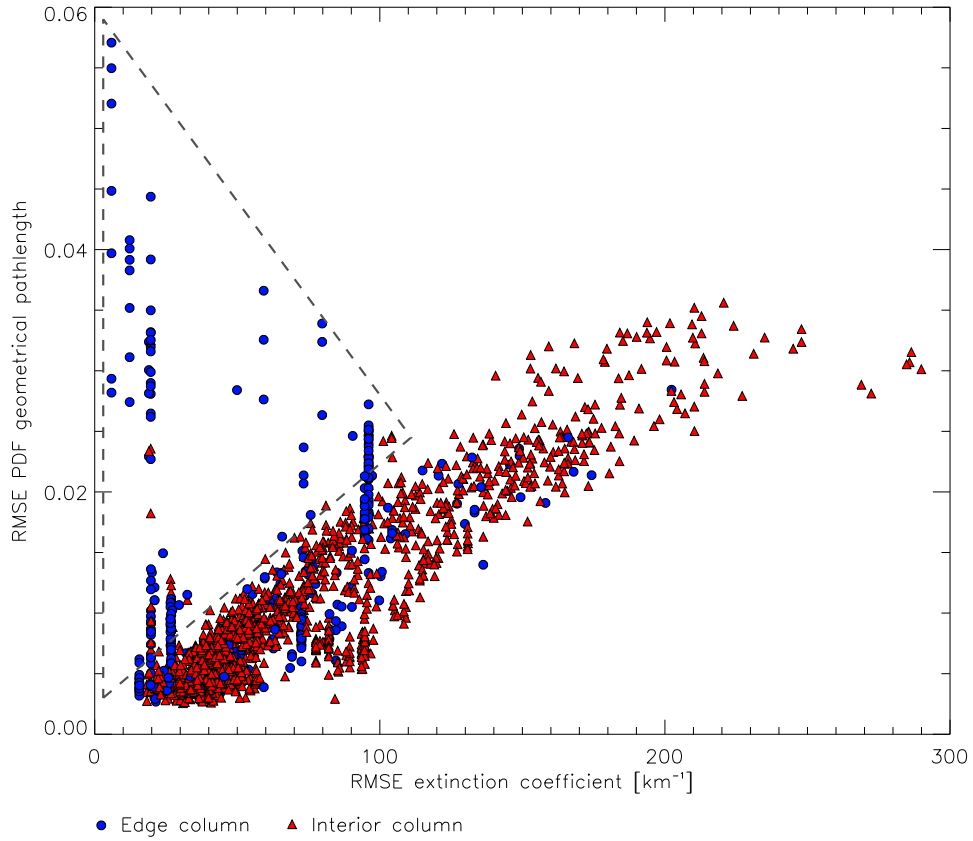

Figure 5.3: Scatterplot of the RMSE of extinction coefficient and the RMSE of the PDF of geometrical pathlength for cloudy columns of the AP reconstruction of cloud field 9 ($\theta_0 = 0°$). Columns at cloud edges are indicated. The triangle encloses columns at cloud edges with low optical depth.

The calculation of the mean geometrical pathlength of all photons that reached a certain depth defined by the penetration depth allows to estimate differences in the horizontal displacement of photons. An example contrasting the profiles derived by simulations with an original cloud field and derived by simulations with reconstructed cloud fields is shown in Fig. 5.4. It becomes obvious that for this case a certain depth exists, wherefrom statistics of the realizations diverge. Because original cloud-top height is preserved in all cloud field realizations, differences have to be attributed to differences in microphysical and optical properties. In simulations with adiabatic profile reconstructions photons entering the depth, wherefrom realizations diverge, have left behind the areas with the highest extinction and therefore the pathlength in lower penetration depth significantly increases. In the reconstructions of Scheme 1 and 2 extinction is distributed more homogeneously. The discontinuities in the mean geometrical pathlength profile are caused by distinct levels of cloud boundaries.

Analyzing the height-dependent mean geometrical pathlength for the overall cloud field by the RMSE shown in Table 5.4, it becomes evident that results of the simulations with reconstruction schemes comprising profile information are, except for cloud field 2, more accurate than results of the simulations with the adiabatic profile approximations. However, the results provide no indication for prefering Scheme 1 or Scheme 2.

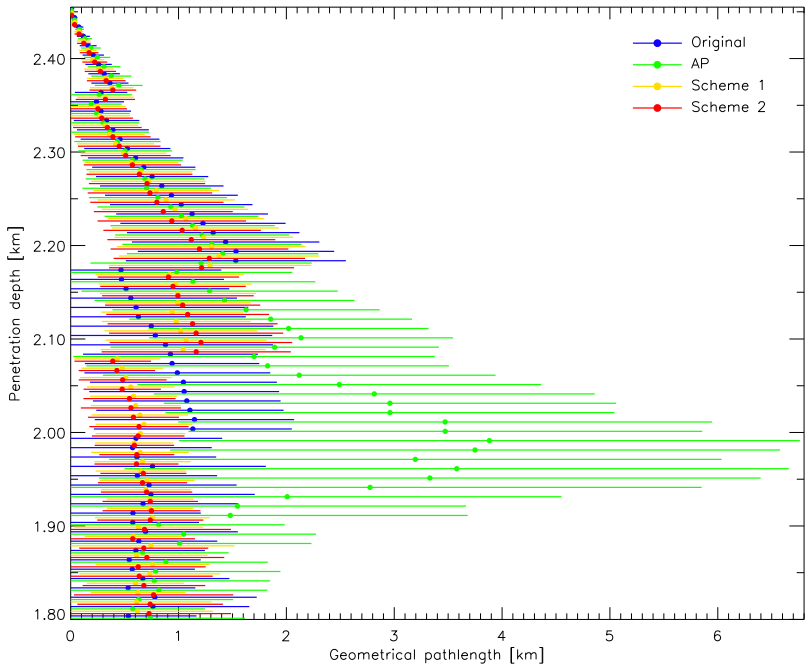

Figure 5.4: Profiles of mean and standard deviation of geometrical pathlength in the cloud, grouped by the penetration depth of the photons for cloud field 5 ($\theta_0 = 0°$)

Localized RMSE of the mean geometrical pathlength derived for the simulations with the original and the reconstructed cloud fields does not reflect differences in microphysical and optical properties. The 25%- and 75%-quartiles of the rank correlation coefficients are -0.08 and 0.302, respectively and coefficients never exceed 0.54. The maximum of non-WRA columns with higher RMSE than the RMSE maximum of WRA columns is about 23%. The randomization test yields on the 0.05 significance level only for 15 of 45 realizations a lower mean RMSE for WRA columns than for non-WRA columns of LWC, effective radius, and extinction coefficient.

Combining geometrical and optical pathlength provides insight into cloud field inhomogeneity (Stephens et al., 2005). Assuming a homogeneous cloud both are tightly correlated whereas inhomogeneity induces decorrelation. Figure 5.5 shows the PDFs of optical and geometrical pathlengthes scaled by mean cloud optical depth and mean cloudthickness, respectively, for cloud field 3 which is characterized by high variability of optical depth preferentially on the small scales (see Fig. 3.3). Figure 5.6, on the other hand, shows the PDFs for the more homogeneous cloud field 7, where the enhanced correlation becomes obvious.

The link between geometrical and optical pathlength was used to address the question if the relationships between microphysical as well as optical differences and deviations of photon path properties, derived in the previous part of this section, depend on the homogeneity of the volume passed by the photons. Therefore, the local correlation between geometrical and optical pathlength has been calculated and columns were sorted by the correlation in ascending order. The correlations of the RMSE of microphysical as well as optical properties and the RMSE of the photon properties were calculated for the columns exceeding a certain correlation coefficient between optical and geometrical pathlength. This approach is depicted in plots like Fig. 5.7. In the displayed realizations correlation coefficients between RMSE of LWC and RMSE of geometrical pathlength increase continuously. When analyzing these plots it has to be kept in mind that the number of

Table 5.4: RMSE of mean geometrical pathlength sorted by the penetration depth

Field	θ_0	AP	Scheme 1	Scheme 2
	0	0.455	0.077	0.077
1	30	0.405	0.072	0.073
	60	0.339	0.067	0.067
	0	0.065	0.280	0.285
2	30	0.060	0.275	0.274
	60	0.058	0.292	0.293
	0	0.110	0.098	0.093
3	30	0.102	0.085	0.083
	60	0.086	0.076	0.073
	0	0.212	0.130	0.123
4	30	0.215	0.132	0.130
	60	0.203	0.166	0.152
	0	0.302	0.076	0.082
5	30	0.288	0.071	0.079
	60	0.251	0.060	0.063
	0	1.032	0.357	0.354
6	30	1.029	0.344	0.357
	60	1.042	0.395	0.423
	0	0.290	0.157	0.184
7	30	0.310	0.173	0.191
	60	0.320	0.202	0.187
	0	0.458	0.266	0.249
8	30	0.488	0.257	0.260
	60	0.527	0.248	0.252

samples decreases towards higher values on the abscissa. Fluctuations appear where the number of data pairs is not sufficient for the calculation of reliable correlation coefficients. Patterns like in Fig. 5.7 are found solely for the correlation of the RMSEs of extinction coefficient as well as LWC and the RMSE of the geometrical pathlength PDF of individual realizations. Other realizations and also the correlations of the RMSE of penetration depth PDF as well as the RMSE of the profiles of mean geometrical pathlength sorted by the penetration depth with the deviations of the microphysical and optical properties either do not indicate an increase of coefficients, are characterized by low values around zero or coefficients fluctuate greatly within the entire series.

In Section 3.3 cloud field homogeneity was described by the parameter χ, derived for optical depth and not taking into account the spatial organization of the cloud field inhomogeneity as well as the slope β of the power spectrum of optical depth. In Fig. 5.8 both parameters are compared with the correlation of geometrical and optical pathlength. The plot provides no indication of a simple relationship between the individual parameters.

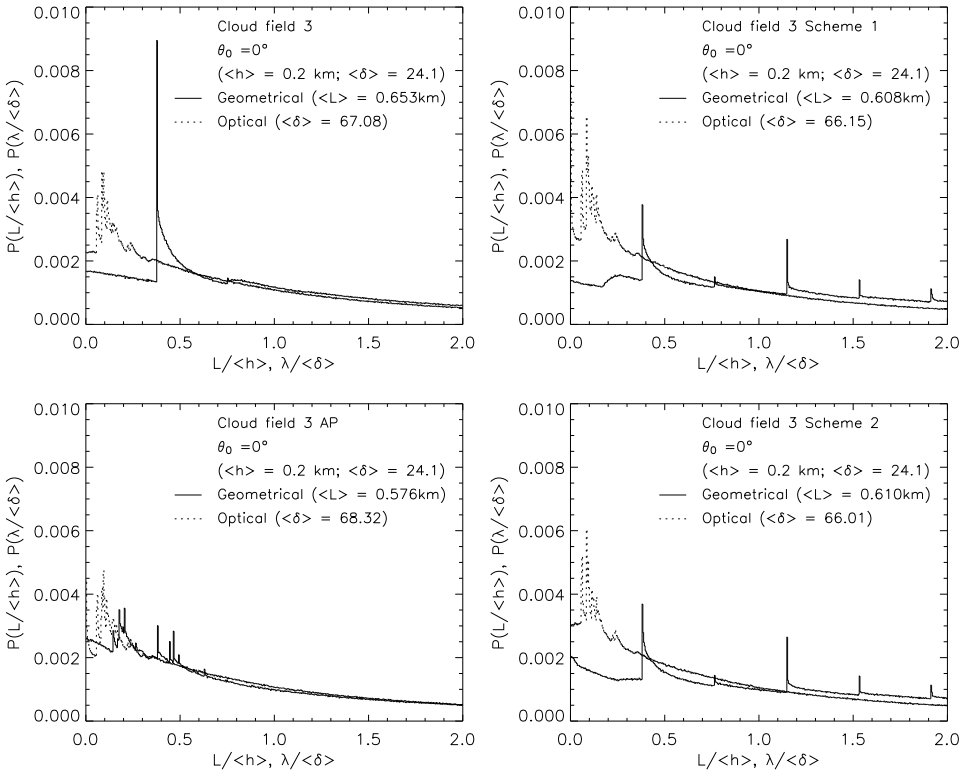

Figure 5.5: Probability distribution functions of scaled geometrical and optical pathlengths in the cloud for all realizations of cloud field 3 ($\theta_0 = 0°$).

From the previous parts of the section it can be summarized that solely geometrical pathlength differences roughly reflect the cloud field reconstruction quality. Comparisons with the photon properties yield low correlation coefficients and no systematic patterns of correlations depending on cloud field characteristics, solar zenith angles, or local cloud field homogeneity suggesting further investigations. Even for parts of the cloud fields, identified by the WRA approach as reconstructed better than the remaining field, the deviation of photon path properties of the reconstructed cloud fields are not significantly lower. It has to be noted that due to the Monte Carlo method photon path properties and consequently their differences are the results of cloud field properties but also of random processes. The influence of the random processes is particularly not negligible when differences in microphysical as well as optical properties are small. This provides a chance for more reliable correlations when microphysical and optical properties of the cloud fields differ to a greater extent than in this study.

5.2 Differences between radiation results of original and reconstructed cloud fields

This section addresses the question of whether differences in microphysical and optical properties between original and reconstructed cloud fields are reflected by differences in reflectances and therefore an evaluation of the reconstruction quality by means of radiative transfer simulations will be feasible. Furthermore, the properties of photon pathes, analyzed in the previous section, are employed to gain deeper insight in the differences in reflectances though properties will not

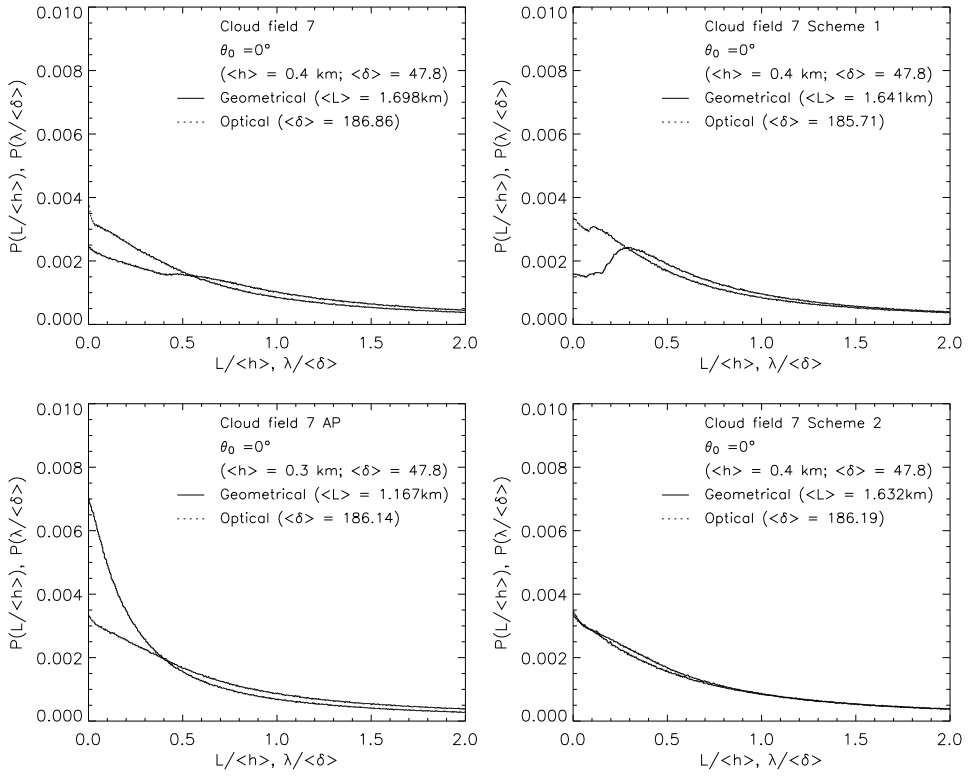

Figure 5.6: Probability distribution functions of scaled geometrical and optical pathlengths in the cloud for all realizations of cloud field 7 ($\theta_0 = 0°$).

be available from satellite radiation measurements. If the employment helps to interpret radiation differences, efforts to derive mean cloud-type dependent photon properties would be worthwhile.

In the Monte Carlo model radiance entering the detector from a certain direction is due to the local estimate approach the sum of the contributions of individual scattering events within the column, defined by the detector grid-cell and the local estimate direction. When radiances of non-nadir directions were examined, cloud properties have been calculated for the respective column. This was accomplished by tracking rays on their way from the sensor plane in the opposite local estimate direction down to the lower boundary of the domain. The starting points of the rays were distributed in a uniform pattern within the detector grid-cell. The track increments of identical microphysical properties were determined, and properties were interpolated on a predefined vertical reference grid by applying Eqs. 2.2 and 2.8. The overall properties of the column in a certain altitude were calculated as the average of the corresponding values derived by tracking the rays. Therefore, the accuracy of the calculated property increases with the number of rays. Optical properties like extinction coefficient or optical depth for the tilted column were derived by firstly determining microphysical properties and then applying Mie theory. The approach using tilted column properties is preferable, as recently shown by Evans et al. (2008). Analyzing simulated data of the Multiangle Imaging Spectro Radiometer (MISR) revealed that the reflectances of non-nadir viewing geometries are more related to the optical path in the respective direction than to the nadir optical depth of the column.

Due to the random nature of Monte Carlo simulations there will be differences in reflectances between individual simulations with the same cloud field. This noise was estimated by performing simulations for the original cloud fields twice and calculating the absolute differences in reflectances.

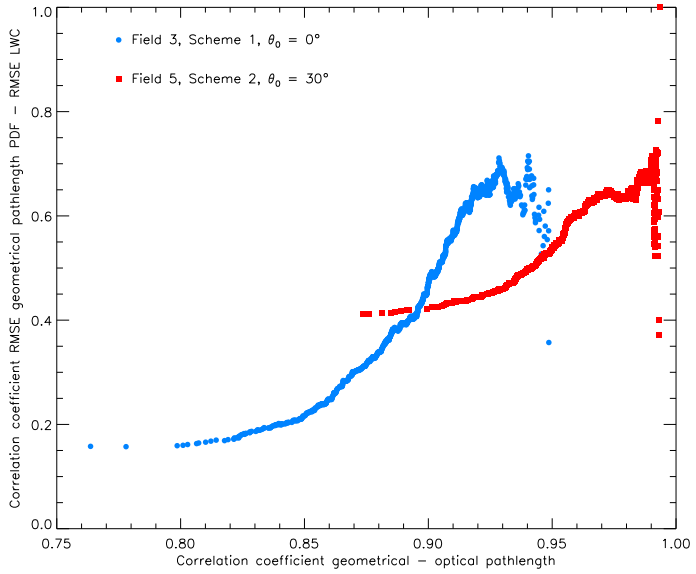

Figure 5.7: Dependence of correlation of the RMSE of the geometrical pathlength PDF on the homogeneity of the surrounding of the column described by the correlation of geometrical and optical pathlength.

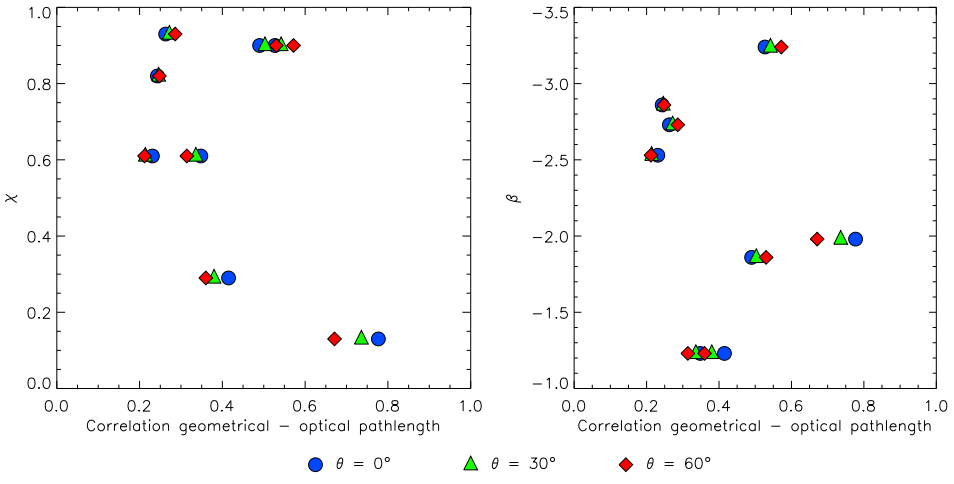

Figure 5.8: Comparison of pathlengths correlations, inhomogeneity parameter χ and slope of 1D power spectrum of optical depth β for the original cloud fields and all solar zenith angles.

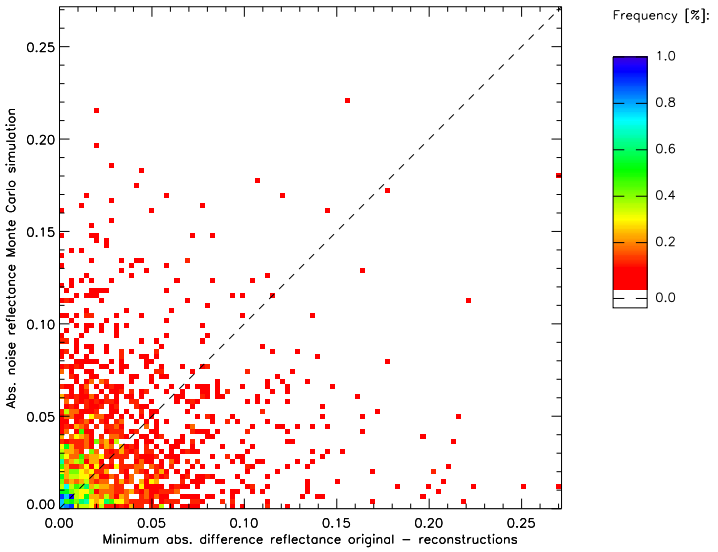

Figure 5.9: Comparison of Monte Carlo noise and the minimum of the absolute reflectance differences of cloudy columns. Differences were calculated between the realizations for the reconstructed cloud fields and the original cloud field found for every cloudy column (Cloud field 7, $\theta = 0°$, $\theta_0 = 0°$, $\phi_0 = 0°$).

In addition, the minimum and maximum absolute deviations of reflectances of simulations with reconstructed cloud fields from reflectances, simulated for the original cloud fields, were computed. The scatterplot of noise and minimum differences (Fig. 5.9) reveals similar magnitudes whereas maximum differences due to differences in microphysical and optical properties are for the majority of the cloudy columns larger than the noise (Fig. 5.10). Because optical depth in zenith direction was a constraint of cloud field reconstruction, differences between reflectances of reconstructed cloud fields and reflectances of original cloud fields in this direction may be caused by the random nature of the Monte Carlo simulations and also by differences in the profiles of optical properties and consequently horizontal photon transport. For the remaining radiance directions differences in reflectances may also be attributed to the differences in the tilted columns optical thickness. Figure 5.11 depicts the PDFs of the absolute differences in reflectances for the cloudy columns of all cloud fields, dependent on the radiance direction. It is evident that besides the differences in optical depth the differences of the other parameters have a considerable influence. This indication is supported by Fig. 5.12 where the probability distribution functions of scaled reflectances are depicted. Scaling of reflectances has been done by calculating the respective reflectance applying asymptotic radiative transfer approximations (e.g. Kokhanovsky et al., 2003). These approximations are valid when optical depth is sufficiently large so that a diffuse radiation regime establishes in the lower part of the cloud. Here a minimum optical depth of 10 is assumed to yield accurate results and consequently the PDFs in Fig. 5.12 consider only the respective columns. Reflectances calculated by asymptotic radiative transfer theory depend on the asymmetry parameter of the phase function, assumed as 0.85, cloud optical depth, as well as illumination and observation geometry. According to this, results can be considered as the plane parallel counterpart of the 3D Monte Carlo results, not taking into account profiles of radiative properties and horizontal inhomogeneities. Utilizing these

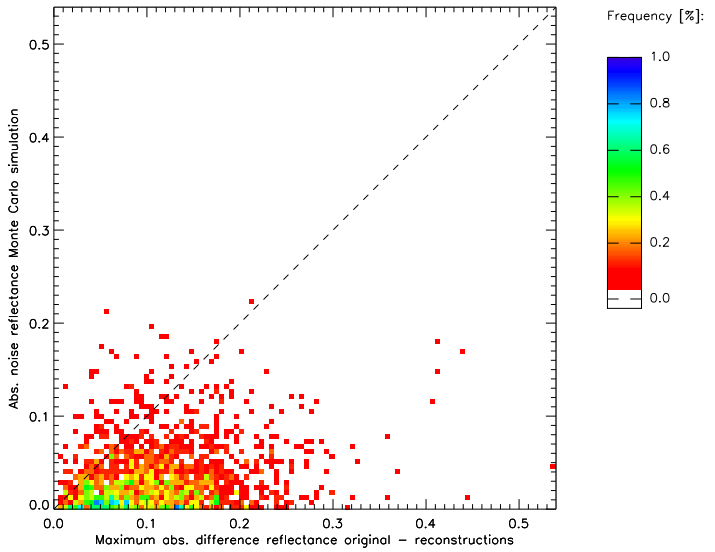

Figure 5.10: Comparison of Monte Carlo noise and the maximum of the absolute reflectance differences of cloudy columns. Differences were calculated between the realizations for the reconstructed cloud fields and the original cloud field found for every cloudy column (Cloud field 7, $\theta = 0°$,$\theta_0 = 0°$,$\phi_0 = 0°$).

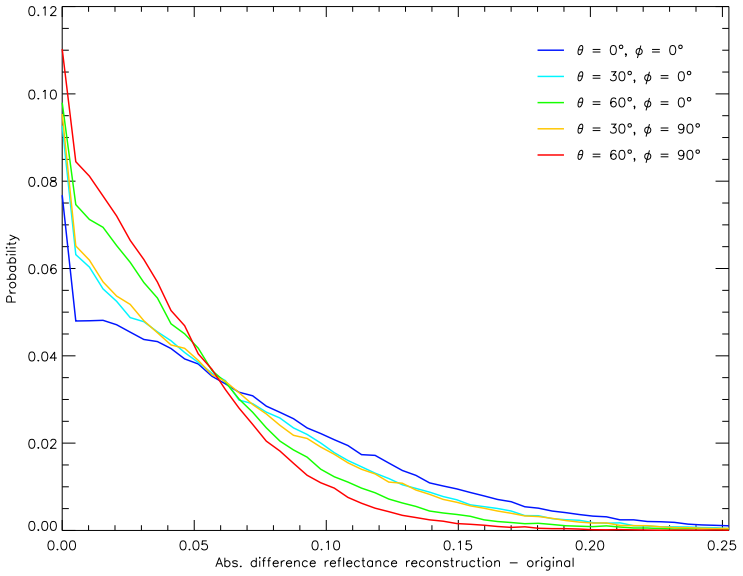

Figure 5.11: Probability distribution functions of the absolute differences in reflectance between realizations for reconstructed and original cloud fields for all radiance directions. The individual PDF enclose all solar zenith angles and reconstructions.

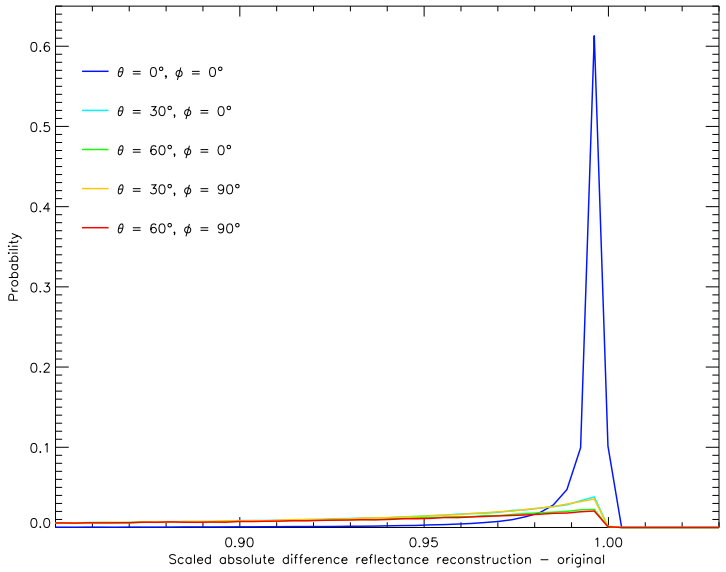

Figure 5.12: Probability distribution functions of the scaled absolute differences in reflectance between realizations for reconstructed and original cloud fields for all radiance directions. The individual PDF enclose all solar zenith angles and reconstructions.

properties, an estimate of the proportion of differences that are not caused by differences in cloud optical properties has been calculated as

$$\text{scaled\_ref} = ((\text{ref}_{\text{3d,rec}} - \text{ref}_{\text{3d,orig}}) - (\text{ref}_{\text{asym,rec}} - \text{ref}_{\text{asym,orig}}))/(\text{ref}_{\text{3d,rec}} - \text{ref}_{\text{3d,orig}}), \qquad (5.6)$$

where scaled_ref is the scaled reflectance and ref the reflectances of the individual realizations specified by the subscripts. The subscript 3d denotes the realizations derived by Monte Carlo simulations whereas asym refers to results derived by application of the asymptotic radiative transfer theory. Reflectances for the original and the reconstructed cloud fields are represented by the subscripts orig and rec, respectively. The PDFs of the scaled reflectance differences reveal that non-zenith directions exhibit also in this approach lower differences though here also differences in optical depth appear. Analyzing the reflectance differences for the the 'well reconstructed areas' as defined in Section 4.5, there are, for the most realizations listed in Table 5.1, less than 20% of reflectance differences smaller than the minimum differences of the remaining pixels.

In the following relationships between integrated properties like LWP as well as optical depth and reflectances will be examined. Because the relationship of the logarithm of the optical depth and the reflectance is approximately linear at least for one-dimensional radiative transfer (Duda et al., 1996), subsequent investigations were unless noted otherwise conducted with the reflectance as the exponent to the base e. For simplicity this transformed reflectance is denoted henceforth as 'reflectance'. An alternative approach would be to limit the investigations to the range where the relation between optical depth and reflectance is nearly linear, e.g. optical depths between 0.5 and 15 and reflectances not exceeding 0.4 (Evans et al., 2008).

Pearson correlation coefficients of optical depth and reflectances for all cloud fields, solar zenith angles, and radiance directions range between 0.2 and 0.95 with an average of 0.71. The permutation test reveals that all coefficients significantly differ from zero. There is a dilution of correlation with increasing cloud field number, which does not necessarily be accompanied by a reduction

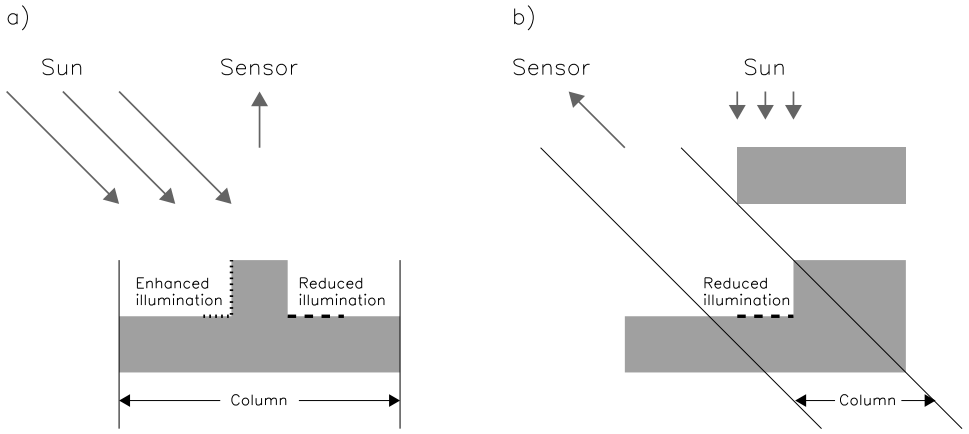

Figure 5.13: Situations where cloud shadowing appears: a.) Cloud-top is a subgrid variable but cloud shadowing has no net effect. b.) Cloud shadow in case of zenithal illumination.

of the confidence level because of an increase of cloudy columns. Coefficients also reduce with increasing solar zenith angle as well as increasing sensor zenith angle.

Large numbers of cloud columns with optical depths in this part of the optical depth - reflectance relationship where the reflectance encounters its saturation value result due to the linearization in an artificial strengthening of the correlation. To quantify this effect, correlation coefficients have also been derived for the subset of columns with optical depth less than 70. Whereas for some of the cloud fields, mainly the broken cloud fields, correlation coefficients for these subsets considerably increase compared to the entire set of cloudy columns, for the rest of the cloud fields correlations weaken so that cases appear for which the permutation test indicates non-significant correlations. When analyzing the subset defined by the linear regime, reflectances have not been linearized. Results have to be interpreted with caution because the sample size decreases rapidly applying the criteria for the linear regime so that in the end sample size is not sufficient for these computations for cloud field 8 and also some other tilted cloud field realizations. For most of the remaining realizations, correlations markedly decrease compared to the cases with all cloudy columns and numerous coefficients become non-significant.

An increasing decorrelation with increasing solar or sensor zenith angles might be an indication for shadowing effects due to cloud-top variability. Shadowing means that parts of the cloud-top do not receive the complete insolation because shadowing elements are found in direction of the illumination. This leads to a reduced reflectance accompanied by a dilution of the reflectance-optical depth relationship. If optical depth in nadir direction is analyzed, cloud shadows are solely determined by the solar zenith angle. Thus, in scenes where clouds are illuminated from the zenith direction, no cloud shadows appear. The situation becomes more complicated when cloud-top is a sub-grid variable with respect to the radiative transfer and also when tilted columns are analyzed. When cloud-top is a sub-grid variable it may happen that the shadowed part as well as the part of the shadowing element receiving enhanced illumination are in the same sensor pixel (Fig. 5.13 a). In this case there is no net-loss of radiation and shadowing effects can be neglected. Having this situation in mind, cloud shadowing may be defined as an effect where cloud-top or parts of the cloud-top receive reduced insolation due to shadowing elements not belonging to the considered column. When tilted columns are considered, furthermore situations may appear where multi-layer vertical cloud columns are truncated by columns tilted in sensor direction so that the lower

Table 5.5: Subsets of cloudy columns

Denotation	Criteria
all	all cloudy columns (LWP > 0)
below reflectance saturation	optical depth ≤ 70 and LWP > 0
linear regime	$0.5 <$ optical depth < 15 and reflectance ≤ 0.4 and LWP > 0
no cloud shadow	none of 64 rays per column intersected by shadowing cloud elements and LWP > 0
well reconstructed areas	fulfill the criteria for well reconstructed areas of respective parameter and LWP > 0

cloud layer belongs to the respective tilted column but the upper layer does not (Fig. 5.13 b). Due to the definition of cloud shadowing in this situation also cloud shadows may appear when insolation enters from zenithal directions. In order to account for these effects, cloud fields have been analyzed by a ray-tracing algorithm identifying relevant cloud shadows. The subset of cloudy columns presented above and used in the following to analyze the relations between cloud properties and radiation are summarized in Table 5.5.

For the analyzed cloud fields cloud shadow effects seem to be of minor importance. Besides increases of correlation coefficients also decreasing coefficients compared to the overall datasets occur. The magnitudes of the changes are so small that all coefficients remain significant and one may hypotize that other effects like horizontal transport may counterbalance this effect.

In order to examine a potential dependence of the relationship upon the local homogeneity, plots like Figure 5.7 were analyzed. Though several realizations appear where the correlation between optical depth and reflectance increases for columns with higher correlation between optical and geometrical pathlength, several very different patterns also occur. Analogous investigations for the LWP-reflectance relationship show similar results with slightly reduced correlation coefficients indicating a close LWC-extinction relationship typical of adiabatic or nearly adiabatic cloud profiles.

The correlations of the differences in optical depth between reconstructed and original cloud fields and the corresponding differences in reflectances range between -0.19 and 0.61 with an average of 0.16 for all cloudy columns. The permutation test indicates on the 0.95 confidence level for 12% of the realizations a correlation coefficient not differing significantly from zero. The strength of the correlation does not depend on the illumination or observation geometry. When examining the subset of columns with optical depth below 70 the mean value increases to 0.21 but concurrently the number of significant cases reduces by 2%. For the subset defined by the linear regime markedly higher coefficients are found for lots of realizations. Due to the occasionally low sample size significance tests might here not be meaningful and so do not contribute to characterize the results. The reduction of the sample of all cloudy columns by the columns affected by cloud shadows does not strengthen the correlation. On the other hand the number of realizations with significant correlations reduces by 8.

Coefficients for the differences in LWP and reflectances also exhibit only weak correlations between -0.53 and 0.37 with a mean value of -0.02 and 25% of the coefficients not differing significantly from zero. Applying the sampling rules for the subset of columns with optical depth corresponding to the not asymptotic part of the reflectance function, for the linear linear regime as well as for the

columns not affected by cloud shadows do not yield strengthened correlations. The percentage of not significant cases remains for all samplings above 25%.

Because correlation coefficients are a feature of each realization for an individual reconstruction scheme and therefore may vary for the same solar and observational geometry from scheme to scheme, the question arises whether it is possible to infer from reflectance differences the most appropriate reconstruction scheme. Figure 5.14 presents results of a classification where differences in reflectances and optical depth computed for cloudy columns of the reconstruction schemes and the original cloud fields schemes have been ranked and compared with each other. Class 1 (C1) encloses all pixels where the ranking of the reflectance differences reflects the ranking of optical depth differences. Remaining pixels where the minimum differences in reflectance and optical depth appear for the same scheme so that at least the determination of the most appropriate scheme is possible are covered by class 2 (C2). The rest of the pixels belong to class 3 (C3). An example to illustrate the classification approach is given below.

$$
\begin{array}{lllllllll}
\mathrm{ref}_{\mathrm{AP}} - \mathrm{ref}_{\mathrm{orig}} & < & \mathrm{ref}_{\mathrm{S1}} - \mathrm{ref}_{\mathrm{orig}} & < & \mathrm{ref}_{\mathrm{S2}} - \mathrm{ref}_{\mathrm{orig}} & \& & & & \\
\delta_{\mathrm{AP}} - \delta_{\mathrm{orig}} & < & \delta_{\mathrm{S1}} - \delta_{\mathrm{orig}} & < & \delta_{\mathrm{S2}} - \delta_{\mathrm{orig}} & & \rightarrow & \mathrm{C1} \\
\mathrm{ref}_{\mathrm{AP}} - \mathrm{ref}_{\mathrm{orig}} & < & \mathrm{ref}_{\mathrm{S2}} - \mathrm{ref}_{\mathrm{orig}} & < & \mathrm{ref}_{\mathrm{S1}} - \mathrm{ref}_{\mathrm{orig}} & \& & & & \\
\delta_{\mathrm{AP}} - \delta_{\mathrm{orig}} & < & \delta_{\mathrm{S1}} - \delta_{\mathrm{orig}} & < & \delta_{\mathrm{S2}} - \delta_{\mathrm{orig}} & & \rightarrow & \mathrm{C2} \\
\mathrm{ref}_{\mathrm{AP}} - \mathrm{ref}_{\mathrm{orig}} & < & \mathrm{ref}_{\mathrm{S1}} - \mathrm{ref}_{\mathrm{orig}} & < & \mathrm{ref}_{\mathrm{S2}} - \mathrm{ref}_{\mathrm{orig}} & \& & & & \\
\delta_{\mathrm{S2}} - \delta_{\mathrm{orig}} & < & \delta_{\mathrm{S1}} - \delta_{\mathrm{orig}} & < & \delta_{\mathrm{AP}} - \delta_{\mathrm{orig}} & & \rightarrow & \mathrm{C3}
\end{array}
$$

It becomes obvious that for all solar and observational geometries not less than 50% are enclosed in class 3 so that for these pixels the information of reflectance differences is completely misleading when the favourable reconstruction scheme has to be chosen. For the rest of the pixels minimum reflectance difference will at least determine the appropraprite reconstruction scheme.

So far only integrated values not providing any information about differences in the vertical distribution of scatterers were analyzed. To infer if reflectances inherit also information about the reconstruction quality of the profiles for every cloudy column the RMSEs of extinction coefficient as well as LWC for cloudy levels were calculated. The relationship of these RMSEs to the absolute differences in the antilogged reflectances were analyzed. Pearson correlation coefficients for the extinction coefficient range between -0.11 and 0.62 with an average of 0.21. Results of the permutation test indicate for 15% of the coefficients no significant differences from zero with most of them found for the cloud fields with high optical depths. Analyzing the results for the subsets of columns defined by the increasing part of the reflectance function as well as the unshadowed columns yields decreasing coefficients and an increase of non significant realizations up to 20% and 16%, respectively. For the linear regime subset few cases are found where the correlation strengthens but for most cases coefficients reduce. The coefficients for the differences in the LWC RMSE and the reflectance differences do not differ notably. For both parameters, extinction coefficient and LWC, correlations do not depend on the local homogeneity described by pathlength distributions. Analyzing a classification as shown in Fig. 5.14 for the RMSEs of extinction and LWC, in nearly all realizations only about 20% of columns are assigned to one of the classes where the most appropriate reconstruction scheme is detected.

As the analysis of the photon penetration depths has demonstrated, not all parts of the clouds contribute uniformly to the radiation signal. A limiting case occurs when all photons are either scattered or absorbed in the upper part and additional cloud matter in the lower part does not influence the radiation resulting in the saturation of the reflectance function for high optical depth (Harshvardhan et al., 2004). Platnick (2000) suggests to count the number of scattering events

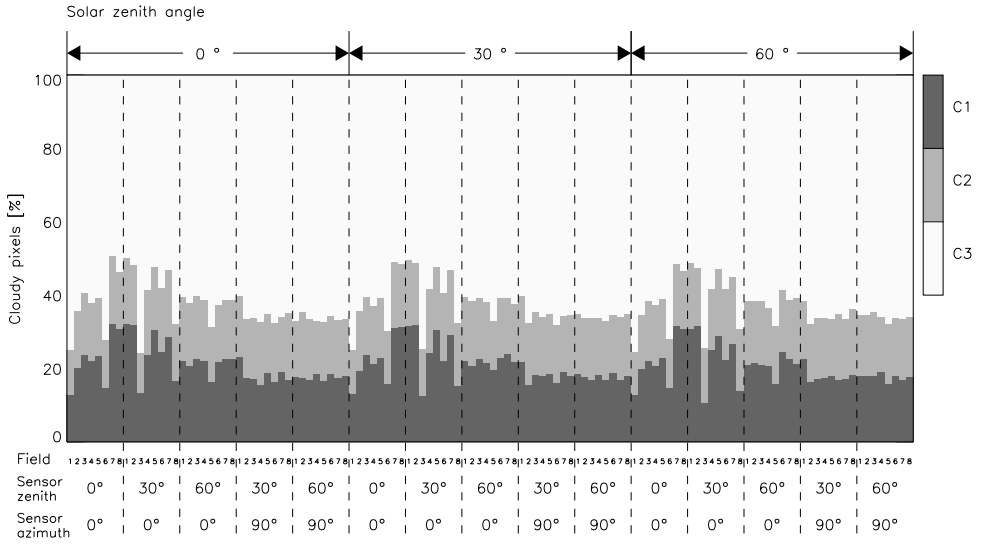

Figure 5.14: Classification results of the ranking of absolute reflectance differences and absolute differences in optical depth. The class C1 encloses these columns where the ranking of reflectance differences corresponds to the ranking of the differences in optical depth. Class C2 contains the columns where the minimum difference in reflectance and the minimum difference in optical depth is found for the same reconstruction scheme. The remaining columns are assigned to class C3.

in each cloud layer and subsequently to make use of the derived profiles as weighting functions to relate cloud optical properties and reflectances. Because positions of the individual scattering events were not stored, in the present study the penetration depth of the individual photons were used for substitution. Though this information is not available from remote sensing, it will be interesting to see if the application of the weighting functions improves the correlations of the differences in microphysical as well as optical properties and the radiation of the respective column. If this is the case one could think about trying to generate representative weighting functions for several cloud types. When weighting functions are derived from penetration depths of the photons there are two approaches referring to varying conceptions of photon pathes. The first one assumes that every photon was scattered once before leaving the cloud and entering the detector and that this event took place in the layer indicated by the penetration depth. This approach is denoted as the single-scattering approach (Fig. 5.15). When cloud optical depth increases photons will be scattered several times before and after the event located in the penetration depth. The number and positions of the individual scattering events have not been recorded, so that the only available information is that additional scattering events may have taken place between the penetration depth and cloud-top. Consequently, weighting functions of this multiple-scattering approach are modeled as the cumulated profiles of the single-scattering weights (Fig. 5.15) as

$$w_i = \int_0^i n(z)dz \tag{5.7}$$

with w_i the weight in height i and $n(z)$ the number of photons encountering the penetration depth z.

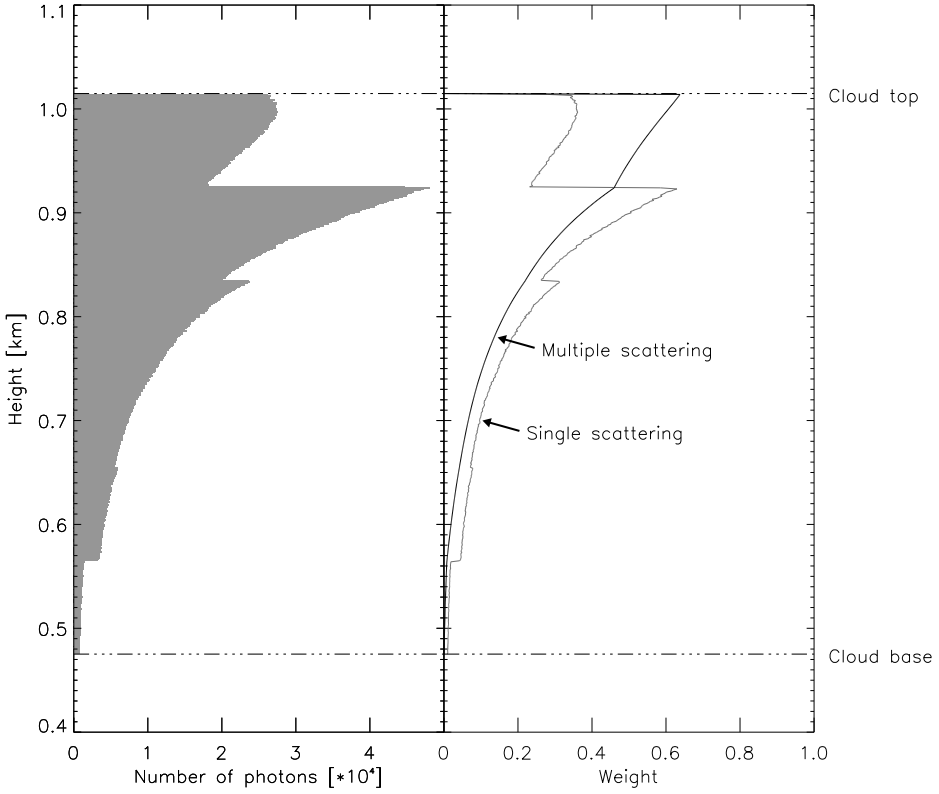

Figure 5.15: Profiles of the penetration depth of photons and the resulting weighting functions for the calculation of weighted RMSE (Cloud field 11, $\theta_0 = 0°$).

It should be noted that both weighting functions are most reliable for plane-parallel clouds. Especially the multiple-scattering weighting functions will not be appropriate when effects like channeling occur where photons propagate deep into the clouds by passing areas of reduced extinction. Another effect diminishing the reliability is entrainment of dry air at cloud-top leading to reduced extinction whereas the function assigns the maximum weights to these layers. Both approaches were employed when deriving global weighting functions from the entire set of photons. Additionally, local weighting functions were obtained by subsets of photons. By means of these functions weighted RMSEs were calculated as

$$\text{weighted RMSE} = \sqrt{\frac{1}{\sum_i w_i} \sum_i w_i \cdot (a_{i,rec} - a_{i,orig})^2} \tag{5.8}$$

where w_i is the weight of layer i and $a_{i,rec}$ as well as $a_{i,orig}$ are the values of the considered parameter of the reconstructed and the original cloud field, respectively. The weighting functions were derived from photons of the original cloud field, and the RMSE were solely calculated for cloudy layers.

Examining the correlations derived by applying the global weighting functions there are no significant or systematic differences in the correlation coefficients of the RMSE of extinction coefficient and the absolute difference in reflectance for the single-scattering and the multiple-scattering approach. This is the case for all subsets listed in Table 5.5. Application of the weighting functions leads to slightly reduced correlations coefficients compared to homogeneous weighting of devia-

tions except for the subsets characterizing the linear regime. Here, coefficients slightly increase for most realizations but stay in a range not indicating reliable relationships. A possible explanation could be that largest differences in extinction coefficient appear in the height where the weighting functions have their maximum and therefore weighting functions do not alter the RMSE significantly.

However, local weighting functions implying the single-scattering assumption degrade the correlation for scattered cloud fields may be due to extensive lateral photon transport and therefore inaccurate assignment of the penetration depth to the position where the photons left the cloud propagating towards the detector. In case that all cloudy columns are examined, the degradation results in about 12% more realizations for which the permutation test indicates a non-significant correlation compared to the analysis with global weighting functions. Similar results were found for the other subsets. Because cumulation of the weights leads to a smoothed weighting function, the correlation coefficients for the local multiple-scattering approach also reduce but the degradation effect is much less pronounced. Consequently, like for the global weighting functions also for the local weighting functions the magnitudes of the coefficients are low not contributing to a further explanation of the relationship between cloud property and reflectance differences. Analyzing the RMSE of liquid water content and reflectance differences results are very similar to the results found for the extinction coefficients. The only systematic difference, but with negligible magnitude, is that correlation coefficients increase when applying the global weighting functions compared to results without weighting functions.

As shown in several studies (e.g. Meyer, 2006; Várnai and Davies, 1999; Várnai and Marshak, 2001) the radiation measured within a pixel is not exclusively determined by the properties of the respective column, but because of horizontal photon transport also by the radiative properties of the surrounding columns. In the final attempt to explain differences between the reflectances of original and reconstructed cloud fields of the present study, several photon path properties were combined to derive highly simplified three-dimensional weighting grids. Besides the vertically varying influences of cloud properties on the radiation, these weighting grids will also take horizontal transport effects into account. It has to be noted that these grids are far from being parametrizable for different cloud types, but if their application sheds more light on the problem how to explain radiation differences by means of differences in microphysical and optical properties, further investigations beyond the scope of this study may be worthwhile.

The three-dimensional weighting grids were reconstructed for every cloudy column using the subset of photons leaving the cloud in upward direction within the respective column. The subset has further been reduced by omitting photons with penetration depths lower than the mean cloud-base to ensure that photons that have possibly undergone excessive horizontal transport but are small in number, will blow up the weighting grid. For each of the remaining photons a simplified path was simulated, making use of the position where the photon left the cloud in upward direction, its penetration depth, and its geometrical pathlength in the cloud (Fig. 5.16). Regardless of the real path it was assumed that the photon encountered at least one but not more than three scattering events. The mandatory scattering event took place in the height of the penetration depth. Before and after this scattering event the photon propagated equal pathlengthes in the cloud, namely half of the overall geometrical pathlength in the cloud. To ease the reconstruction cloud-top height for the step of the path reconstruction was assumed as homogeneous. Because propagation directions of the photons are simplified and consequently do not depend on solar and sensor zenith angle, the simulation allows for additional scattering events at the temporary cloud-top. Due to missing information about the propagation directions of the photons in the cloud, all photons were supposed

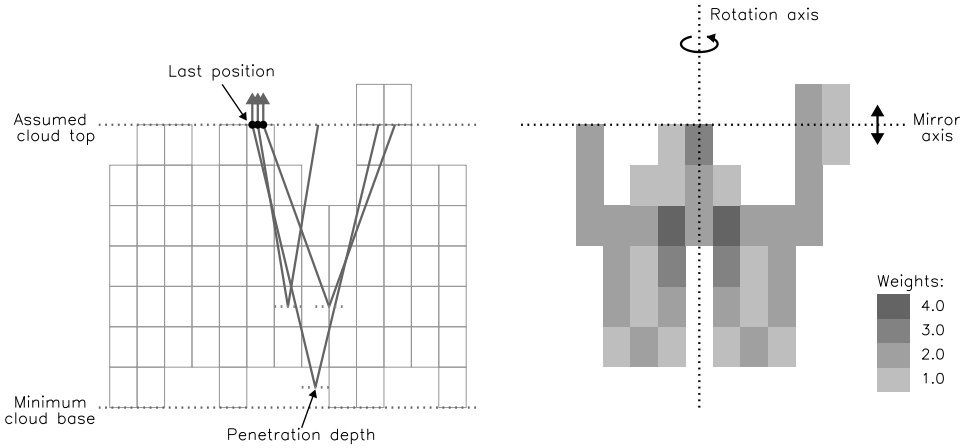

Figure 5.16: Schematic depiction explaining the reconstruction of simplified photon pathes and the weighthing grid for the respective column. The photon path properties were applied to derive a simplified path in a predefined direction. The number of passing photons determined the weight for every gridcell. Weights were then rotated and mirrored to complete the 3d-weighting grid.

to have the same azimuthal direction not changing after the scattering event. The number of the passing photons determined the weight of the respective grid-cell. The derived weights were then remapped isotropically by rotation around the vertical axis passing through the center of the considered column. Because of the periodic boundary conditions in the Monte Carlo simulations rotation of the weights was not limited by the edges of the domain and weights were also assigned to columns at the opposite side. It has to be noted that there was no need to take the varying sizes of the columns due to the uneven spacing into account when rotating the weights. Finally, the weights were mirrored vertically not to miss the influence of cloudy cells above the assumed cloud-top. In case of non-zenithal radiance directions, weighting grids were reconstructed for the zenithal case, but then tilted to match the radiance direction. Like the one-dimensional weighting functions also the three-dimensional weighting grids were calculated by using photon properties derived from Monte Carlo simulations for the original cloud fields.

Applying the grids to cloudy grid-cells, weighted RMSEs of cloud properties were derived. In addition weighting grids were used as indicator variables to deduce unweighted RMSEs for the subset of cells where the weight was different from zero. The results exhibit for the parameters extinction coefficient as well as liquid water content correlation coefficients significantly reduced compared to the coefficients calculated with columns-wise RMSEs. These findings are valid for both approaches, that one using the weighting grid as an indicator variable and that one employing weighted RMSEs. This implies that a highly simplified approach, like the one used here, is not capable to explain to a greater extent the relationship between the differences in reflectances simulated for the reconstructed and the original cloud fields and the respective differences in their optical and microphysical properties.

All efforts in this section reveal, that even when additional information not measured by satellite instruments and difficult to parametrize are applied, differences in reflectances reproduce differences in cloud microphysical and optical properties only to a minimum extent. Thus, approaches presented before do not enable to evaluate the reconstruction quality by radiation measurements. Besides the inability to provide information about the quantitative differences between cloud columns

of reconstructed and original cloud fields, differences are also only able to provide qualitative information about the reconstruction schemes for subsets of cloud columns.

Chapter 6

Influence of ancillary parameters

The results of the radiative transfer simulations presented in the previous chapter are characterized by various simplifications compared to real-world atmospheric situations. Simplifications either consist of neglecting and predefining parameters or describing their influence by simplified models. Because the magnitude of the uncertainties due to the simplifications is unknown, cases may arise where uncertainties exceed differences originating from deviations of cloud field reconstruction. This chapter presents assessments of the uncertainties caused by simplified treatment of individual parameters. This is done with respect to the differences caused by inaccurate cloud field reconstruction. The considered aerosol profiles belong to the group of parameters that were completely omitted in previous simulations. The surface reflection was simplified by assuming Lambertian albedo instead of applying a more realistic reflection function depending on the photon propagation direction. Before the influence of a more sophisticated treatment of both parameters is analyzed, results of an investigation are presented where the horizontal resolution of the cloud field was reduced. This may shed light on the question if correlations, analyzed in the previous chapter, will strengthen when intercolumn horizontal photon transport reduces and consequently radiative properties are determined to a greater extent by the microphysical and optical properties of the underlying column.

6.1 Influence of horizontal resolution

The effect of horizontal photon transport between adjacent columns may blur potential relationships between differences in microphysical and radiative properties in the considered column. In the previous chapter attempts were described to include this effect by means of simplified three-dimensional weighting grids. Here the problem is addressed by an alternative approach in which cloud fields are remapped onto a grid with reduced horizontal resolution. As a consequence photons will pass less columns and so the radiation signal will be determined to a greater extent by the properties of the respective column. As an aside-effect it is expected that radiation and photon property statistics become more robust by this approach. Rephrasing the task the questions shall be discussed if results derived in the previous chapter are scale-dependent and if consequently more reliable dependencies will appear when cloud fields approach their plan-parallel reference. The mean horizontal cell size of original and reconstructed cloud fields varies from ∼240 to ∼480 m. Marshak et al. (1995) introduced the smoothing scale η to describe the influence of horizontal photon transport on radiances of cloud fields. They derived η applying diffusion theory as

$$\eta \approx \overline{h}/\sqrt{(1-g)\overline{\delta}} \tag{6.1}$$

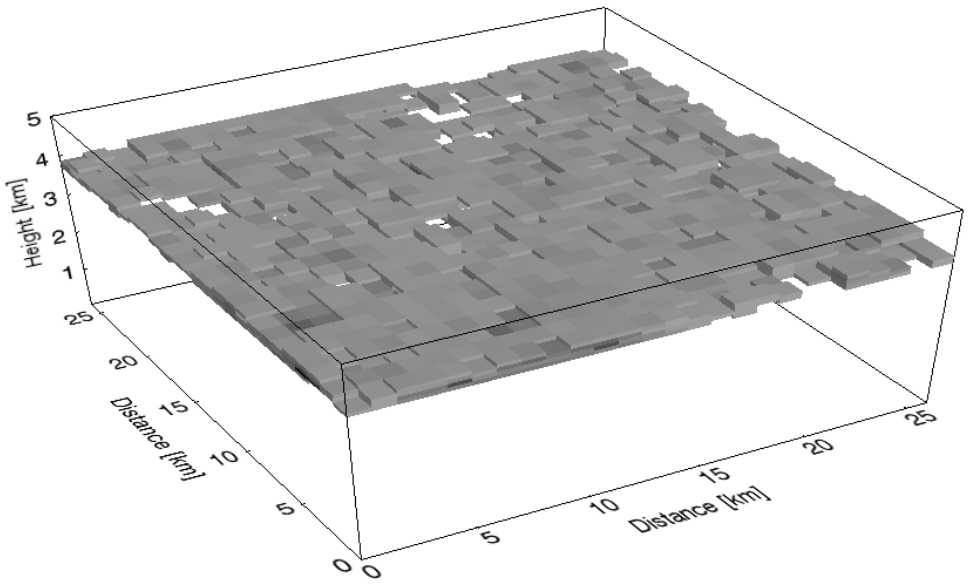

Figure 6.1: Cloud field from Fig. 3.1 with reduced horizontal resolution.

where $\overline{h}$ is the mean geometrical thickness, g the asymmetry parameter of the scattering phase function and $\overline{\delta}$ the average optical depth of the cloud. Neglecting cloud-free columns by averaging optical depth and geometrical thickness of cloudy columns and assuming an asymmetry parameter of 0.85, smoothing scales for the original cloud fields range between 100 and 200 m. Though this scale is smaller than the horizontal resolution of the cloud fields, photon pathlengths suggest more extended lateral photon transport leading to an enhanced smoothing effect. To shed light on the influence of the horizontal resolution cloud fields were regridded preserving the vertical resolution but averaging microphysical properties on an evenly spaced 1 km horizontal grid. The optical properties were subsequently derived by applying Mie theory using the same droplet size distribution characteristics as in previous calculations. The regridded cloud fields corresponding to cloud fields in Fig. 3.1 and 3.2 are depicted in Fig. 6.1 and 6.2, respectively.

Analogous to the cloud fields with original resolution, data sets retrievable from measurements of satellite-mounted instruments (illustrated in Fig.1.1) were compiled for the regridded fields. The reconstruction of the entire cloud fields were accomplished by employing Scheme 1. Radiative transfer simulations were performed with the same number of photons as in previous calculations.

A straight comparison of relationships between microphysical as well as optical properties and radiation for cloud fields with original and reduced resolution is not feasible because regridding alters average optical properties as well as cloud fraction. However, systematic deviations of the correlations of differences in photon properties as well as reflectances and differences in microphysical properties due to the reduced photon transport from adjacent columns may be examined.

When results of Monte Carlo simulations are analyzed, no significant strengthening of correlations between microphysical and photon property deviations is found. The maximum Spearman rank correlation coefficient of the RMSE of photon penetration depth and the RMSE of extinction coefficient, LWC and effective radius is 0.214 and like for the cloud fields with original resolution a permutation test reveals that for roughly 41% of the simulations the correlation coefficient does not differ from zero on the 0.05 significance level. The changes of the correlation between the RMSE

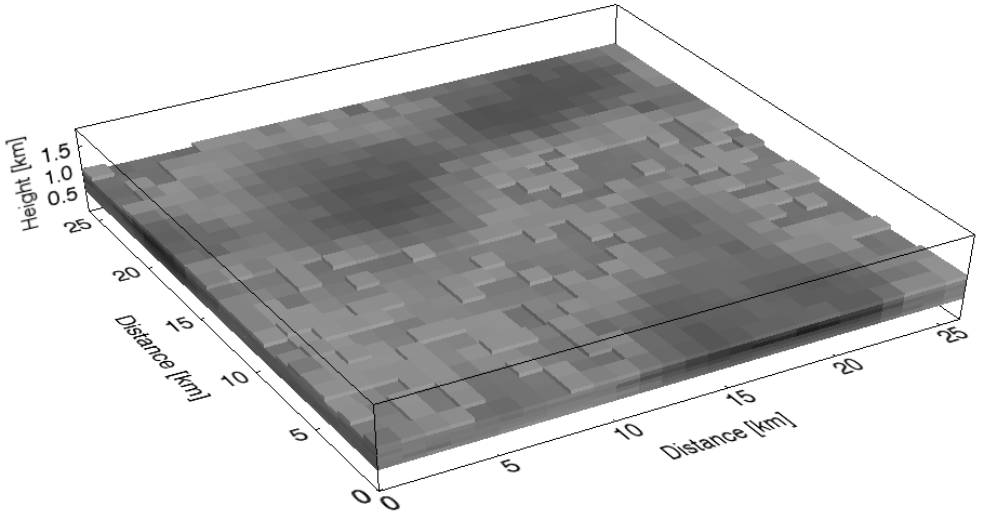

Figure 6.2: Cloud field from Fig. 3.2 with reduced horizontal resolution.

of geometrical pathlength in the cloud and the RMSE of optical and microphysical properties due to reduction of the resolution are ambiguous. Both enhanced and weakened correlations appear. Whereas the permutation test identified each correlation coefficient for realizations with fine grid cloud fields reconstructed by means of Scheme 1 as differing significantly from zero, cases with correlations not differing significantly from zero for cloud fields with reduced resolution exist. A similar situation is found for profiles of mean geometrical pathlength. The signs of the differences in the correlation coefficients compared to the original cloud fields (which have been very low anyway) vary and even coefficients of fields with an enhanced correlation do not reach values indicating robust correlations. The changes of the correlation coefficients are accompanied by an increase of realizations with coefficients not differing significantly from zero. Comparing Fig. 6.3 with Fig. 5.5 pathlength distributions do not provide an evidence for more homogeneity.

Examining reflectances its has to be noted that besides internal inhomogeneity also external inhomogeneity describing for example the cloud-top variability has been reduced by regridding, which will also have a fundamental influence on radiation results. As expected the degree of correlation of antilogged reflectances and liquid water path as well as optical depth increases for

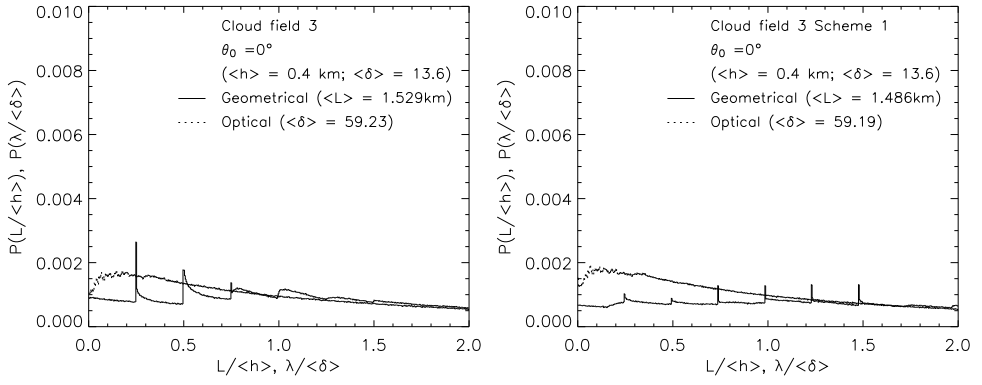

Figure 6.3: Probability distribution functions of scaled geometrical and optical pathlength in cloud for realizations with regridded original and reconstructed cloud field (Cloud field 3, $\theta = 0°$).

nearly all of the remapped cloud fields compared to the original ones. The largest magnitudes of increase appear for fields with numerous columns located in the asymptotic part of the optical depth - reflectance relationship. Analysis of the relation of differences in optical depth as well as liquid water path and differences in the antilogged reflectances yield no clear increase of correlation coefficients. Whereas for the liquid water path nearly all simulations show unaltered or decreased coefficients compared to simulations with original resolution, there are several realizations where the correlation between differences in optical depth and differences in reflectances is strengthened markedly. At the same time numerous cases with weakened relationships. These changes are not organized in a systematic pattern depending on cloud field, solar or sensor geometry.

As for original cloud fields also for the columns of the regridded cloud fields RMSEs of non-integrated properties like liquid water content, extinction coefficient and effective radius describing profile differences between the original and the reconstructed cloud fields were computed. Accordingly, correlation coefficients between the RMSEs and the absolute differences in the antilogged reflectances were calculated. In accordance to coefficients determined for the integrated properties also for correlation coefficients taking into account the deviations of the profile various changes compared to the corresponding coefficients for the original cloud fields occur. A decrease of coefficients prevails and increasing ones do not follow a typical pattern depending on cloud field, solar or sensor geometry. Even the increasing coefficients do not enter a level where most of the variability of reflectance differences is described by the respective profile deviations.

Also correlations coefficients of penetration depth weighted RMSEs and absolute reflectance differences reveal no significant strengthening when analyzing the coarse grid realizations. On the contrary, the number of cases for which the permutation test detected a correlation coefficient differing significantly from zero decreases substantially. It makes no difference for these findings if local or global single or multiple-scattering weighting functions were applied. Analogous to the original cloud field realizations three-dimensional weighting grids combining photon path properties as well as corresponding grids consisting of an indicator variable were derived for coarse grid realizations. The maximum correlation coefficient for the weighting grid approach is 0.34 for LWC and 0.32 for extinction coefficient and the respective mean coefficients are about 0.05 for both parameters. Correlation coefficients applying the indicator grid are quite similar with maximum values of 0.32 for LWC and 0.33 for extinction coefficient and mean values for both parameter are in the range of 0.05.

Summarizing the results it can be concluded that remapping results in the expected strengthening of the correlations of the integrating metrics like liquid water path as well as optical depth and reflectances. An increase of correlation could not be found for the differences in the integrated parameters and the differences in reflectances and also not for deviations of spatially resolved differences in cloud properties and differences in reflectances.

6.2 Influence of aerosol profile assumptions

In the following section, the magnitude of the influence of varying aerosol profiles on the radiative transfer is investigated. Though the optical depth of aerosols is low compared to cloud optical depth neglection or simplification of aerosols may impose an error on simulated reflectances. Besides additional optical depth also the less pronounced forward peak of the aerosol scattering phase function compared to the scattering phase functions of water droplets might contribute to the error. If the magnitude of this error is large, less accurate treatment of aerosols will blur the differences in reflectances due to cloud field reconstruction and will prevent conclusions about

Table 6.1: Microphysical parameters of aerosol models

Model	Altitude (m)	H_p (m)	$N_d(0)$	$N_d(B)$	$N_d(i)$	$r_m(i)$	$\sigma(i)$	rh_t
mc	$\rightarrow$ 1000	75	1500	300	1	0.03	0.35	30
ru	$\rightarrow$ 2500	825	16500	300	0.999875	0.03	0.35	23
					0.000125	0.5	0.4	
tr	$\rightarrow$ tropopause		-	300	1	0.03	0.35	23

the accuracy of the reconstruction. The influence of aerosols is inferred from the differences in radiative tranfer simulations for the original cloud fields applying a maritime aerosol model with a continental background (mc) and a rural model (ru) in the boundary layer. This is owed to the fact that the measurement site is close to the sea and depending on the direction of advection it may either be influenced by maritime or continental air masses. In the free troposphere for both cases the same tropospheric model (tr) is applied. The parameters of lognormal size distributions for the aerosol profiles are listed in Table 6.1. The number densities of aerosol particles at the surface and in the background were adopted from the compilation published by Jaenicke (1993). The decrease of the the number density $N_d(z)$ in height z up to the free atmosphere is expressed by

$$N_d(z) = N_d(0)\left\{exp\left(\frac{-z}{|H_p|}\right) + \left(\frac{N_d(B)}{N_d(0)}\right)^v\right\}^v; \quad H_p \neq 0; \quad v = \frac{H_p}{|H_p|} \tag{6.2}$$

where $N_d(0)$ is the surface value, H_p is the scale height and $N_d(B)$ is the background value. In the free troposphere a tropospheric model with a height invariant number density was used. The rural model is described by a superposition of two lognormal size distributions whereas the maritime and the tropospheric model is characterized by an individual lognormal distribution (Shettle and Fenn, 1979). The single scattering properties for the dry profiles were calculated assuming refractive indixes of (1.53, 0.006) for the rural and the tropospheric model and (1.5322, 0.0105) for the maritime model. If relative humidity in the respective layer derived from interpolated radiosoundings exceeds a model-dependent threshold rh_t aerosols start swelling. The models describing the hygroscopic growth were adopted from Haenel (1976). Adjustment of aerosol radii dependent on humidity was done by an iterative procedure. Due to hysteresis effects models for water uptake and release exist whereas in the present study model parameters for water uptake were applied.

There are two approaches employed when calculating the single scattering properties for the wet aerosol profiles. The first one (Shettle and Fenn, 1979) assumed completely dissolved aerosol particles resulting in homogeneous spheres with a refractive index calculated as

$$n = n_w + (n_o - n_w) \cdot \left[\frac{r_o}{r_{a_w}}\right]^3 \tag{6.3}$$

where n_w is the complex refractive index of water, n_o the refractive index of the dry aerosol, r_o the radius of the dry aerosol and r_{a_w} the radius of the swollen particle. In this approach single scattering properties are derived applying a Mie routine for homogeneous spheres. The second approach refers to the other extreme where a water coat encloses the particle but no solution takes place. This approach makes use of a coated-sphere routine to calculate single scattering properties (Toon and Ackermann, 1981). The profiles of microphysical and bulk optical properties of cloud field 7 are displayed in Figure 6.4.

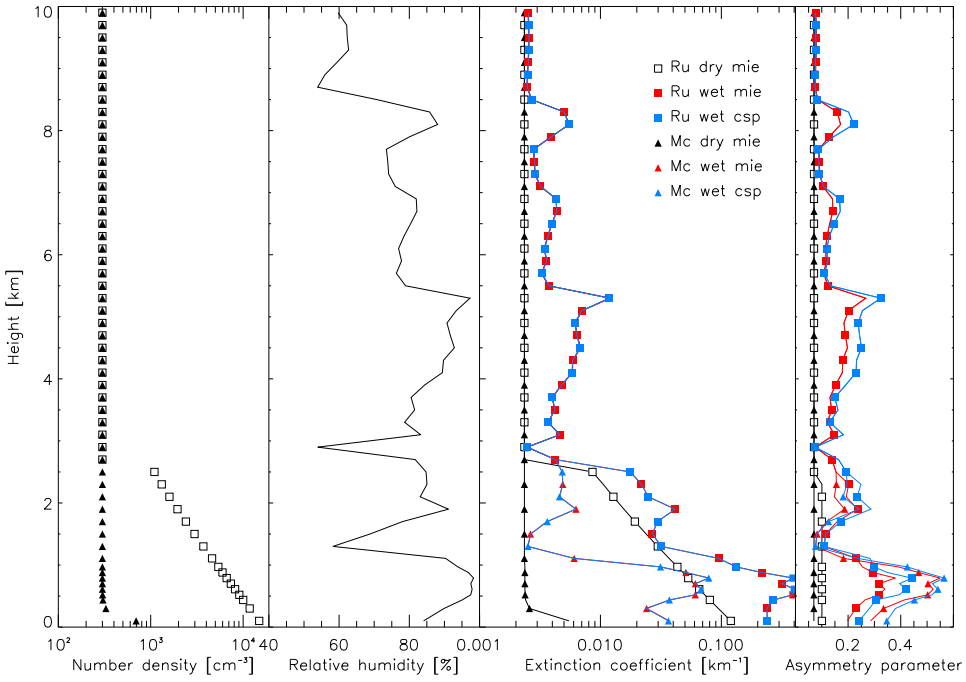

Figure 6.4: Microphysical and optical properties of profiles of wet and dry aerosol populations (Cloud field 7).

It becomes obvious that hygroscopic growth of aerosol particles increases significantly the extinction. The aerosol optical depth for the maritime model is between 8% and 290% larger than the corresponding value for the dry population. Wet rural profiles have a 7% to 240% larger optical depth. In the free troposphere aerosol extinction is the same for both models due to identical tropospheric models. There are no differences in the extinction depending whether the Mie routine for homogeneous spheres or the coated-sphere routine has been applied. However, examining the asymmetry parameter reveals remarkable differences between the phase functions where the forward direction is more pronounced by the coated-sphere routines when scatterers are sufficiently large. In order to assess the magnitude of radiative transfer results caused by the treatment of aerosols, additional simulations for the original cloud fields including the aerosols profiles were carried out. Because of difficulties to distinguish between cloud droplets and swollen aerosol particles, aerosol radiative properties were only considered in cloud-free grid-cells. Due to the less pronounced forward peak of the aerosol phase functions compared to water droplet phase functions variance reduction techniques like the phase function redistribution and the redistribution of radiation entering the detector and exceeding a certain threshold were not used in case of aerosol scattering.

There are two effects of the additional aerosols on the radiative transfer conceivable. Due to the enhanced extinction above the clouds photons free-pathlength is reduced and as a result more photons would be scattered towards detector without entering the cloud. This would weaken the relation of reflectances and cloud properties. The other effect is driven by the more pronounced forward scattering of the combined Rayleigh and aerosol phase function compared to the phase function in Rayleigh atmospheres and consequently photons scattered above the clouds are more likely scattered towards the clouds. Analyzing the results of the simulations the second effect is found to dominate and less photons are scattered back above the clouds towards the detector. For

all simulations the proportion of photons never encountering layers below cloud-top scales with the mean height of the cloud-top. Also the number of photons scattered back above cloud-top increases with increasing solar zenith angle. This effect is less pronounced for simulations taking aerosol scattering into account compared to aerosol-free simulations. Due to the same aerosol population applied in the free troposphere, differences are mainly found for cloud fields where cloud-top is located in the boundary layer of the aerosol model, namely cloud fields 7 and 8. Here, significantly more photons are scattered back to the detector when the rural model is applied. Except for few realizations also a considerable increase is found when water uptake of aerosols was taken into account. As mentioned before the pronounced forward peak of the aerosol scattering phase function compared to the Rayleigh scattering phase function is stated to be responsible for the reduced number of photons scattered backwards to the detector. This is in-line with the results for most of the realizations. A closer look at the results for cloud fields 7 and 8 reveals that effects may diminish when certain combinations of solar zenith angle and cloud-top height appear. Both water uptake of aerosols and application of the coated sphere routine promote an enhanced asymmetry parameter of the phase function, but nevertheless the number of photons scattered above the clouds is larger for these fields in simulations with a solar zenith angle of 60° compared to the aerosol-free references. The maximum percentage of photons scattered back to the detector is 2.1%, 2.4% and 4.1% for realizations without aerosols and solar zenith angles of 0°, 30° and 60°, respectively. Corresponding values of realizations with added aerosols are 1.1%, 1.6% and 4.6%.

Analyzing histograms (not shown here) reveals that systematic differences in reflectances derived for realizations applying the different aerosol models only appear for the cloud fields 7 and 8. Largest differences are found between results with pure Rayleigh scattering and the wet rural model calculated by the Mie approach. Comparing the realizations without aerosols and the rural model approximated by the coated-sphere-approach yields the second largest differences. Less pronounced differences but still markedly larger differences than the remaining combinations are found for realizations with dry maritime aerosols combined with realizations applying both types of wet rural profiles. The differences in reflectances do not depend on the solar zenith angle or the angles determining the radiance direction.

Comparison of absolute reflectance differences due to application of the different aerosol models including the aerosol-free simulations with reflectance differences caused by the noise of the Monte-Carlo simulations shows that for all cloud fields independent of illumination and observation geometry differences due to noise exceed the minimum differences found from the set of realizations incorporating the aerosol models. An analogous comparison of maximum absolute differences caused by the aerosol models and noise (Fig. 6.5) shows that differences due to aerosol models are for all realizations significantly larger than Monte-Carlo noise. The minimum absolute differences in reflectances calculated for the original cloud fields and reflectances simulated for the reconstructed cloud fields are for all cloud fields and geometries significantly larger than minimum differences due to different aerosol model applications. When minimum differences of the aerosol differences are replaced by the maximum differences, results of the comparison are reversed so that the aerosol treatment is responsible for the larger differences. Results of comparison become more complex when analyzing the maximum differences found from aerosol simulations as well as from simulations for the reconstructed cloud fields. Whereas cloud fields 1 to 3 are slightly biased to larger differences caused by inaccurate reconstruction (Fig. 6.6) the other cloud fields exhibit larger differences due to differences of aerosols. For cloud fields 4 and 5 this behaviour is less pronounced than for cloud fields 6 to 8 (Fig. 6.7).

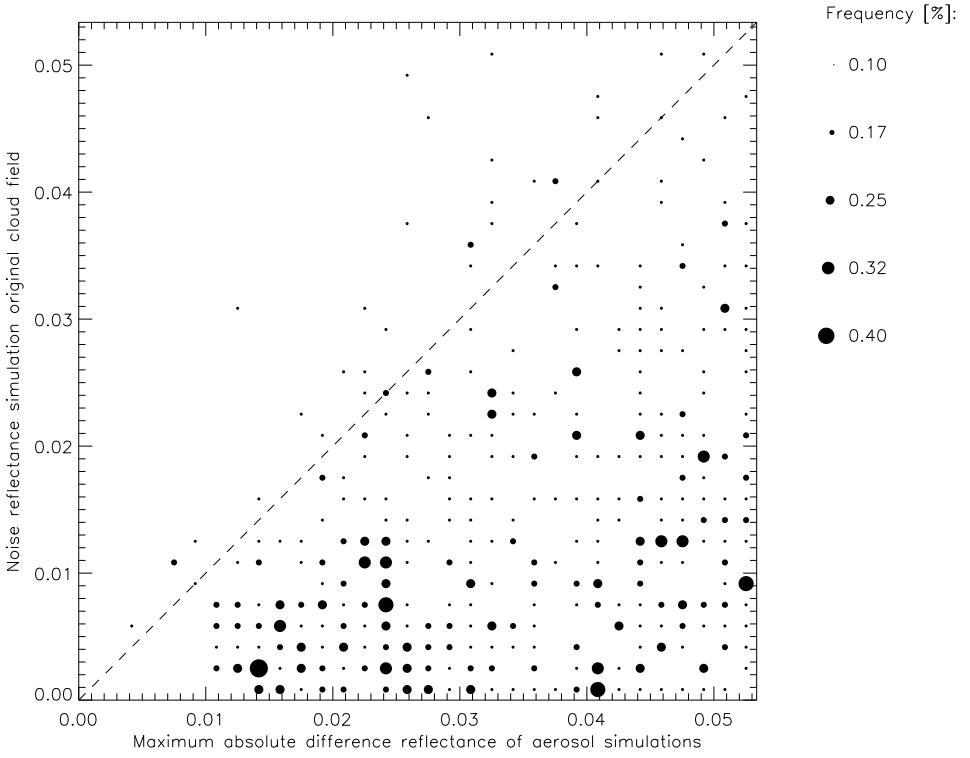

Figure 6.5: Comparison of maximum absolute differences in reflectances due to different aerosol models and Monte Carlo noise (Cloud field 3, $\theta_0 = 0°$, $\theta = 0°$, $\phi = 0°$).

From the results presented above it can be concluded that inappropriate assumptions about the aerosol profile or its neglection may blur the differences due to cloud field reconstruction. The situation especially becomes complicated when the maximum error imposed to the reflectances by inappropriate aerosol assumptions is taken into account, since the simulations have shown that the net effect depends on the individual cloud field and humidity profile.

6.3 Lower boundary conditions

In order to investigate the influence of the lower boundary conditions, the Monte Carlo model has been extended by a module to simulate surface reflection by a Bidirectional Reflectance Distribution Function (BRDF). The new direction of photons entering the surface is calculated due to the BRDF depending on the direction of the incoming photon. The new direction is determined by the random weighted BRDF, whereas the new direction is forced to have a zenith angle below a threshold value to avoid prolonged photon pathes below the clouds. The black-sky albedo depending on the incoming vector determines the weight of the outgoing photon.

For this study a BRDF of pasture land (Rahman et al., 1993) has been used. This function is illustrated for three illumination angles in Fig 6.8. It becomes obvious that this BRDF is characterized by predominant backward scattering concentrated in the so-called hot spot. Rahman et al. (1993) make the absence of shadows responsible for this effect. It is remarkable that a second maximum in the forward direction is missing.

Comparing the BRDF with an isotropic reflection function one would at least for photons reaching the ground through cloud gaps assume more photons scattered back through the same

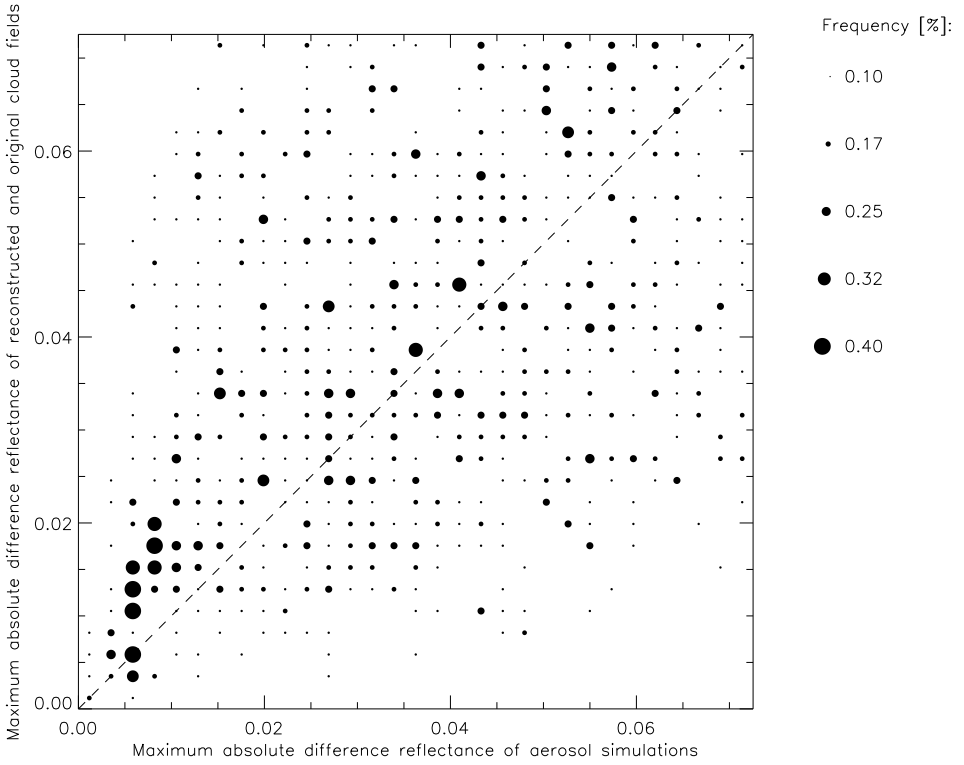

Figure 6.6: Comparison of maximum absolute differences in reflectances due to different aerosol models and maximum absolute differences in reflectances due to inaccurate reconstruction. The differences due to cloud field reconstruction are slightly large than the differences due to varying aerosol assumptions (Cloud field 3, $\theta_0 = 0°$, $\theta = 30°$, $\phi = 90°$).

gap due to the backscattering hot spot. This would lead to a reduced geometrical pathlength compared to pathlengthes simulated by applying the Lambertian model.

Except for 2 realizations (both with $\theta_0 = 60°$) all realizations for broken cloud fields show an increased number of photons reaching the ground and leaving the domain at the top without entering the clouds in simulations with the BRDF model compared to the Lambertian albedo. Compared to the noise due to Monte-Carlo uncertainty all increases are significant. When PDFs of radiance contributions of the photon reaching the ground, not entering the clouds and hitting the detector are analyzed, it is found that for simulations with $\theta_0 = 0°$ as well as $\theta_0 = 30°$ the radiance contribution of photons simulated by the aid of the BRDF is reduced compared to results simulated with Lambertian albedo. For simulations with $\theta_0 = 60°$ relations are reversed. This must be a consequence of the difference between white-sky albedo and black-sky albedo determining the weight after the scattering event. When pathlength distributions of photons that reached the ground, did not entered clouds and reached the detector are analyzed, results does not reveal that the pathlength of BRDF simulations is significantly shorter. More striking feature are the distinct peaks of the distribution compared to the more homogeneous PDF of Lambertian albedo simulations. The peaks are a result of the hot spot direction, preventing from a random walk through the domain. The same results are found when analyzing the pathlength PDFs for all photons that reached the ground in the simulations.

Analogous to the investigations of the aerosol effects in Section 6.2, the differences in reflectances resulting from the treatment of the lower boundary conditions by applying a lambertian albedo as

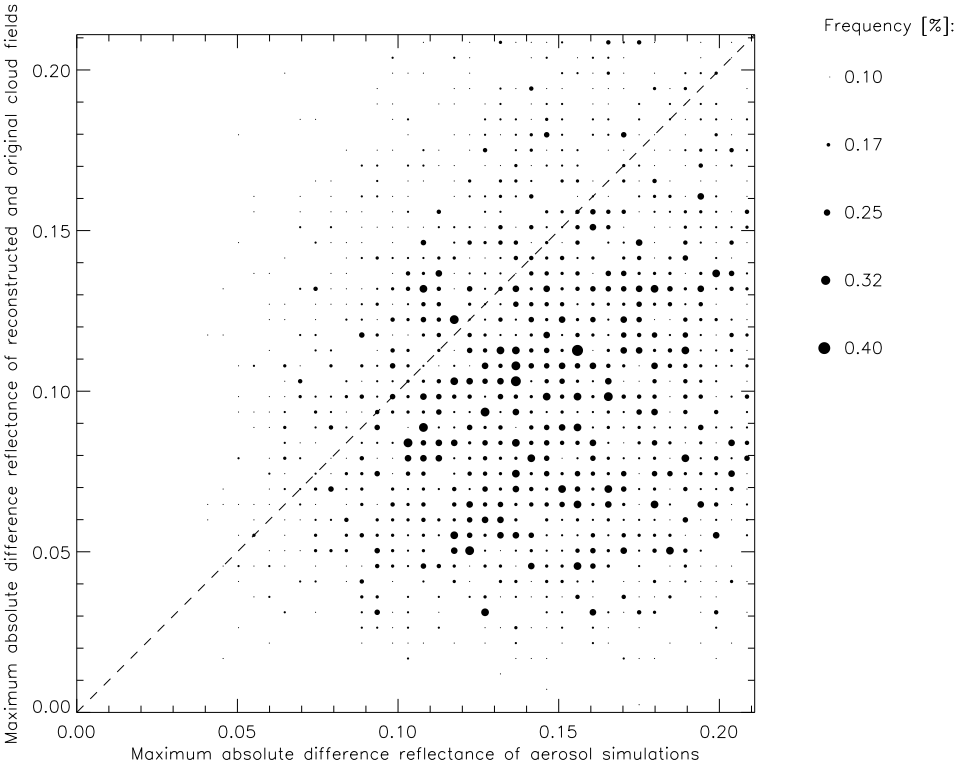

Figure 6.7: Comparison of maximum absolute differences in reflectances due to different aerosol models and maximum absolute differences in reflectances due to inaccurate reconstruction. The differences are clearly biased towards the differences due to varying aerosol models (Cloud field 6, $\theta_0 = 0°$, $\theta = 0°$, $\phi = 0°$).

well as a BRDF were calculated. By visual inspection of the PDFs of reflectance differences for the solar zenith angles and the radiance directions there is no dependency on the illumination and observation geometry found. The differences were also compared to the reflectance differences of the two independent radiative transfer simulations for the original cloud fields. Figure 6.9 represents results found for all cloud fields and geometries indicating differences due to the treatment of the lower boundary conditions not exceeding the Monte Carlo noise.

Results imply that at least for surface conditions with albedos as low as in this example the treatment will not obscure the differences in reflectance due to the reconstruction accuracy and so there seems to be no need for a more sophisticated description of the lower boundary conditions.

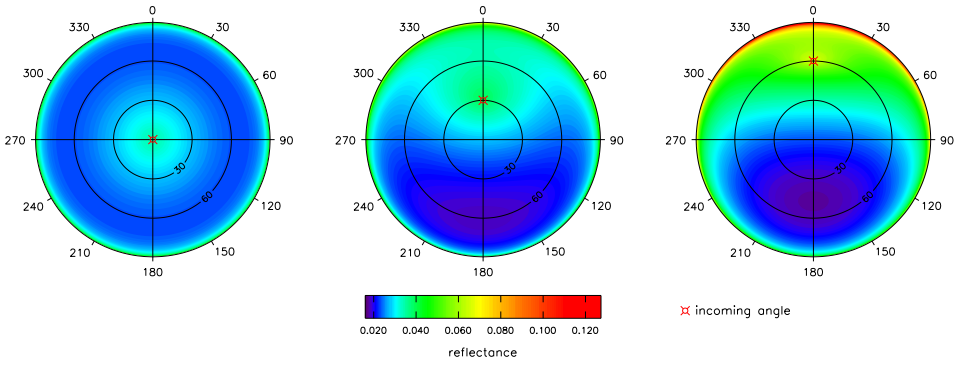

Figure 6.8: Bidirectional reflectance distribution function for pasture land plotted for three illumination angles.

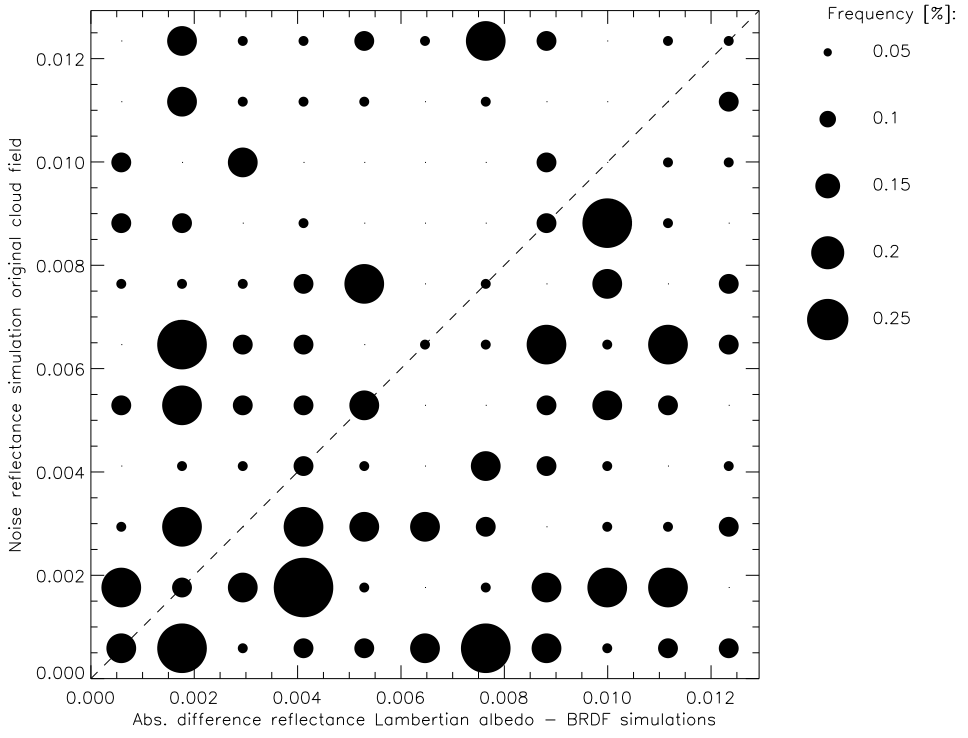

Figure 6.9: Frequency plot of Monte Carlo noise and absolute differences between reflectances of a realization with Lambertian albedo and a realization applying the BRDF (Cloud field 3, $\theta_0 = 30°$, $\theta = 0°$, $\phi = 0°$).

Chapter 7

Conclusions and perspective

In the present study cloud fields were reconstructed from input data as they will become available from future satellite missions. Because three-dimensional cloud fields are not available from measurements surrogate cloud fields have been used to provide the initial cloud fields. Statistics of the surrogate cloud fields were compared with statistics from measured and simulated cloud fields from literature to evaluate the quality of the surrogate fields and reveal particularities. The broad description of these statistics aims furthermore to provide additional constraints that could be involved in reconstruction schemes. The surrogate cloud fields do not capture the variability statistics found for integral parameter like liquid water path and optical depth. Furthermore, their effective radii are found to be exceptionally low. Despite these findings and the restriction of isotropy, the surrogate cloud fields provide valuable substitutions for measured three-dimensional cloud fields.

Several reconstruction schemes with varying complexity tailored for the special geometry of the input data were developed. All schemes assume that measurements of the same parameter by more than one sensor like cloud-top height or optical depth are in agreement. This will not be the case for real measurements and future algorithms may use the discrepancies to deduce further information about the cloud field or will at least have to take the discrepancies into account. All of the schemes are due to the inherent iterative routines applying complete Mie routines to derive optical properties extraordinary time consuming and therefore not applicable in real-time. The employment of these schemes shows that the implementation of additional constraints will lengthen the execution time or will even prevent the algorithm to find a solution within the given constraints. For advanced reconstruction schemes in future there should be a kind of ranking for the constraints derived from longterm measurements and compiled campaign data of cloud properties. By the aid of these data typical statistics for specific cloud types and cloud fields depending on the atmospheric situation and the climatic region could be detected. The most reliable statistical parameters should serve as constraints for the reconstruction schemes.

Extensive radiative transfer simulations were performed with the original and the reconstructed cloud fields. Though all operational techniques for active and passive sensors apply one-dimensional radiative transfer to retrieve cloud properties, simulations in the present study were done applying a three-dimensional radiative transfer code. This might be inconsistent and this inconsistency is also addressed by Chambers et al. (1997). This inconsistency disappears when it is broken down in a two-fold problem. The first part of the problem deals with the inaccuracy of cloud property retrievals due to the simplified radiative transfer. This is an open problem though there are huge efforts to incorporate three-dimensional effects in retrieval techniques. Several of these studies

showed the differences in retrieved cloud properties and consequently these results may provide a first guess about the inherent error of the reconstructed cloud fields due to these effects. Zinner et al. (2006) presented a technique that accounts for horizontal photon transport between columns to reduce the independent pixel error. Therefore, they applied the Green's function (Marshak et al., 1998), relating the reflectivity fields derived by 3d radiative transfer and the independent pixel approximation in Fourier space, to correct IPA reflectivites for horizontal photon transport and then derive cloud properties by employing 1D methods.

The present study addresses the second part of the problem, the reconstruction of the cloud fields employing cloud properties derived by techniques applying one-dimensional radiative transfer. But the reconstructed cloud fields would in a real-world application be evaluated by their radiation compared to the radiation measured by the satellite radiometer which is a result of three-dimensional radiative transfer. So applying one-dimensional radiative transfer models would simplify the problem in an inappropriate way because it would derive radiation taking only microphysical and optical properties in the respective column into account. So if the radiation would indicate an inaccurate reconstructed column only liquid water content and effective radius profiles of the column would needed to be changed. This would reduce the degrees of freedom but may bias the results. But as long as cloud parameters are derived by one-dimensional radiative transfer, the inconsistency of part one and part two still exists. Initial ideas to tackle this problem has been presented by Marchand and Ackerman (2004). Their algorithm, already been described in the introduction, uses 1D retrievals as a first guess for cloud reconstruction and refines the result by applying 3D radiative transfer simulations. Unfortunately, it becomes not clear how the algorithm takes into account horizontal photon transport between neighbouring columns.

The results of the radiative transfer simulations show that at least with one wavelength in the visible it is not possible to infer the reconstruction quality from radiance results even if additional parameters like photon path properties not known from satellite measurements are used. Performing the analyses described before for additional wavelengths might help to shed on more light on the problem. These wavelengths could also be used to derive additional constraints for the reconstruction scheme when for example the technique to derive effective radius profiles described by Chang and Li (2002) is applied.

The simple scale analysis by regridding the cloud fields revealed some unexpected results. Though the photon transport over column boundaries is reduced relationships were not strengthened and the unexplained portion of the variance remains the same. Hence there seems to be no chance to solve the reconstruction problem by reducing the cloud field resolution.

The influence of the simplified treatment of additional parameter like aerosols and the lower boundary were shown to be of the same order as the Monte Carlo noise. For the aerosols it might be due the profiles where extinction above the cloud layers is low. Other patterns of the aerosol distribution with layers of increased extinction above the clouds may alter the results so that aerosols will not be neglectable. The results of the sensitivity studies with varying surface reflectance functions have to be interpreted bearing the low albedo in mind. For local areas of broken cloud fields with higher surface reflectances different treatment of the lower boundary might result in higher magnitudes.

Summarizing the results it seems to be not possible to evaluate cloud fields reconstructed applying the given database. Hence, there is a need for tackling this problem by other approaches. Recently, theoretical studies (Huang et al., 2008a; Huang et al., 2008b) have shown that reconstructions of 3D LWC fields seems to be possible by applying tomographic methods using microwave radiometer data. Because of the influence of the background radiation, radiometer have to be

ground-based and reconstructed fields will cover a limited area so that no global view will be possible. The high ill-posedness of the tomographic problem could besides applying some assumptions of the retrieval result like smoothness and non-negativity further be reduced by employing data of additional instruments like cloud boundaries from cloud radar (Huang et al., 2008b).

Kollias et al. (2007) mentioned the potential of scanning millimeter-wavelength radars or arrays of them for mapping of 3D cloud fields. Because of the required sensitivity to detect even weak cloud elements, their range will be limited covering small domains (e.g. 20 x 20 km). Three-dimensional cloud reconstruction solely by means of cloud radars still suffer from the problem that the radar signal is not a direct measure of cloud water content. An approach applicable to satellite data proposed here would be the use of tomographic methods to reconstruct 3D extinction fields from MISR data in the visible range. This approach is quite challenging because of some inherent issues. From the first to the ninth camera of MISR, scanning the scene from different directions, it takes 7 minutes. Within this time, there might be a significant evolution of the cloud field. Compared to microwave radiative transfer, the forward model in the visible range, needed to derive extinction fields in an iterative procedure is much more complicated. In order to face this problem Evans (2009) recently suggested to limit the retrieval to situations where the optical depth - reflectance relationships can be approximated by a linear approach. Lateral photon transport results in reflectances not solely determined by the optical properties of the considered column. This problem might be reduced by operating with resolutions where these effects are minimized. Evans (2009) suggested to incorporate these effects by using a strategy like Marchand and Ackerman (2004) where in the first part of the procedure a first guess of a 3D extinction field is derived by applying tomographic methods with 1D radiative transfer forward models and in the second part the retrieval is refined by 3D radiative transfer simulations using the radiation results to adjust somehow the extinction field. Unfortunately, MISR is mounted on the TERRA satellite crossing the equator at 10:30 AM. Additional sensors on this satellite are all passive instruments which might not help to constrain the tomographic problem. Active instruments like CloudSAT and CALIPSO which could provide valuable constraints because of their profile information cross the equator at about 1:30 PM, so that the time spread in-between will prevent from using their data as constraints. Therefore, constraining data could be available solely from ground-based sensors limiting the retrieval to the local scale. Though several potential obstacles have been listed, currently it is not clear how they will influence the retrieval of 3D extinction fields by means of MISR data. Having in mind the reconstruction of 3D cloud fields on a global scale, it would be worth to shed more light on this issue.

List of Figures

1.1 Data pool for cloud field reconstructions . . . 3
1.2 Flowchart of this study . . . 7

2.1 Profiles of liquid water content . . . 13
2.2 Cloud droplet size distributions . . . 16
2.3 Profiles of effective radius . . . 17
2.4 Relative differences in extinction coefficient between the approximation Eq. 2.18 and Mie calculations . . . 20
2.5 Size distributions of a rural aerosol population dependent on ambient humidity . . . 21
2.6 Sketch of the Monte Carlo model . . . 25
2.7 Scattering phase functions for an ensemble of water droplets . . . 27

3.1 Cloud field 1 with original resolution . . . 32
3.2 Cloud field 8 with original resolution . . . 33
3.3 Cloud optical depths of surrogate cloud fields . . . 34
3.4 Combinations of mean LWC and r_e from different data sets . . . 37
3.5 Density of the combinations of LWC and r_e of cloud field 4 . . . 37
3.6 Cumulative PDFs of subadiabaticity of LWC for the surrogate cloud fields . . . 38
3.7 Cumulative PDFs of the subadiabaticity of r_e for the surrogate cloud fields . . . 39
3.8 Profiles of standard deviation of LWC . . . 40
3.9 Cumulative PDFs of extinction coefficient for surrogate cloud fields . . . 40
3.10 PDFs of the LWP . . . 42
3.11 PDFs of cloud optical depth . . . 42

4.1 Sketch of adiabatic profile approximation scheme . . . 46
4.2 Cloud-base approximation scheme . . . 48
4.3 Adjustment of the profiles of LWC and r_e . . . 49
4.4 PDFs of RMSE of extinction coefficient . . . 53
4.5 RMSE of cloud microphysics and optical properties . . . 55

5.1 Ripleys K for the photon patterns of different realizations . . . 58
5.2 PDFs of photon penetration depth . . . 59
5.3 Scatterplot of RMSE of extinction coefficient and RMSE of the PDF of geometrical pathlength . . . 63
5.4 Profiles of mean and standard deviation of geometrical pathlength . . . 64
5.5 PDFs of scaled geometrical and optical pathlengths of cloud field 3 . . . 66

5.6 Probability distribution functions of scaled geometrical and optical pathlengths of cloud field 7 . . . 67
5.7 Dependence of correlation of the RMSE of the geometrical pathlength PDF on the homogeneity . . . 68
5.8 Comparison of pathlengths correlations, inhomogeneity parameter χ and slope of 1D power spectrum of optical depth . . . 68
5.9 Comparison of Monte Carlo noise and the minimum of the absolute reflectance differences of cloudy columns . . . 69
5.10 Comparison of Monte Carlo noise and the maximum of the absolute reflectance differences of cloudy columns . . . 70
5.11 PDFs of the absolute differences in reflectance between realizations for reconstructed and original cloud fields . . . 70
5.12 PDFs of scaled absolute differences in reflectance between realizations for reconstructed and original cloud fields . . . 71
5.13 Cloud shadow situations . . . 72
5.14 Classification results of the ranking of absolute reflectance differences and absolute differences in optical depth . . . 75
5.15 Profiles of the penetration depth of photons and the resulting weighting functions . 76
5.16 Sketch of path reconstruction scheme . . . 78

6.1 Cloud field 1 with reduced horizontal resolution . . . 81
6.2 Cloud field 8 with reduced horizontal resolution . . . 82
6.3 PDFs of scaled geometrical and optical pathlength in cloud for regridded cloud field 3 82
6.4 Microphysical and optical properties of profiles of wet and dry aerosol populations 85
6.5 Comparison of maximum absolute differences in reflectances due to different aerosol models and Monte Carlo noise . . . 87
6.6 Comparison of maximum absolute differences in reflectances due to different aerosol models and maximum absolute differences due to Monte Carlo noise . . . 88
6.7 Comparison of maximum absolute differences in reflectances due to different aerosol models and maximum absolute differences in reflectances due to inaccurate reconstruction . . . 89
6.8 BRDF for pasture land . . . 90
6.9 Frequency plot of Monte Carlo noise and absolute differences due to surface reflection 90

List of Tables

3.1 Cloud-top, cloud-base and cloud layer statistics 35
3.2 Cloud fraction for different perspectives 36
3.3 Liquid water path statistics 41
3.4 Cloud optical depth statistics 43

4.1 Differences in cloud geometrical thickness 52
4.2 Differences in cloud liquid water path [gm^{-2}] 53
4.3 Synopsis of microphysical and optical properties reconstruction quality 54

5.1 Parameters of radiative transfer simulations 57
5.2 L2, JM and KS for PDFs of global penetration depth 60
5.3 L2, JM and KS for PDFs of global geometrical pathlength 62
5.4 RMSE of mean geometrical pathlength sorted by the penetration depth 65
5.5 Subsets of cloudy columns 73

6.1 Microphysical parameters of aerosol models 84

Acronyms

4D-CLOUDS	Project to study clouds in 4 dimensions
AirMISR	aircraft mounted version of MISR
AP	Adiabatic Profile Reconstruction
AVHRR	Advanced Very High Resolution Radiometer
BBC	Baltex Bridge Campaign
BRDF	Bidirectional Reflectance Distribution Function
CALIPSO	Cloud-Aerosol Lidar and Infrared Pathfinder Satellite Observations
CCN	Cloud Condensation Nuclei
CLIWA-NET	Cloud Liquid Water Network
CloudSat	Satellite of the Earth Observing System (EOS)
CRM	Cloud Resolving Model
ECHAM 5	Global Climate Model of the Max Planck Institute Hamburg Version 5
FSSP	Fourier Scattering Spectrometer Probe
IFM Geomar	Institut für Meereskunde Forschungszentrum für Marine Geowissenschaften
IAAFT	Iterative Amplitude Adapted Fourier Transformation
IPA	Independent Pixel Approximation
IPCC	International Panel on Climate Change
IPT	Integrated Profiling Technique
LES	Large-Eddy Simulation
LM	Lokalmodell
LWC	Liquid Water Content
LWC_{ad}	adiabatic liquid water content
LWP	Liquid Water Path
mc	maritime aerosol model with continental background
MCUnik	Monte Carlo model University of Kiel
MISR	Multiangle Imaging Spectroradiometer
MODIS	Moderate Resolution Imaging Spectroradiometer
NIR	near-infrared
NOAA	National Oceanic and Atmospheric Administration
PDF	Probability Distribution Function
PVM	Particle Volume Monitor
REMO	Regional Model
RMSE	Root-Mean-Squared Error
RTE	Radiative Transfer Equation
ru	rural aerosol model
SHDOM	Spherical Harmonics Discrete Ordinate Method
SITCOM	Spectral Idealized Thermodynamically Consistent Model
TERRA	Satellite of the Earth Observing System (EOS)
TIPA	Tilted Independent Pixel Approximation

tr	tropospheric aerosol model
UV	ultraviolet
WRA	Well Reconstructed Area

Symbols

3d	subscript for reflectances calculated by 3d radiative transfer simulations	[-]
α	distribution shape parameter of gamma distribution	[-]
β	slope of power spectrum	[-]
β_{1d}	slope of 1d power spectrum	[-]
β_{2d}	slope of 2d power spectrum	[-]
β_{qd}	slope of q-dimensional power spectrum	[-]
β_a	absorption coefficient	$[km^{-1}]$
β_{ad}	vertical gradient of liquid water	$[gkg^{-1}m^{-1}]$
β_{cld}	Cloud extinction coefficient	$[km^{-1}]$
β_e	extinction coefficient	$[km^{-1}]$
$\beta_e(s')$	extinction coefficient at position s'	$[km^{-1}]$
β_{ea}	Aerosol extinction coefficient	$[km^{-1}]$
β_{er}	Rayleigh extinction coefficient	$[km^{-1}]$
β_{em}	Mie extinction coefficient	$[km^{-1}]$
β_s	scattering coefficient	$[km^{-1}]$
β_{sa}	Aerosol scattering coefficient	$[km^{-1}]$
β_{sr}	Rayleigh scattering coefficient	$[km^{-1}]$
β_{sm}	Mie scattering coefficient	$[km^{-1}]$
Γ	gamma function	[-]
Γ'	rate of LWC increase with height	$[gm^{-3}m^{-1}]$
γ	adjustable parameter of gamma distribution	[-]
	parameter of Rayleigh scattering phase function	[-]
δ	optical depth	[-]
η	smoothing scale	[m]
θ	zenith angle of scattered radiation	[°]
θ_0	zenith angle of incident radiation	[°]
λ	wavelength	$[\mu m]$
Ξ	normalized redistribution function	[-]
ρ_w	density of liquid water	$[kgm^{-3}]$
ρ_n	depolarization factor	[-]
$\rho(\theta, \phi)$	reflectance in scattering direction (θ, ϕ)	[-]
σ	standard geometrical deviation of r	$[\mu m]$
σ_λ	Rayleigh scattering cross section for wavelength λ	$[m^{-2}]$
ς	reflectance contribution of scattering event	[-]
Φ	radiant flux	[W]

ϕ_0	azimuth angle of scattered radiation	[rad]
ϕ	azimuth angle of scattered radiation	[rad]
χ	size parameter	[-]
	inhomogeneity parameter	[-]
ω	solid angle	$[sr]$
$\tilde{\omega}$	single scattering albedo	[-]
A	surface	$[m^{-2}]$
	region of interest	[-]
a	concentration parameter of gamma distribution	$[m^{-3}\mu m^{-1-\alpha}]$
a	albedo	[-]
	considered parameter	[-]
a_{bs}	Black-sky albedo	[-]
asym	subscript for reflectances calculated by asymptotic radiative transfer approximation	[-]
a_{ws}	White-sky albedo	[-]
B	Planck function	$[Wm^{-2}sr^{-1}\mu m{-}1]$
b	size parameter of gamma distribution	$[\mu m^{-1}]$
C_p	specific heat of air at constant pressure	$[JK^{-1}kg^{-1}]$
cb	cloud-base	[m]
ct	cloud-top	[m]
D	droplet diameter	[mm]
$dLWC(z)$	deviation of LWC in height z	$[gm^{-3}]$
$dr_e(z)$	deviation of r_e in height z	$[\mu m]$
d_{orig}	parameter value of original cloud field	[-]
d_{rec}	parameter value of reconstructed cloud field	[-]
dz	geometrical thickness	[km]
$E(k)$	power spectrum for wavenumber k	[-]
E_s	saturation vapour pressure	[kPa]
F	irradiance	$[Wm^{-2}]$
$F^{\downarrow}$	downward irradiance	$[Wm^{-2}]$
$F(k)$	Fourier coefficient for wavenumber k	[-]
f_n	n^{th} value of spatial or time series	[-]
$f(\cdot)$	frequency of occurrence	[-]
g	gravitational acceleration	$[ms^{-2}]$
	asymmetry parameter of scattering phase function	[-]
$g(\cdot)$	frequency of occurrence	[-]
H_p	scale height	[m]

$h_{abs}(\delta = 2)$	absolute height of 2 optical depth from cloud-top	[km]
$h_{rel}(\delta = 2)$	relative height of 2 optical depth from cloud-top	[-]
I_t	number of photons in bin t	[-]
i	index variable	[-]
	imaginary unit	[-]
JM	Jeffries-Matusita distance	[-]
j	index variable	[-]
KS	Kolmogorov-Smirnov distance	[-]
$K(t)$	Ripleys K parameter for distance bin t	[-]
L	latent heat of condensation	$[Jkg^{-1}]$
	radiance	$[Wm^{-2}sr^{-1}]$
L2	Euclidian distance	[-]
LWC	liquid water content	$[gm^{-3}]$
LWC_{ad}	adiabatic liquid water content	$[gm^{-3}]$
$LWC_i(z)$	LWC in height z of reference column	$[gm^{-3}]$
$LWC_{max}(z)$	maximum LWC in height z	$[gm^{-3}]$
$LWC_{min}(z)$	minimum LWC in height z	$[gm^{-3}]$
k	wavenumber	$[m^{-1}]$
N	number of volumes of equal size	[-]
	number of measurements in spatial or time series	[-]
	number of bins of histogram	[-]
N_d	number density	$[m^{-3}]$
N_s	molecular number density	$[cm^{-3}]$
n	number of photons	[-]
	refractive index of homogeneous sphere	[-]
$n(r)$	number of droplets with radius r	$[m^{-3}\mu m^{-1}]$
n_s	refractive index for standard air	[-]
n_w	refractive index for water	[-]
n_0	refractive index for dry aerosol	[-]
orig	subscript for reflectances calculated for original cloud fields	[-]
P	pressure	[kPa]
$P(\cdot)$	probability	[-]
$p(cos\theta)$	phase function value for scattering angle $cos\theta$	$[sr^{-1}]$
$p_a(cos\theta)$	Aerosol phase function value for scattering angle $cos\theta$	$[sr^{-1}]$
$p_m(cos\theta)$	Mie phase function value for scattering angle $cos\theta$	$[sr^{-1}]$

$p_r(cos\theta)$	Rayleigh phase function value for scattering angle $cos\theta$	$[sr^{-1}]$
$Q_e(r)$	Extinction efficiency	[-]
$Q_s(r)$	Scattering efficiency	[-]
q	number of dimensions	[-]
q_{LWC}	scaling coefficient for LWC	[-]
q_{r_e}	scaling coefficient for r_e	[-]
R_m	gas constant of moist air	$[JK^{-1}kg^{-1}]$
$R(\theta_0, \theta, \phi, \lambda)$	Reflection function	[-]
R_v	gas constant of water vapour	$[JK^{-1}kg^{-1}]$
r_m	geometrical mean of drop radius	$[\mu m]$
r	radius	$[\mu m]$
r_{a_w}	radius of swollen particle	$[\mu m]$
r_e	effective radius	$[\mu m]$
$r_{e,i}(z)$	effective radius in height z of reference column	$[\mu m]$
$r_{e,max}(z)$	maximum effective radius in height z	$[\mu m]$
$r_{e,min}(z)$	minimum effective radius in height z	$[\mu m]$
rec	subscript for reflectances calculated for reconstructed cloud fields	[-]
ref	reflectance	[-]
rh_t	threshold of relative humidity	[%]
r_0	radius of dry aerosol	$[\mu m]$
S_0	solar irradiance	$[Wm^{-2}]$
s, s_0, s_1, s_2	positions in space	[-]
scaled_ref	scaled reflectance	[-]
T	temperature	[°C]
t	distance bin	$[km^{-1}]$
u	euclidian distance	[km]
V	volume	$[cm^{-3}]$
w	weighting factor	[-]
x,y	relative positions in space	[km]
Z	radar reflectivity factor	$[mm^6m^{-3}]$
z	height	[m]

Bibliography

[1] Albrecht, B.A. (1989) Aerosols, cloud microphysics, and fractional cloudiness. Science, 245, 1227-1230.

[2] Andrews, E., Sheridan, P., Ogren, J., and Ferrare, R. (2004) In situ aerosol profiles over the Southern Great Plains cloud and radiation test bed site: 1. Aerosol optical properties. Journal of Geophysical Research, 109, D06208, doi:10.1029/2003JD004025.

[3] Antyufeev, V.S. (1996) Solution of the generalized transport equation with a peak-shaped indicatrix by the Monte Carlo method. Russian Journal of Numerical Analysis and Mathematical Modelling, 11, 113-137.

[4] Arends, B.G., Kos, G.P.A., Maser, R., Schell, D., Wobrock, W., Winkler, P., Ogren, J.A., Noone, K.J., Hallberg, A., Svenningsson, I.B., Wiedensohler, A., Hansson, H.C., Berner, A., Solly, I., and Kruisz, C. (1994) Microphysics of Clouds at Kleiner Feldberg. Journal of Atmospheric Chemistry, 19, 59-85.

[5] Arking, A. and Childs, J.D. (1985) Retrieval of Cloud Cover Parameters from Multispectral Satellite Images. Journal of Climate and Applied Meteorology, 24, 322-333.

[6] Austin, R.T., England, A.W., and Wakefield, G.H. (1994) Special Problems in the Estimation of Power-Law Spectra as Applied to Topographical Modeling. IEEE Transactions on Geoscience and Remote Sensing, 32, 928-939.

[7] Austin, P.H., Baker, M.B., Blyth, A.M., and Jensen, J.B. (1995) Small-Scale Variability in Warm Continental Cumulus Clouds. Journal of the Atmospheric Sciences, 42, 1123-1138.

[8] Baker, M.B., Corbin, R.G., and Latham, J. (1980) The influence of entrainment on the evolution of cloud droplet spectra: I. A model of inhomogeneous mixing. Quarterly Journal of the Royal Meteorological Society, 106, 581-598.

[9] Barker, H.W. and Davies, J.A. (1992) Solar Radiative Fluxes for Stochastic, Scale-invariant Broken Cloud Fields. Journal of the Atmospheric Sciences, 49, 1115-1126.

[10] Barker, H.W., Goldstein, R.K., and Stevens, D.E. (2003) Monte Carlo Simulation of Solar Reflectances for Cloudy Atmospheres. Journal of the Atmospheric Sciences, 60, 1881-1894.

[11] Barker, H.W., Pavloski, C.F., Ovtchinnkov, M., and Clothiaux, E.E. (2004) Assessing a Cloud Optical Depth Retrieval Algorithm with Model-Generated Data and the Frozen Turbulence Assumption. Journal of the Atmospheric Sciences, 61, 2951-2956.

[12] Barker, H.W., Wielicki, B.A., and Parker, L. (1996) A Parametrization for Computing Grid-Averaged Solar Fluxes for Inhomogeneous Marine Boundary Layer Clouds. Part II: Validation Using Satellite Data. Journal of the Atmospheric Sciences, 53, 2304-2316.

[13] Baum, B.A., Uttal, T., Poellot, M., Ackerman, T.P., Alvarez, J.M., Intrieri, J., Starr, D.O'C., Titlow, J., Tovinkere, V., and Clothiaux E.E. (1995) Satellite remote sensing of multiple cloud layers. Journal of the Atmospheric Sciences, 52, 4210-4230.

[14] Beaulieu, A., Goanac'h, H., and Lovejoy, S. (2007) Anisotropic scaling of remotely sensed drainage basins: the differential anisotropic scaling technique. Nonlinear Processes in Geophysics, 14, 337-350.

[15] Berendes, T., Sengupta, S.K., Welch, R.M, Wielicki, B.A., and Navar, M. (1992) Cumulus Cloud Base Height Estimation from High Spatial Resolution Landsat Data: A Hough Transform Approach. IEEE Transactions on Geoscience and Remote Sensing. 30, 3, 430-443.

[16] Blyth, A.M. (1993) Entrainment in Cumulus Clouds. Journal of Applied Meteorology, 32, 4, 626-641.

[17] Boers, R. and Rotstayn, L.D. (2001) Possible links between cloud optical depth and effective radius in remote sensing observations. Quarterly Journal of the Royal Meteorological Society, 127, 2367-2383.

[18] Bower, K.N., Choularton, T.W., Latham, J., Nelsen, J., Baker, M.B., and Jensen, J. (1994) A Parametrization of Warm Clouds for Use in Atmospheric General Circulation Models. Journal of the Atmospheric Sciences, 51, 2722-2732.

[19] Brenguier, J.L., Pawlowska, H., Schüller, L., Preusker, R., Fischer, J. and Fouquart, Y. (2000) Radiative properties of Boundary Layer Clouds: Droplet Effective Radius versus Number Concentration. Journal of the Atmospheric Sciences, 57, 803-821.

[20] Brenguier, J.L., Pawlowska, H., and Schüller, L. (2003) Cloud microphysical and radiative properties for parameterization and satellite monitoring of the indirect effect of aerosol on climate. Journal of Geophysical Research, 108, 8632, doi:10.1029/2002JD002682.

[21] Bucholtz, A. (1995) Rayleigh-scattering calculations for the terrestrial atmosphere. Applied Optics, 34, 15, 2765-2773.

[22] Cahalan, R.F., Oreopoulos, L., Marshak, A., Evans, K.F., Davis, A.B., Pincus, R., Yetzer, K.H., Mayer, B., Davies, R., Ackerman, T.P., Barker, H.W., Clothiaux, E.E., Ellingson, R.G., Garay, M.J., Kassaniov, E., Kinne, S., Macke, A., O'Hirok, W., Partain, P.T., Prigarin, S.M., Rublev, A.N., Stephens, G.L., Szcap, F., Takara, E.E., Várnai, T., Wen, G., and Zhuravleva, T.B. (2005) The I3RC. - Bringing Together the Most Advanced Radiative Transfer Tools for Cloudy Atmospheres. Bulletin of the American Meteorological Society, 86, 1275-1293.

[23] Cahalan, R.F., Ridgeway, W., and Wiscombe, W.J. (1994a) Independent pixel and Monte Carlo Estimate of stratocumulus clouds. Journal of Atmospheric Sciences, 51, 3776-3790.

[24] Cahalan, R,F., Ridgeway, W., Wiscombe, W.J., Bell, T.L., and Snider, J.B. (1994b) The albedo of fractal stratocumulus clouds. Journal of Atmospheric Sciences, 53, 2434-2455.

[25] Cahalan, R.F. and Snider, J.B. (1989) Marine stratocumulus structure. Remote Sensing of Environment, 28, 95-107.

[26] Chambers, L.H., Wielicki, B.A., and Evans, K.F. (1997) Independent Pixel and Two-Dimensional Estimates of Landsat-Derived Cloud Field Albedo. Journal of the Atmospheric Sciences, 54, 1525-1532.

[27] Chandrasekhar, S. (1950) Radiative transfer. Clarendon Pr., Oxford, 393 pp.

[28] Chang, F.L. and Li, Z. (2002) Estimating the vertical variation of cloud droplet effective radius using multispectral near-infrared satellite measurements. Journal of Geophysical Research, 107, D15, doi:10.1029/2001JD000766.

[29] Chang, F.L. and Li, Z. (2005) A Near-Global Climatology of Single-Layer and Overlapped Clouds and Their Optical Properties Retrieved from Terra/MODIS Data Using a New Algorithm. Journal of Climate, 18, 4752-4771.

[30] Chin, H.N.S., Rodriguez, D.J., Cederwall, R.T., Chuang, C.C., Grossmann, A.S., Yio, J.J., Fu, Q., and Miller, M.A. (2000) A microphysical retrieval Scheme for Continental Low-Level Stratiform Clouds: Impacts of the Subadiabatic Character on Microphysical Properties and the Radiation Budgets. Monthly Weather Review, 128, 2511-2527.

[31] Chlond, A. and Wolkau, A. (2000) Large-eddy simulation of a nocturnal stratocumulus-topped marine atmospheric boundary layer: an uncertainty analysis. Boundary-Layer Meteorology, 95, 31-55.

[32] Coley, P.F. and Jonas, P.R. (1996) The influence of cloud structure and droplet concentration on the reflectance of shortwave radiation. Annales Geophysicae, 14, 845-852.

[33] Coley, P.F. and Jonas, P.R. (1997) The contribution of cloud inhomogeneities and droplet concentration to the albedo of broken-cloud fields. Quarterly Journal of the Royal Meteorological Society, 123, 1931-1944.

[34] Considine, G., Curry, J.A., and Wielicki, B. (1997) Modeling cloud fraction and horizontal varaibility in marine boundary layer clouds. Journal of Geophysical Research, 102, 13517-13525.

[35] Crewell, S., Simmer, C., Löhnert, U., Venema, V., Feijt, A., van Meijgaard, E., van Lammeren, A., Bloemink, H., Joliet, D., Wendisch, M., Schmidt, S., Schröder, M., Willen, U., Quante, M., Meywerk, J., Krasnov, O.A., Trautmann, T., Garcia, S.G., Pfeilsticker, K., and Scholl, T. (2004) The BALTEX Bridge Campaign. An integrated approach for a better understanding of clouds. Bulletin of the American Meteorological Society, 85, 1565-1584.

[36] Damiano, P. and Chýlek, P. (1994) Shortwave Radiative Properties of Clouds: Numerical Study. Journal of the Atmospheric Sciences, 51, 1223-1233.

[37] Deirmendjian, A. (1969) Electromagnetic scattering on spherical polydispersions. Elsevier, Amsterdam, 260 pp.

[38] Dim, J.R., Takamura, T., Okada, I., Nakajima, T.Y., and Takenaka, H. (2007) Influence of inhomogeneous cloud fields on optical properties retrieved from satellite observations. Journal of Geophysical Research, 112, D13202, doi:10.1029/2006JD007891.

[39] Dong, X. and Mace, G.G. (2003) Profiles of Low-Level Stratus Clod Microphysics Deduced from Ground-Based Measurements. Journal of Atmospheric and Oceanic Technology, 20, 42-53.

[40] Duda, D.P., Stephens, G.L., Stevens, B., and Cotton, W.R. (1996) Effects of Aerosol and Horizontal Inhomogeneity on the Broadband Albedo of Marine Stratus: Numerical Simulations. Journal of the Atmospheric Sciences, 53, 3757-3769.

[41] Evans, K.F. (1998) The Spherical Harmonics Discrete Ordinate Method for Three-Dimensional Atmospheric Radiative Transfer. Journal of the Atmospheric Sciences, 55, 429-446.

[42] Evans, K.F. (2009) personal communications.

[43] Evans, K.F. and Wiscombe, W.J. (2004) An algorithm for generating stochastic cloud fields from radar profile statistics. Atmospheric Research, 72, 263-289.

[44] Evans, K.F., Marshak, A., and Várnai, T. (2008) The Potential for Improved Boundary Layer Cloud Optical Depth Retrievals from the Multiple Directions of MISR. Journal of the Atmospheric Sciences, 65, 3179-3196.

[45] Fleishauer, R.P., Larson, V.E., and Vonder Haar, T.H. (2002) Observed Microphysical Structure of Midlevel, Mixed-Phase Clouds. Journal of the Atmospheric Sciences, 59, 1779-1804.

[46] Fomin B.A. and Mazin I.P. (1998) Model for an investigation of radiative transfer in cloudy atmosphere. Atmospheric Research, 47-48, 127-153.

[47] Forsythe, J.M., Vonder Harr, T.H., and Reinke, D.L. (2000) Cloud-Base Estimates Using a Combination of Meteorological Satellite Imagery and Surface Reports. Journal of Applied Meteorology, 39, 2336-2347.

[48] Fox, N.I. and Illingworth, A.J. (1997) The retrieval of stratocumulus cloud properties by ground-based cloud radar. Journal of Applied Meteorology, 36, 485-492.

[49] Frisch, A.S., Fairall, C.W., and Snider, J.B. (1995) Measurement of Stratus Cloud and Drizzle Parameters in ASTEX with a K_{α}-Band Doppler Radar and a Microwave Radiometer. Journal of the Atmospheric Sciences, 52, 2788-2799.

[50] Frisch, A.S., Shupe, M.D., Djalalova, I., Feingold, G., and Poellot, M.R. (2002) The Retrieval of Stratus Cloud Droplet Effective Radius with Cloud Radars. Journal of Atmospheric and Oceanic Technology, 19, 835-842.

[51] Giraud, V., Thouron, O., Riedi, J., and Goloub, P. (2001) Analysis of direct comparison of cloud top temperature and infrared split window signature against independent retrievals of cloud thermodynamic phase. Geophysical Research Letters, 28, 983-986.

[52] Di Guiseppe, F. and Tompkins, A.M. (2003) Effect of Spatial Organization on Solar Radiative Transfer in Three-Dimensional Idealized Stratocumulus Cloud Fields. Journal of Atmospheric Sciences, 60, 1774-1794.

[53] Gultepe, I., Isaac, G.A., Leaitch, W.R., and Banic, C.M. (1996) Parametrizations of marine stratus microphysics based on in situ observations: Implications for GCMs. Journal of Climate, 9, 345-357.

[54] Haase, P. (1995) Spatial pattern analysis in ecology based on Ripleys's K-function: Introduction and methods of edge correction. Journal of Vegetation Science, 6, 575-585.

[55] Hänel, G. (1976) The properties of atmospheric aerosol particles as functions of the relative humidity at thermodynamic equilibrium with the surrounding moist air. Advances in Geophysics, 19, 73-188.

[56] Hansen, J.E. and Travis, L.D. (1974) Light scattering in planetary atmospheres. Space Science Reviews, 16, 527-610.

[57] Harshvardhan, Guo, G., Green, R.N., Qu, Z., and Nakajima, T.Y. (2004) Remotely Sensed Microphysical and Thermodynamic Properties of Nonuniform Water Cloud Fields. Journal of the Atmospheric Sciences, 61, 2574-2587.

[58] Hinkelman, L.M., Stevens, B., and Evans, K.F. (2005) A Large-Eddy Simulation Study od Anisotropy in Fair-Weather Cumulus Cloud Fields. Journal of Atmospheric Sciences, 62, 2155-2171.

[59] Hu, Y.X. and Stamnes, K. (1993) An accurate parametrization of the radiative properties of water clouds suitable for use in climate models. Journal of Climate, 6, 728-742.

[60] Huang, D., Liu, Y., and Wiscombe, W. (2008a) Determination of cloud liquid water distribution using 3D cloud tomography. Journal of Geophysical Research, 113, D13201, doi:10.1029/2007JD009133.

[61] Huang, D., Liu, Y., and Wiscombe, W. (2008b) Cloud tomography: Role of constraints and a new algorithm. Journal of Geophysical Research, 113, D23203, doi:10.1029/2008JD009952.

[62] Hudson, J.G. and Yum, S.S. (2001) Maritime-Continental Drizzle Contrasts in Small Cumuli. Journal of the Atmospheric Sciences, 58, 915-926.

[63] Hutchison, K.D (2002) The retrieval of cloud base heights from MODIS and three-dimensional cloud fields from NASA's EOS Aqua mission. International Journal of Remote Sensing, 23, 5249-5265.

[64] Hozumi, K., Harimaya, T., and Magono, C. (1982) The Size distribution of Cumulus Clouds as a Function of Cloud Amount. Journal of the Meteorological Society of Japan, 60, 691-699.

[65] Iwabuchi, H. (2006) Efficient Monte Carlo Methods for Radiative Transfer Modeling. Journal of the Atmospheric Sciences, 63, 2324-2339.

[66] Iwabuchi, H. and Hayasaka, T. (2002) Effects of Cloud Horizontal Inhomogeneity on the Optical Thickness Retrieved from Moderate-Resolution Satellite Data. Journal of the Atmospheric Sciences, 59, 2227-2242.

[67] Jaenicke, R. (1993) Tropospheric aerosols., in: Aerosol-Cloud-Climate Interactions. edited by P.V. Hobbs, Academic Press, New York, pp 1-31.

[68] Karstens, U., Simmer, C., and Ruprecht, E. (1994) Remote Sensing of Cloud Liquid Water. Meteorology and Atmospheric Physics, 54, 157-171.

[69] Khairoutdinov, M.F. and Kogan, Y.L. (1999) A Large Eddy Simulation Model with Explicit Microphysics: Validation against Aircraft Observations of a Stratocumulus-Topped Boundary Layer. Journal of the Atmospheric Sciences, 56, 2115-2131.

[70] Khrgian, A.H. and Mazin, I.P. (1952) On droplet size distribution in clouds. Transactions of Central Aerological Observatory Moscow, 7, 56-61.

[71] Kim, B.G., Klein, S.A., and Norris, J.R. (2005) Continental liquid water cloud variability and its parametrization using Atmospheric Radiation Measurement data. Journal of Geophysical Research, 110, D15S08, doi:10.1029/2004JD005122.

[72] Kokhanovsky, A.A. (2004a) Optical properties of terrestrial clouds. Earth-Science Reviews, 64, 189-241.

[73] Kokhanovsky, A.A. (2004b) The Depth of Sunlight Penetration in Cloud Fields for Remote Sensing. IEEE Geoscience and Remote Sensing Letters, 1, 242-245.

[74] Kokhanovsky, A.A., Rozanov, V.V., Zege, E.P., Bovensmann, H., and Burrows, J.P. (2003) A semianalytical cloud retrieval algorithm using backscattered radiation in 0.2-2.4 μm spectral region. Journal of Geophysical Research, 108, 4008, doi:10.1029/2001JD001543.

[75] Kollias, P., Clothiaux, E.E., Miller, M.A., Albrecht, B.A., Stephens, G.L., and Ackerman, T.P. (2007) Millimeter-Wavelength Radars: New Frontier in Atmospheric Cloud and Precipitation Research. Bulletin of the American Meteorological Society, 88, 1608–1624.

[76] Korolev, A.V. (1993) On the formation of non-adiabatic LWC profile in stratiform clouds. Atmospheric Research, 29, 129-134.

[77] Korolev, A.V., Isaac, G.A., Mazin, I.P., and Barker, H.W. (2001) Microphysical properties of continental clouds from in-situ measurements. Quarterly Journal of the Royal Meteorological Society, 127, 2117-2151.

[78] Korolev, A.V. and Mazin, I.P. (1993) Zones of Increased and Decreased Droplet Concentration in Stratiform Clouds. Journal of Applied Meteorology, 32, 760-773.

[79] Lenoble, J. (1993) Atmospheric Radiative Transfer. Deepak, Hampton, 532 pp.

[80] Lenoble, J. and Brogniez, C. (1984) A Comparative Review of Radiation Aerosol Models. Contributions to Atmospheric Physics, 57, 1-20.

[81] Li, J., Geldart, J.W., and Chýlek, P. (1994) Solar radiative transfer in clouds with vertical inhomogeneity. Journal of the Atmospheric Sciences, 51, 2542-2552.

[82] Liou, K.N. (1992) Radiation and Cloud Processes in the Atmosphere. Oxford University Press, Oxford, 487 pp.

[83] Liou, K.N., Ou, S.C., Takano, Y., Roskovensky, J., Mace, G.G., Sassen, K., and Poellot, M. (2002) Remote sensing of three-dimensional inhomogeneous cirrus clouds using satellite and mm-wave cloud radar data. Geophysical Research Letters, 29, 9, doi:10.1029/2002GL014846.

[84] Liu, Y., Daum, P.H., and Hallet, J. (2002) A Generalized Systems Theory for the Effect of Varying Fluctuations on Cloud Droplet Size Distributions. Journal of the Atmospheric Sciences, 59, 2279-2290.

[85] Loeb, N.G., Várnai, T., and Winker, D.M. (1998) Influence of subpixel-scale cloud-top structure on reflectances from overcast stratiform cloud layers. Journal of the Atmospheric Sciences, 55, 2960-2973.

[86] Löhnert, U., Crewell, S., and Simmer, C. (2004) An integrated approach toward retrieving physically consistent profiles of temperature, humidity and cloud liquid water. Journal of Applied Meteorology, 43, 1295-1307.

[87] Lucht, W., Schaaf, C.B., and Strahler, A.H. (2000) An Algorithm for the Retrieval of Albedo from Space Using Semiempirical BRDF Models. IEEE Transactions on Geoscience and Remote Sensing, 38, 977-998.

[88] Macke, A., Mitchell, D., and von Bremen, L. (1999) Monte Carlo radiative transfer calculations for inhomogeneous mixed phase clouds. Physics and Chemistry of the Earth(B), 24, 237-241.

[89] Malinowski, S.P. and Zawadzki, I. (1993) On the Surfaces of Clouds. Journal of the Atmospheric Sciences, 50, 5-13.

[90] Manly, B.F.J. (1996) Randomization, Bootstrap and Monte Carlo Methods in Biology. Chapman & Hall, Boca Raton, 480 pp.

[91] Marchand, R. and Ackerman. T. (2004) Evaluation of radiometric measurements from the NASA Multiangle Imaging Spectroradiometer (MISR): Two- and threedimensional radiative transfer modeling of an inhomogeneous stratocumulus cloud deck. Journal of Geophysical Research., 109, D18208, doi:10.1029/2004JD004710.

[92] Marchuk, G.I., Mikhailov, G.A., Nazaraliev, M.A., Darbinjan, R.A., Kargin, B.A., and Elepov, B.S. (1980) The Monte Carlo Methods in Atmospheric Optics. Springer, Berlin, 208 pp.

[93] Marshak, A., Davis, A., Wiscombe, W., and Cahalan, R.F. (1995) Radiative smoothing in fractal clouds. Journal of Geophysical Research, 100, 26247-26261.

[94] Marshak, A., Davis, A., Cahalan, R.F., and Wiscombe, W. (1998) Nonlocal independent pixel approximation: Direct and inverse problems. IEEE Transactions on Geoscience and Remote Sensing, 36, 192-204.

[95] Marshak, A., Platnick, S., Várnai, T., Wen, G., and Cahalan, R.F. (2006) Impact of threedimensional radiative effects on satellite retrievals of cloud droplet sizes. Journal of Geophysical Research, 111, D09207, doi: 10.1029/2005JD006686.

[96] Menon, S. (2004) Current Uncertainties in Assessing Aerosol Effects on Climate. Annual Review of Environment and Resources, 29, 1-30.

[97] Menzel, W.P., Smith, W.L., and Stewart, T.R. (1983) Improved cloud motion wind vector and height assignment using VAS. Journal of Climate and Applied Meteorology, 22, 377-384.

[98] Meyer, S. (2006) Einfluss der Wolkenstruktur auf die reflektierte solare Strahlung inhomogener Bewölkung. PhD thesis, University of Kiel, Germany, 120 pp.

[99] Mie, G. (1908) Beiträge zur Optik trüber Medien, speziell kolloidaler Metall-Lösungen. Annalen der Physik, 25, 377-445.

[100] Miles, N.L., Verlinde, J., and Clothiaux, E.E, (2000) Cloud Droplet Size Distributions in Low-Level Stratiform Clouds. Journal of the Atmospheric Sciences, 57, 295-311.

[101] Miller, M.A., Jenson, M.P., and Clothiaux, E.E. (1998) Diurnal cloud and thermodynamic variations in the stratocumulus transition regime: A case study using in situ and remote sensors. Journal of the Atmospheric Sciences, 55, 2294-2310.

[102] Minnis, P., Heck, P.W., Young, D.F., Fairall, C.W., and Snider, J.B. (1992) Stratocumulus cloud properties derived from simultaneous satellite and island-based instrumentation during FIRE. Journal of Applied Meteorology, 31, 317-339.

[103] Moeng, C.-H., Cotton, W.R., Bretherton, C., Chlond, A., Khairoutdinov, M., Krueger, S., Lewellen, W.S., MacVean, M.K., Pasquier, J.R.M., Rand, H.A., Siebesma, A.P., Stevens, B., and Sykes, R.I. (1996) Simulation of a Stratocumulus Topped Planetary Boundary Layer: Intercomparison among Different Numerical Codes. Bulletin of the American Meteorological Society, 77, 261-278.

[104] Moore, D.S., McCabe, G.P., Duckworth, W.M., and Sclove, S.I. (2003) Bootstrap Methods and Permutation Tests. Freeman, New York, 74 pp.

[105] Nakajima, T. and King, M.D. (1990) Determination of the optical thickness and effective particle radius of clouds from reflected solar radiation measurements. Part I: Theory. Journal of the Atmospheric Sciences, 47, 1878-1893.

[106] Naud, C.M., Muller, J.-P., Clothiaux, E.E., Baum, B.A., and Menzel, W.P. (2005) Intercomparison of multiple years of MODIS, MISR and radar cloud-top heights. Annales Geophysicae, 23, 2415-2424.

[107] Neggers, R.A.J,, Jonker, H.J.J., and Siebesma, A.P. (2003) Size statistics of cumulus cloud populations in large-eddy simulations. Journal of the Atmospheric Sciences, 60, 1060-1074.

[108] Nevzorov, A.N., and Shugaev, V.F. (1972) The use of integral parameters for study of cloud microstructure. Transactions of Central Aerological Observatory, 101, 32-47.

[109] Nicholls, S. and Leighton, J. (1986) An observational study of the structure of stratiform cloud sheets: Part I. Structure. Quarterly Journal of the Royal Meteorological Society, 112, 431-460.

[110] Oreopoulos, L. and Davies, R. (1998) Plane parallel albedo bias from satellite observations. Part I: Dependence on resolution and other factors. Journal of Climate, 11, 919-932.

[111] Pardo-Igúzquiza E. and Chica-Olmo, M. (1993) The Fourier Integral Method: An Efficient Spectral Method for Simulation of Random Fields. Mathematical Geology, 25, 177-217.

[112] Pawlowska, H., Brenguier, J.-L., Fouquart, Y., Armbruster, W., Bakan, S., Descloitres J., Fischer, J., Flamant, C., Fouilloux, A., Gayet, J.-F., Gosh, S., Jonas, P., Parol, F., Pelon, J., and Schüller L. (2000) Microphysical and radiative properties of stratocumulus clouds: The EUCREX mission 206 case study. Atmospheric Research, 55, 85-102.

[113] Petty, G.W. (2004) A First Course in Atmospheric Radiation. Sundog Publishing, Madison, 445 pp.

[114] Pincus, R., Szczodrak, M., Gu, J., and Austin, P.H. (1995) Uncertainty in Cloud Optical Depth Estimates made from Satellite Radiance Measurements. Journal of Climate, 8, 1453-1462.

[115] Pincus, R. and Klein, S.A. (2000) Unresolved spatial variability and microphysical process rates in large-scale models. Journal of Geophysical Research, 105, 27059-27065.

[116] Plank, V.E (1969) The size distribution of cumulus clouds in representative Florida populations. Journal of Applied Meteorology, 8, 46-67.

[117] Platnick, S. (2000) Vertical photon transport in cloud remote sensing problems. Journal of Geophysical Research, 105, 22919-22935.

[118] Platnick, S. and Valero, F.P.J. (1995) A Validation of a satellite cloud retrieval during ASTEX. Journal of the Atmospheric Sciences, 52, 2985-3001.

[119] Platt, C.M.R, Young, S.A., Carswell, A.I., Pal, S.R., McCormick, M.P., Winker, D.M., Delgusta M., Stefanutti, L., Eberhard, W.L., Hardesty, M., Flamant, P.H., Valentin, R., Forgan, B., Gimmestad, G.G., Jager, H., Khmelevtsov, S.S., Kolev, I., Kaprieolev, B., Lu, D.R., Sassen, K., Shamanaev, V.S., Uchino, O., Mizuno, Y., Wandinger, U., Weitkamp, C., Ansmann, A., and Woolridge, C. (1994) The Experimental Cloud Lidar Pilot Study (ECLIPS) for cloud radiation research. Bulletin of the American Meteorological Society, 75, 9, 1635-1645.

[120] Press, W.H., Flannery. B.P., Teukolsky, S.A., and Vetterling, W.T. (1992) Numerical recipes. Cambridge University Press, Cambridge, 992 pp.

[121] Rahman, H., Pinty, B. and Verstraete, M.M. (1993) Coupled Surface-Atmosphere Reflectance (CSAR) Model 2. Semiempirical Surface Model usable with NOAA Advanced Very High Resolution Radiometer Data. Journal of Geophysical Research, 98, 20791-20801.

[122] Räisänen, P., Isaac, G.A., Barker, H.W., and Gultepe, I.(2003) Solar radiative transfer for stratiform clouds with horizontal variations in liquid-water path and droplet effective radius. Quarterly Journal of the Royal Meteorological Society, 129, 2135-2149.

[123] Randall, D., Khairoutdinov, M., Arakawa, A., and Grabowski, W. (2003) Breaking the Cloud Parametrization Deadlock. Bulletin of the American Meteorological Society, 84, 1547-1564.

[124] Randall, D.A., Wood, R.A., Bony, S., Colman, R., Fichefet, T., Fyfe, J., Kattsov, V., Pitman, A., Shukla, J., Srinivasan, J., Stouffer, R.J., Sumi, A., and Taylor, K.E. (2007): Climate Models and Their Evaluation. In: Solomon, S., Qin, D., Manning, M., Chen, Z., Marquis, M., Averyt, K.B., Tignor, M., and Miller, H.L. (2007) Climate Change 2007: The Physical Basis. Contribution of Working Group I to the Fourth Assessment Report of the Intergovernmental Panel on Climate Change. Cambridge University Press, Cambridge, 1009 pp.

[125] Richter, F., Barfus, K., Berger, F.H., and Görsdorf, U. (2007) The influence of cloud top variability from radar measurements on 3-D radiative transfer. Atmospheric Chemistry and Physics, 7, 4699-4708.

[126] Ripley, B.D. (1977) Modelling spatial patterns. Journal of the Royal Statistical Society, B 39, 172-212.

[127] Roeckner, E., Brokopf, R., Esch, E., Giorgetta, M., Hagemann, S., Kornblueh, L., Manzini, E., Schlese, U., and Schulzweida, U. (2004) The atmospheric general circulation model ECHAM 5. Part II: Sensitivity of Simulated Climate to Horizontal and Vertical Resolution. MPI-Report 354, Hamburg, 56 pp.

[128] Rogers, R.R. and Yau, M.K. (1989) A Short Course in Cloud Physics. Butterworth-Heinemann, Oxford, 304 pp.

[129] Satheesh, S.K. and Krishna Moorthy, K. (2005) Radiative effects of natural aerosols: A review. Atmospheric Environment, 39, 2089-2110.

[130] Schreiber, T. and Schmitz, A. (1996) Improved surrogate data for nonlinearity tests. Physical Review Letters, 77, 635-638.

[131] Sengupta, M., Clothiaux, E.E., and Ackerman, T.P. (2004) Climatology of Warm Boundary Layer Clouds at the ARM SGP Site and their Comparison to Models. Journal of Climate, 17, 4760-4782.

[132] Shettle, E.P. and Fenn, R.W. (1979) Models for the Aerosols of the Lower Atmosphere and the Effects of Humidity Variations on their Optical Properties. AFGL Technical Report, AFGL-TR-79-0214, 94 pp.

[133] Sloane, C.S. (1984) Optical properties of aerosols of mixed composition. Atmospheric Environment, 18, 871-878.

[134] Solomon, S., Qin, D., Manning, M., Chen, Z., Marquis, M., Averyt, K.B., Tignor, M., and Miller, H.L. (2007) Climate Change 2007: The Physical Basis. Contribution of Working Group I to the Fourth Assessment Report of the Intergovernmental Panel on Climate Change. Cambridge University Press, Cambridge, 1009 pp.

[135] Stephens, G.L., Heidinger, A.K., and Gabriel, P.M. (2005) Photon Paths and Cloud Heterogeneity: An Observational Strategy to Assess Effects of 3D Geometry on Radiative Transfer. in: Marshak, A. and Davis, A.B. 3D Radiative Transfer in Cloudy Atmospheres. Springer, Berlin, 587-616.

[136] Stephens, G.L. and Platt, C.M.R. (1987) Aircraft Observations of the Radiative and Microphysical Properties of Stratocumulus and Cumulus Cloud Fields. Journal of Climate and Applied Meteorology, 26, 1243-1269.

[137] Stephens, G.L., Vane, D.G., Boain, R.J., Mace, G.G., Sassen, K., Wang, Z., Illingworth, A.J., O'Connor, E.J., Rossow, W.B., Durden, S.L., Miller, S.D., Austin, R.T., Benedetti, A., Mitrescu, C., and the Cloudsat Science Team (2002) The Cloudsat Mission and the A-Train. Bulletin of the American Meteorological Society, 83, 1771-1790.

[138] Stevens, B. and Lenschow, D.H. (2001) Observations, Experiments, and Large Eddy Simulation. Bulletin of the American Meteorological Society, 82, 283-294.

[139] Tian, L. and Curry, J.A. (1989) Cloud overlap statistics. Journal of Geophysical Research, 94, 9925-9935.

[140] Tompkins, A.M. (2002) A prognostic parametrization for the subgrid-scale variability of water vapor and its use to diagnose cloud cover. Journal of Atmospheric Sciences, 59, 1917-1942.

[141] Toon, O.B. and Ackerman, T.P. (1981) Algorithms for the calculation of scattering by stratified spheres. Applied Optics, 20, 3657-3660.

[142] Twomey, S.A. (1977) The influence of pollution on the shortwave albedo of clouds. Journal of the Atmospheric Sciences, 34, 1149-1152.

[143] Várnai, T. (2000) Influence of Three-Dimensional Radiative Effects on the Spatial Distribution of Shortwave Cloud Reflection. Journal of the Atmospheric Sciences, 57, 216-229.

[144] Várnai, T. and Davies, R. (1999) Effects of cloud heterogeneities on short-wave radiation: Comparison of cloud-top variability and internal heterogeneity. Journal of Geophysical Research, 104, 2253-2260.

[145] Várnai, T. and Marshak, A. (2001) Statistical Analysis of the Uncertainties in Cloud Optical Depth Retrievals Caused by Three-Dimensional Radiative Effects. Journal of the Atmospheric Sciences, 58, 1540-1548.

[146] Venema, V., Russchenberg, H., Apituley, A., van Lammeren, A., and Ligthart, L. (2000) Cloud boundary height measurements using lidar and radar. Physics and Chemistry of the Earth (B), 25, 129-134.

[147] Venema, V., Meyer, S., García, S.G., Kniffka, A., Simmer, C., Crewell, S., Löhnert, U., Trautmann, T., and Macke, A. (2005) Surrogate cloud fields generated with the Iterative Amplitude Adapted Fourier Transform algorithm. Tellus, 58(1), 104-120.

[148] Wang, Z. and Sassen, L. (2001) Cloud Type and Macrophysical Property Retrieval Using Multiple Remote Sensors. Journal of Applied Meteorology, 40, 1665-1682.

[149] Warner, J. (1955) The water content of cumuliform cloud. Tellus, 7, 449-457.

[150] Wen, G., Marshak, A., and Cahalan, R.F. (2008) Importance of molecular Rayleigh scattering in the enhancement of clear sky reflectance in the vicinity of boundary layer cumulus clouds. Journal of Geophysical Research, 113, D24207, doi:10.129/2008JD010592.

[151] Wilheit, T.T. and Hutchison K.D. (2000) Retrieval of Cloud Base Heights from Passive Microwave and Cloud Top Temperature Data. IEEE Transactions on Geoscience and Remote Sensing, 38, 1253-1259.

[152] Wilks, D.S. (2005) Statistical Methods in Atmospheric Sciences. Academic Press, London, 648 pp.

[153] Wood, R. and Taylor, J.P. (2001) Liquid water path variability in unbroken marine stratocumulus cloud. Quarterly Journal of the Royal Meteorological Society, 127, 2635-2662.

[154] Wylie, D.P., Santek, D., and Starr, D.O. (1998) Cloud-Top Heights from GOES-8 and GOES-9 Stereoscopic Imagery. Journal of Applied Meteorology, 37, 405-413.

[155] Xu, K.-M. (2006) Using the Bootstrap Method for a Statistical Significance Test of Differences between Summary Histograms. Monthly Weather Review, 134, 1442-1453.

[156] Yan, B., Stamnes, K., Wei, L., Chen, B., Stamnes, J.J., and Si-Chee, T. (2002) Pitfalls in atmospheric correction of ocean color imagery: how should aerosol optical properties be computed ? Applied Optics, 41, 412-423.

[157] Yum, S.S. and Hudson, J.G. (2002) Maritime/continental microphysical contrasts in stratus. Tellus, 54, 61-73.

[158] Zinner, T. Mayer, B., and Schröder, M. (2006) Determination of three-dimensional cloud structures from high-resolution radiance data. Journal of Geophysical Research, 111, D08204, doi:10.1029/2005JD006062.

Acknowledgement

It took a long time to pull this ship over the mountain but there has been support from many people I would like to thank. First of all I am especially grateful to Prof. Dr. Christian Bernhofer, who gave me the chance to work in his group and was always interested in the progress of my thesis. Thanks also for reviewing the thesis.
Special thanks go to Prof. Dr. Andreas Macke of the Leibnitz Institute for Tropospheric Research in Leipzig supporting me during the time of the thesis, helped to improve the document and finally was the second reviewer of the thesis.
I also would like to thank PD Dr. habil. Franz Berger for the opportunity to write this thesis and the freedom he has given me for my research.
Dr. Steffen Meyer and Dr. Mario Schewski of the IFM-Geomar always provided me support when working with the Monte Carlo code and answered my questions concerning all aspects of radiative transfer in clouds. I always enjoyed meeting them and having a good time. Thanks for that !
Thanks also to the other guys from the 4D-Clouds project. I am thankful to Dr. Victor Venema for pushing the project all the time and for his idea of having these tutorials accompanying the workshops, where I learned a lot about science. Thanks also because he never became tired explaining me the principles of surrogate clouds and sharing ideas.
Thanks to Dr. Marc Schröder, Dr. Sebastian Schmidt, Sebastian Gimeno García, Dr. Thomas Scholl and Dr. Matthias Jerg for their scientific support and the great time during the 4D-Clouds meetings.
When you get stuck into a problem there are people who give you advice by answering your emails even if they sometimes do not know you. This was one of the most inspiring experiences for me entering the scientific community. Thanks for that to Dr. Tobias Zinner, Prof. Dr. Bernhard Mayer, Dr. Frank Evans, Prof. Dr. Wolfgang Lucht, Prof. Dr. Howard Barker, Dr. Eric Shettle, Dr. Mark Miller, and Prof. Dr. Ruprecht Jänicke.
Improvement of my computer skills was highly supported by the experience of my colleague Dr. Michael Sommer - thanks Michael !
Most of the simulations could not have been carried out without using the super computer of the ZIH Dresden. Thanks for the processors and the computing time and special thanks go to Claudia Schmidt for her assistance checking several non-optimal lines of my code.
I really enjoyed working with Falk Richter and Sebastian Winkler who assisted when computing the microphysical preprocessing routines and also the routines for running the Monte Carlo model. Thanks Falk and Sebastian !
When I went during the period of the thesis to the Richard Assmann Observatory at Lindenberg, I met there two guys always interested in discussions concerning this work. Thanks for that to Dr. Bernd Stiller and Dr. Ulrich Görsdorf.
In the end, and the end may be a very long period, it is good to have trusty lectors. Many thanks to Angela Schwiebus and Kristina Brust showing some endurance doing this job.
Special thanks go to my colleagues from the Chair of Meteorology of the Technische Universität Dresden. I enjoyed the friendly and motivating atmosphere there and life at the institute was always more than a working environment.
The time in the mountains was always good for leaving science behind, recreation, and great experiences. Thanks to all my friends sharing this time.
I thank my family for making it possible to pursue this path and the support over all the years.

The study was carried out within the framework of the 4D-Clouds project funded by the Federal Ministry of Education and Research, Germany.

Erklärung

Hiermit erkläre ich, die vorliegende Arbeit selbständig und ohne die Hilfe anderer Personen angefertigt zu haben. Weiterhin versichere ich, nur frei zugängliche oder lizensierte Software verwendet zu haben, welche mir im Rahmen einer Anstellung als wissenschaftlicher Mitarbeiter an der Professur für Meteorologie des Instituts für Hydrologie und Meteorologie der Technischen Universität Dresden zur Verfügung stand.

Klemens Barfus

Dresden, 01.06.2010